2011

Anisotropic Particles: Preparation and Study

Shengrong Ye
West Virginia University

Anisotropic Particles: Preparation and Study

Shengrong Ye

Dissertation submitted to the
Eberly College of Arts and Sciences
at West Virginia University
in partial fulfillment of the requirements
for the degree of

Doctor of Philosophy
in
Chemistry

R. Lloyd Carroll, Ph.D., Chair
Jeffrey Petersen, Ph.D.
Alan Stolzenberg, Ph.D.
Kenneth Showalter, Ph.D.
David Lederman, Ph.D.

Department of Chemistry

Morgantown, West Virginia
2011

ABSTRACT

Anisotropic Particles: Preparation and Study

Shengrong Ye

Anisotropic particles have received significant attention in self-assembly for the large scale fabrication of hierarchical structures. Janus particles, a specific class of anisotropic particles, have two hemispheres with different materials. Due to the anisotropic nature of the particle shape and interactions, Janus particles have demonstrated interesting properties in interfacial assembly, switchable devices, cargo transport, and optical sensing. The objective of this research is to fabricate novel anisotropic Janus particles and explore their potential unique properties.

One of the driving forces arises from the previous work of bimetallic nanorods and their autonomous motion. The bimetallic nanorod systems undergo chemically powered non-Brownian motion due to the asymmetric distribution of catalytic source for a chemical fuel solution. However, the approach used to prepare the bimetallic nanorods is rather complex. The original design of bimetallic Janus particles is based on a general physical vapor deposition technique – electron beam evaporation. The resulting bimetallic Janus particles are colloidal silica spheres coated with two differing metals on each hemisphere. This approach allows fabricating bimetallic Janus particles with various combinations of metals that are available for electron beam evaporation.

Chemical transformation of bimetallic Janus particles into other species provides an opportunity to expand the scope of anisotropic particles. The metals on the Janus particles are possible to convert to their corresponding metal oxides and metal sulfides through solid-gas heterogeneous reactions, and therefore, the chemical transformation of the parent bimetallic Janus particles produces a wide array of previously unavailable Janus particle types, including metal/metal oxide, metal/metal sulfide, metal oxide/metal oxide, metal sulfide/metal sulfide, and metal oxide/metal sulfide, which allows tuning their optical, electronic, magnetic and catalytic properties. This vast library of anisotropic particulate building blocks provides a powerful arsenal for engineering the assembly of specific targeted structures and systems.

Autonomous motion is distinctive from Brownian motion. Platinum half-coated Janus particles undergo self-propelled motion, which is induced by the catalytic decomposition of hydrogen peroxide. The average speed of the self-propelled Pt-SiO_2 Janus particles increases with increasing the concentration of hydrogen peroxide. Motion direction analyses show that the

probability for the Janus particles continuing to travel in nearly same direction goes higher in higher concentrations of hydrogen peroxide. Microscopic observation of the particle motion demonstrates that these Janus particles move, on average, with the platinum-coated region oriented opposite to the direction of motion. The trajectories of the autonomous motion exhibit a directed motion at short time scale but with an overall random behavior at long time scales. Huge benefit can be garnered by taking advantage of the self-propulsion component in the system. The control of the motion of the magnetic Janus particles in solutions of hydrogen peroxide is demonstrated using the external magnetic field. The magnetic Janus particles orient themselves with the equatorial plane parallel to the applied field and the motion direction is perpendicular to the field. The directed motion has a more distinct preferred direction compared to the case in the absence of magnetic field, and the applied field is verified to control the orientation, not influence the speed of the particle motion.

Anisotropic particles are unique building blocks to assemble complex structures. The surface functionalized Janus particles with alkanethiols are adsorbed at the interfaces of liquid-air and liquid-liquid, forming monolayers with metal hemispheres pointing to the same direction. By changing the liquid oil phase, the orientation of the Janus particles can be manipulated, which provides an opportunity to selectively modify the surface in either phase. The preferential orientation in the same direction at interfaces allows for direct transfer of the Janus particles while the desired faces remain in either a “face-down” or “face-up” configuration. An external intervention, magnetic field, is also sought to direct the assembly of the magnetic Janus particles. In the presence of uniform magnetic field, the magnetic Janus particles form staggered chain structures with the chain direction parallel to the direction of the applied field. These chain structures are destroyed due to the capillary force during solvent evaporation. However, these soft structures are successfully locked in place after the solution dries by the addition of ammonium carbonate to the solution, which suggests a promising way to achieve 2D or 3D super structures for the fabrication of photonic crystals and photonic devices.

Acknowledgements

All the work described in this dissertation would not have been possible without the help and support of many people. First and foremost, I would like to express my deepest thanks to my PhD advisor, Professor R. Lloyd Carroll, for his five-year guidance, inspiration, advice, encouragement, and support in research. Personally, he is also a great friend for me to learn culture and language in the US. Secondly, I appreciate the help and the friendship as well from the current and previous members in his research group. They are Aaron Routzahn, Kyoo Jo, Zack Jones, Sri Yedlapalli, Yuan Li, Mikala Shremshock, Ichhuk Karki, and Victor Aldelsayed. Thanks as well to Professor Kenneth Showlater and his student Kua Ke for the collaboration work on motion analysis. I am deeply grateful to the professors in my Graduate Research Committee, Profs. R. Lloyd Carroll, Jeffrey Petersen, Alan Stolzenberg, Kenneth Showalter, and David Lederman, for their services, and, especially, those detailed comments during the research proposal defense and dissertation defense. I thank Dr. Felio Perez and Kineshma Munbodh for teaching me to use the VSM and XRD in Dr. Lederman's group. The WVU shared facility and her staff, Dr. Kolin Brown, Dr. Andew Woodworth, Mr. Harley Hart and Dr. Weiqing Ding, has been the source of help on training and maintenance. Same thanks go to Dr. Keith Morris and WVU Forensic Chemistry for the use of their instruments. Finally, I greatly appreciate my wife, Jie Xiao, two daughters, Shawn and Lauren, and my parents, Jiegen Ye and Ruzhen Wang, for their love and sacrifice.

Table of Contents

List of Figures

Chapter 1

Chapter 2

Chapter 1

Anisotropic Particles: Preparation and Applications

1.1 Anisotropic Particles

Understanding the relationship between structure and property has been the primary interest in the physical sciences over the past decades. Self-assembly – the spontaneous formation of matter into ordered structures from 'disordered' components – is a widely accepted approach to create complex structures at virtually any length scale spanning from atomic to astronomic.[1-3] The assembled structures are becoming increasingly important for applications in photonics,[4,5] electronics,[6] optical and biological sensing.[7,8] In any self-assembling system, the properties (i.e. composition, shape, interaction) of the individual components (building blocks) plays a key role in determining the resulting structures.[1,9] Isotropic colloidal particles, one of the most fundamental building blocks, have been the focus for particle assembly in the range of fields: chemistry, physics, materials science, nanoscience, and manufacturing. These materials form simple symmetric structures (e.g. face-center cubic, hexagonal close-packed, and body-center cubic lattices) in the solid state, and possibly, other extended colloidal structures using templated approaches or external forces.[10,11]

Recently, rapid progress has been made in the design and synthesis of novel building blocks with anisotropic shape and functionality, facilitating the engineering of the particle assembly into complex superstructures.[12,13] Glotzer and Solomon proposed a classification of anisotropic particles in their review article.[14] Figure 1-1 lists examples of recently synthesized anisotropic particle building blocks, possessing diverse anisotropy in shape, composition, functionality. In contrast to the isotropic spherical colloids, starting self-assembly with complex structures suggests a promising approach to create complex structures in a potentially controllable and predictable way.[15] According to the simulations using "patchy particles" made of synthetic organic or biological molecules, Glotzer predicted that combinations of forces, particle shapes, and building-block topology would provide means for assembling the particles into wires, sheets, tubes, and other structures.[1,16] Figure 1-2 depicts a fraction of vast array of structures possible through relatively simple precursors. For instance, the twisted wire (left) is assembled from tethered triangular nanoparticles; tetrahedron, icosahedron, and ring (middle) are self-assembled from spherical patchy particles; micelle (right) is assembled from tethered

nanospheres. These novel anisotropic building blocks provide potentially much greater control over a material's structure and properties, enabling design and programming rather than selection of materials for specific applications.[1]

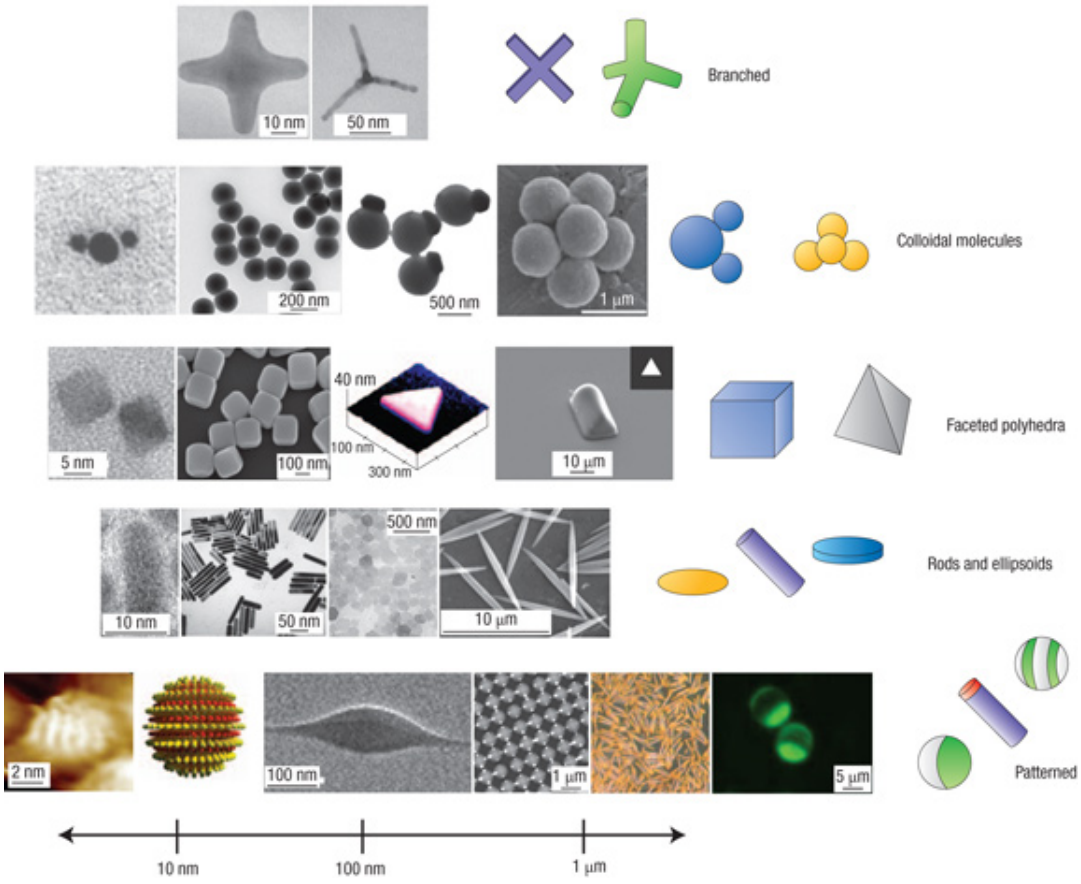

Figure 1-1. Representative examples of synthesized anisotropic particle building blocks.[14] From left to right, row 1: branched particles include gold and CdTe tetrapods; row 2: DNA-linked gold nanocrystals, silica dumb-bells, asymmetric dimers and fused clusters; row 3: PbSe and Ag cubes, Au and polymer triangular prisms; row 4: rods and ellipsoids of composition CdSe, Au, gibbsite and polymer latex; row 5: patterned particles include striped spheres, biphasic rods, patchy spheres with 'valence', Au–Pt nanorods and Janus spheres.

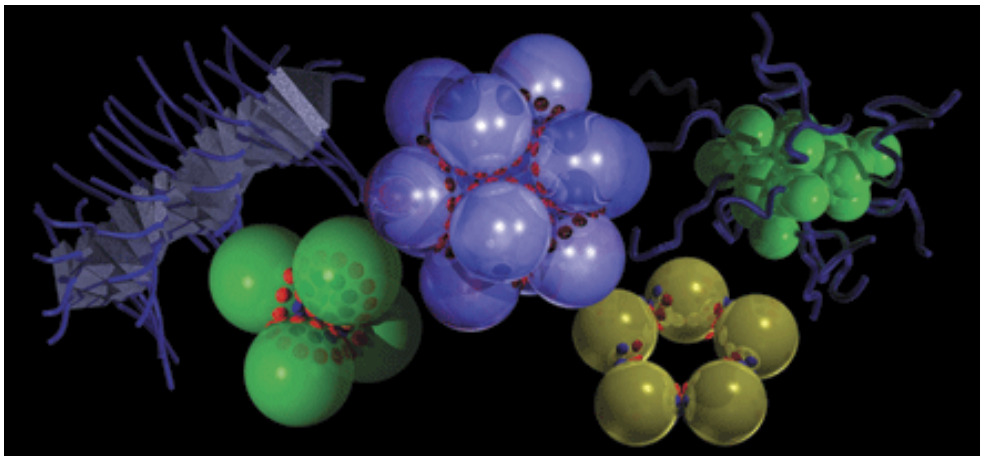

Figure 1-2. Predicted self-assembled structures for model building blocks.[1]

Self-assembly occurs when the building blocks preferentially interact with each other through a balance of interactions.[2] In many cases, however, these anisotropic building blocks do not self-assemble into desired structures. It is crucial to develop methods allowing unprecedented control over the forces exerted on individual particles. Such techniques for directed particle assembly are under development through application of external stresses such as electric field,[17,18] magnetic field.[19] Velev and coworkers observed dipoles induced through electric field directs the formation of chains, crystals and nanoparticle wires.[20] Development of particles in response to applied fields offers potential approaches for formation of pre-programmed complex structures on demand.

The design and synthesis of novel anisotropic particles is critical in engineering bottom-up fabrication of self-assembling multifunctional and smart materials. Multifunctionality is a universal trait of biological materials and systems in nature. These biological systems routinely contain sensing, healing, actuation, and other functional capabilities built into the primary structures of an organism. The human skin, for instance, consists of a stratified, cellular epidermis and an underlying dermis of connective tissue, which performs integrated physiological functions of protection, sensation, thermoregulation, control of water evaporation, communication, storage, synthesis, excretion, absorption, and water resistance.[21,22] Scientists seek to synthesize unique multifunctional material systems using bottom-up approach mimicking those

natural chemical and biological processes. Artificial multifunctional materials and structures are defined as a structure which has the ability to simultaneously or sequentially perform a task or a series of tasks (e.g. sensing, control, actuation, and motion) through judicious combinations of structural integrity.[23] The integration of multifunctionality may provide advantages in reducing size, weight, cost, power consumption, and complexity while improving performance, efficiency, safety, versatility and lifetime. Recently, the concept of biologically inspired nanotechnology, or bionanotechnology, has been developed to become a new frontier, leading to new generations of smart materials and intelligent systems.[24]

1.2 Janus Particles

"Janus" particles are an anisotropic building block possessing potentially complex shapes and competing interactions that expand the range of self-assembly beyond those exhibited by traditional isotropic building blocks.[12,13,25-28] The term Janus, named after the double-faced Roman god (Figure 1-3A) who has two faces looking into opposite directions, is used here to describe particles that have two hemispheres with different materials (Figure 1-3B). In 1991, P. G. de Gennes[29] first raised the concept of "Janus" particles in his Nobel lecture and he predicted that the amphiphilic Janus particles would act similarly as the molecular surfactant and block copolymer. Recently, many techniques have been developed for the fabrication of anisotropic (Janus) particles.[12,13,25-27,30,31] Parwar and Kretzschmar summarized several major techniques to fabricate anisotropic Janus particles, including templating, capillary fluid flow, nanosphere lithography, glancing angle deposition, particle lithography and colloidal clusters.[27] These methods may be broadly classified into three categories: 1) toposelective surface functionalization, including interfacial self-assembly,[32-45] physical/chemical vapor deposition,[46-56] masking,[57-65] and micro-contact printing (μCP),[66-70] 2) micro-fluidic condensation,[31,71-76] 3) phase separation.[77-84]

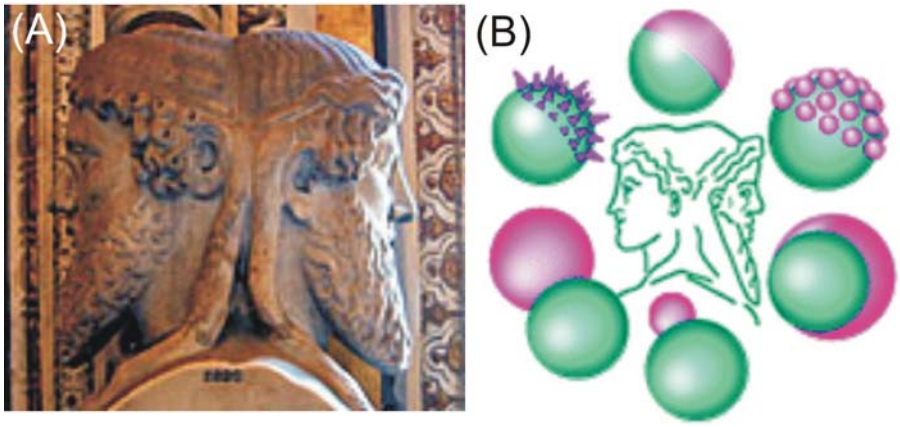

Figure 1-3. (A) Sculpture of the two-faced god Janus in Rome's Vatican Museums.[85] (B) Schematic representations of various types of Janus particles.[25]

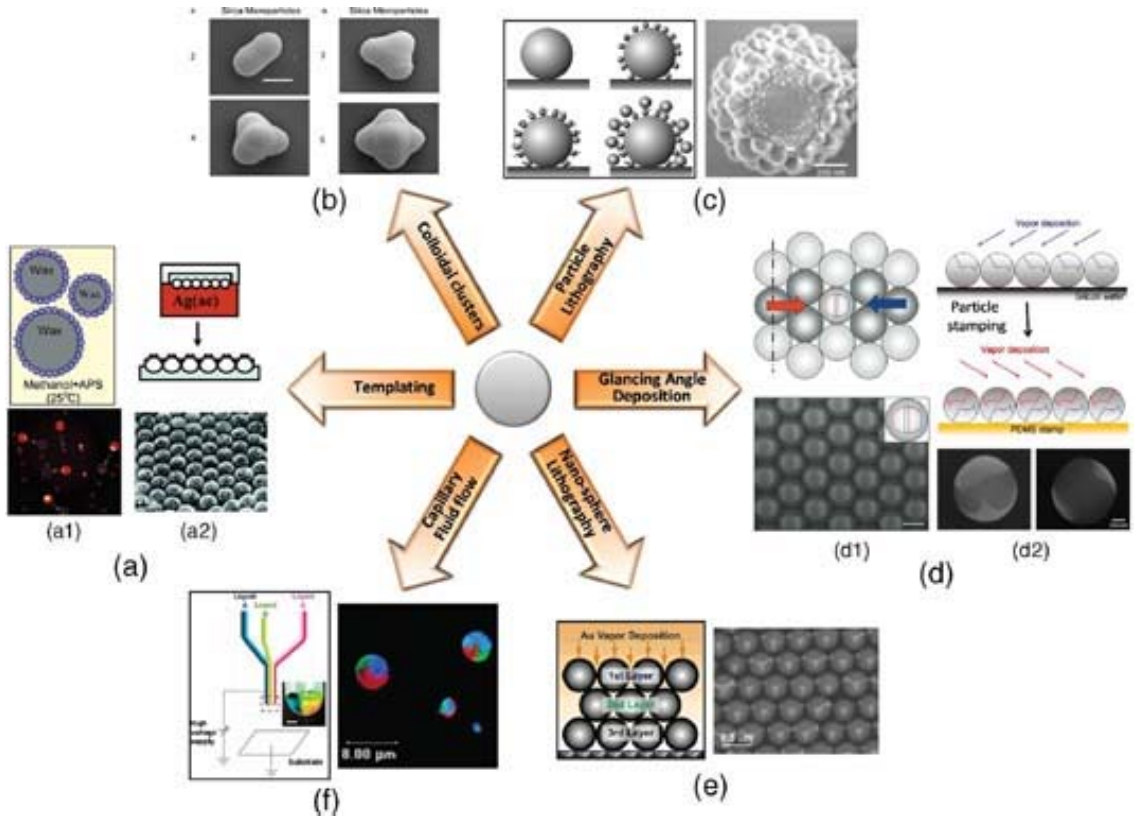

Figure 1-4. Techniques for fabrication of anisotropic (Janus) particles.[27]

Janus particles possess integrated multi-functionality of disparate components into a single unit or structure potentially with vastly different optical, electrical, magnetic and catalytic properties. Due to their unique structures and properties, they have become an

active area of research, especially for applications as anisotropic building blocks for advanced hierarchical structures,[14,17-19,26,27,86-90] switchable display devices,[71] particulate surfactants,[40,45,91,92] self-motile particles for targeted cargo transportation,[93,94] optical and biological sensing.[58,72,95,96] For example, Janus particles with one metallic hemisphere and one dielectric hemisphere can be assembled into staggered chain structures in the presence of AC electric field (Figure 1-5A).[17] Nisisako and coworkers demonstrated that the bicolor Janus particles with a dipolar character can be electrically actuated for application in a particle-based electronic paper display (Figure 1-5B).[71] Through selective chemical modification, amphiphilic Janus particles (hydrophobic on one side and hydrophilic on the other) can be produced and adsorbed strongly to the water/oil interface (Figure 1-5C).[40] The Pt-Au bimetallic nanorods undergo autonomous motion in a solution of hydrogen peroxide with the ability of transport of a prototypical cargo – polystyrene microspheres (Figure 1-5D).[93] McConnell and coworkers also demonstrated that the optical property of the gold nanoparticles decorated Janus particles can be tuned by changing the surface energy between the silica and gold particles (Figure 1-5E).[58]

Chemically powered motion exhibited by certain types of Janus particles attracts significant attention into this field. Self-propelled motion and control on the nanoscale in solution and at interfaces is one of the grand challenges in nanotechnology.[97] Mechanistic understanding would form the foundation for applications in cargo transport and drug delivery. Whitesides and coworkers initially demonstrated the catalytic decomposition of hydrogen peroxide can force millimeter-scale objects to glide across the surface of a liquid without external intervention.[98] Following this preliminary example of a chemically powered synthetic motor, the Sen and Mallouk groups at the Penn State University[99] and the Ozin group at the University of Toronto[100] independently developed a variety of self-propelled systems such as Au/Pt and Au/Ni bimetallic nanorods in solutions of hydrogen peroxide (Figure 1-6). These projectiles based on the catalytic decomposition of H_2O_2, were observed to undergo dominantly translational motion and circular motion. A remotely controlled movement was demonstrated in a similar motor system (Pt/Ni/Au/Ni/Au) with the incorporation of nickel into the Au/Pt nanorods.[101] The application of external magnetic field resulted in higher directionality and substantially lower transverse rotation. Sen and coworkers reported the feasibility of using synthetic

nanomotor systems for microscale transport of cargo to target in solution in the presence of magnetic field,[93] followed by Wang and coworkers, who further demonstrated the cargo transport within a microfluidic network.[94] These studies lead to the practical applications of lab-on-chip devices performing a series of tasks simultaneously or sequentially with significant prospects in drug delivery.

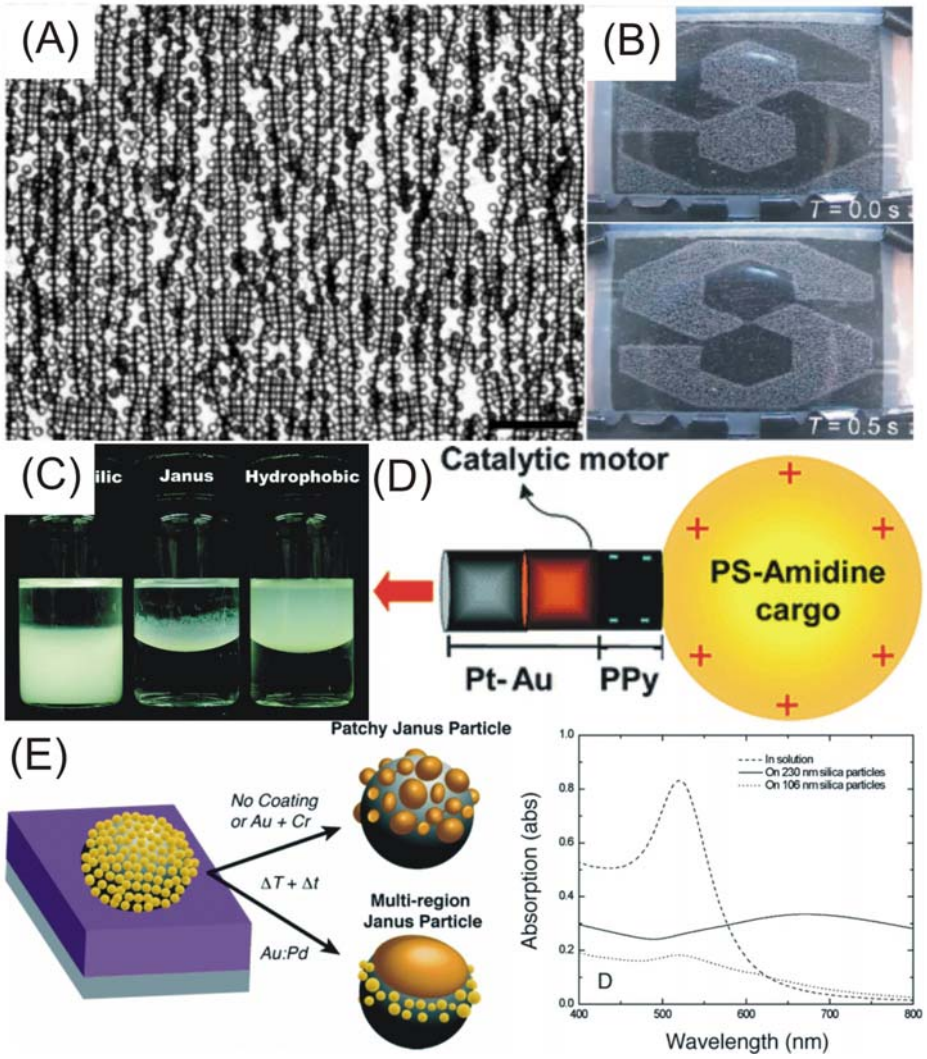

Figure 1-5. (A) chain structures formed by the Janus particles in the presence of electric field.[17] (B) switchable display devices using electrical actuation.[71] (C) Amphiphilic Janus particles adsorbed as particulate surfactants at water/oil interface.[40] (D) Transport of a prototypical cargo by an Au/Pt catalytic motor.[93] (E) Optically active Janus particles.[58]

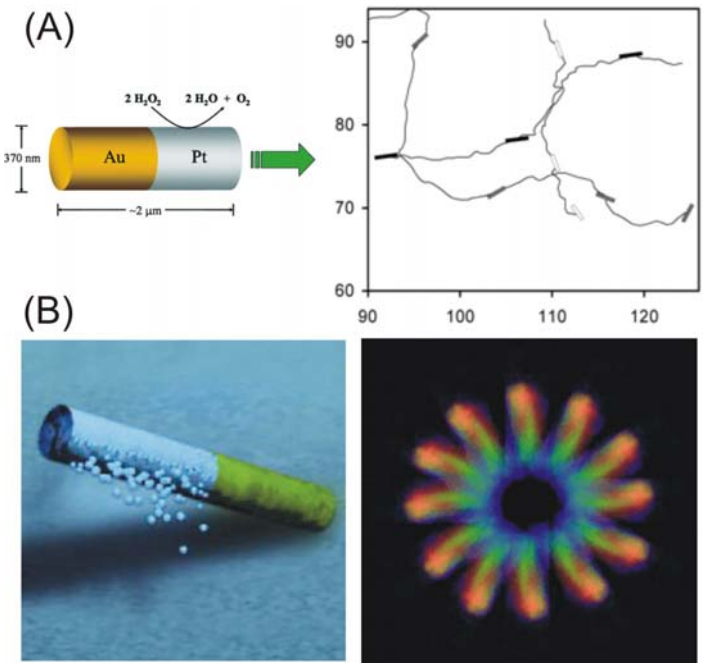

Figure 1-6. (A) Schematic illustration of the autonomous movement of one Au/Pt bimetallic rod by decomposition at the platinum end and the trajectory plots.[99] (B) Circular motion of Au/Ni nanorod tethered to silicon wafer in H_2O_2 solution when oxygen is generated at the nickel end.[100]

In nature, many useful structures arise via self-assembly such as the formation of lipid bilayers and the folding of polypeptide chains into proteins.[2] The assembly of both isotropic and anisotropic particle building blocks has already been implemented. Starting self-assembly from anisotropic particles offers increased possibilities. Glotzer and Zhang studied the self-assembly of particles with discrete and attractive "patches" into chains, sheets, rings, icosahedra, square pyramids, tetrahedral, and twisted and staircase structures by performing molecular simulation.[102] Granick and coworkers both theoretically and experimentally demonstrated that the Janus bipolar particles and Janus amphiphilic particles assembled into clusters and strings due to the nature of anisotropy in attractive and repulsive interactions. These works provided insight into the formation mechanism of the superstructures observed in experiments. In addition to utilize the internal force between the Janus particles, the external intervention has also been applied to direct the assembly. The external electric field drove the metal half-coated Janus particles to form staggered chain structures, where the metal half shells of neighboring

particles align into lanes along the direction of the electric field, which were different from those structures obtained from self-assembly of plain particles.[17] Janus character of the particles with a magnetic hemisphere on one side combined with the external magnetic field guided the particles into new types of chain structures.[19] Other external forces such as light are possible to direct the assembly into unique configurations.[103] The directed assembly of anisotropic particles has great potential for applications in photonics, electronics, and optics, but is still at the very early stage. The objective of our research is to design and synthesize new anisotropic building blocks and explore their possible unique properties.

1.3 Dissertation Design and Layout

The work presented herein focuses on the synthesis and characterization of anisotropic particles. The design and synthesis of anisotropic particles aims to create novel anisotropic building blocks, providing the basis for studying the behavior in motion and assembly. The main idea demonstrated in previous work is the Au-Pt [99] and Au-Ni bimetallic nanorod systems[100] undergo autonomous motion in a fuel solution. In both cases, anisotropy played an key role as the catalytic decomposition of hydrogen peroxide occurred on Pt and Ni segments (Pt and Ni are the catalysts for decomposition of hydrogen peroxide), which induced translational motion and circular movement. These systems can be considered as the smallest synthetic engines converting chemical energy into mechanical movement. However, the method to fabricate bimetallic nanorods is rather complex. A similar bimetallic system was believed to be possible using a novel approach based on the evaporation of the relevant metals. This method led to the design of bimetallic Janus particles (BJPs) composed of (silica) microspheres with two different half-shell coatings of metals on the opposite hemispheres and these two metals should be in complete contact with each other.[46] Our objective was to compare the difference in translational and rotational diffusion from the associated shape change of the particles.

Due to intrinsic “shadowing” in e-beam evaporation and the curved spherical surface, however, this approach produced BJPs with an uncoated silica belt around the equatorial region of the particles. The prepared Au-Pt BJPs displayed unique behavior as

the platinum was the forward facing metal during motion.[104] Based on the Pt-SiO_2 Janus particle system, we analyzed the motion behavior in detail[105] and controlled motion in the presence of magnetic field.[106] Meanwhile, on the side of material preparation, two approaches were discovered to chemically transform the prepared bimetallic Janus particles, which led to a new realm of anisotropic building blocks in the formation of colloidal Janus particles consisting of metals, metal oxides, metal sulfides.[107] These Janus particles exhibited interesting surface anisotropy property during further study of assembly. The self-assembly of Janus particles at interface and specific assembly in the presence of external intervention such as magnetic field were investigated. We believe that there is a huge benefit in understanding the basic principles of surfactants and colloidal packing by study of Janus particles and their fundamental behaviors.

The scope of our research contained in the dissertation is laid out in Chart 1. This work is centered on the preparation of anisotropic particles, diverging into four different directions – preparation of Janus particles and chemical transformation, motion analysis, JPs at interface, and directed assembly of JPs in the applied field – towards preparation of new anisotropic building blocks, and future application in cargo transport and drug delivery, particulate surfactants, and assembly of particular targeted structures.

According to Chart 2, this research work heavily focuses on the fundamental aspect, including preparation of bimetallic Janus particles and other types of Janus particles (Stage I), and study of the interfacial and directed assembly of the Janus particles and motion dynamics of the Janus particles (Stage II). The possible practical applications (Stage III) in optical biosensors and electronic devices, particulate surfactants, and cargo transport and drug delivery will be pursued in the future. Thus, the research described in the dissertation includes design and preparation of novel anisotropic particles (Janus particles, Chapter 2), chemical transformation of bimetallic Janus particles and ultrathin metal films (Chapter 3), and motion analysis of Janus particles in the presence and absence of magnetic field (Chapter 4), the behavior of Janus particles at interfaces, and directed assembly of magnetic Janus particles (Chapter 5). The Chapters 2 and 3 focus on the preparation of Janus particles and the Chapters 4 and 5 study the motion behavior in a fuel system and directed assembly of the prepared Janus particles,

respectively. The first two sections of each chapter contain specific background introduction and experimental sections.

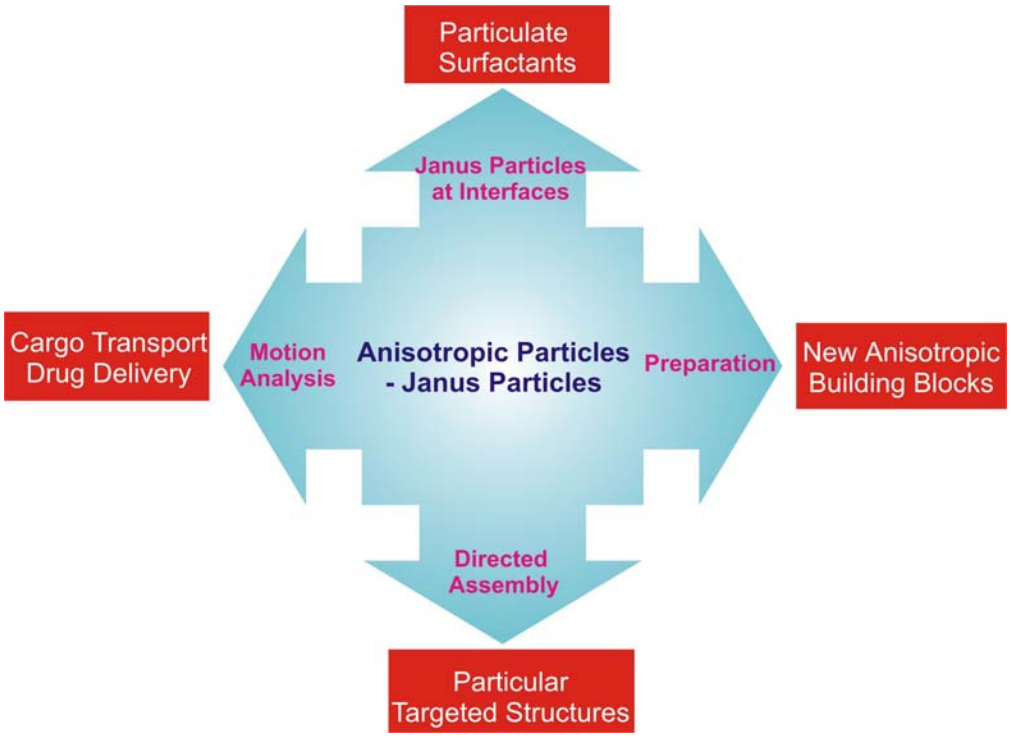

Chart 1

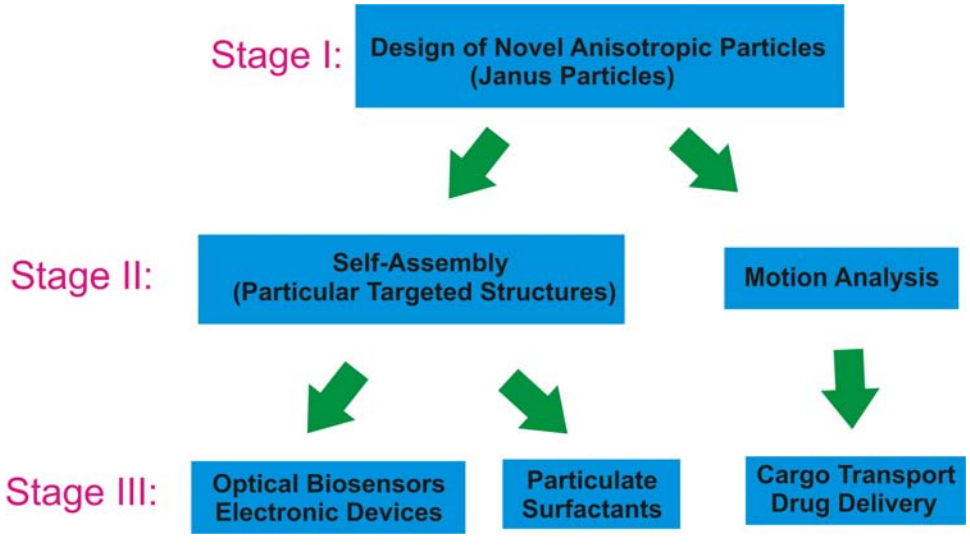

Chart 2

In the third section of Chapter 2, a new approach to prepare the bimetallic Janus particles (BJPs) is described, including (1) the self-assembly of a monolayer of silica particles, (2) the metal deposition via electron beam evaporation, (3) the inversion of the metal half-coated particles onto another substrate, and (4) the second metal deposition. The resulting BJPs are composed of silica colloidal spheres coated with differing metals on opposite hemispheres. SEM imaging, EDS mapping, and XPS analysis clearly indicate that beads are capped with two different metals, typically leaving an equatorial belt around the particle composed of uncoated silica. The inversion of the particles is realized by using the double-sided adhesive copper tape due to its capability of picking and releasing the particles. Silica particles of sizes in diameter of 800 nm and up have been successfully inverted and evaporated with two different metals.

The silica belt leaves a gap between those two metals on the bimetallic Janus particles. In another word, the silica particles cannot be fully coated with metals using e-beam evaporation. During evaporation, the close-packed particles are found to have a tendency to be "welded" when the thickness of the coating increases, forming particle clusters ("rafts"), which are hard to break into individual particles. These observations lead to a further study of the structure of the metal coating on the spherical surface. In the fourth section of Chapter 2, we discuss the relationship between the curved surface and the metal vapor flux. Due to the curvature of the spherical surface, the relative angle of the sphere surface with respect to the metal vapor flux increases from the pole position to the equator. The pole position, where the angle $\theta = 0°$, is supposed to receive the maximal thickness of the coating whereas the equator, where $\theta = 90°$, is supposed to receive the minimal thickness, resulting in a non-uniform coating on the sphere surface. This observation supports the presence of the silica belt around the equatorial regions. By determining the thickness on the flat substrates using SEM and AFM, instead, an empirical numerical model is developed to predict, and thus, control the growth of the metal coating on the particle and the resulting nanostructures on the substrate.

The bimetallic Janus particles can be prepared with combination of various metals that are available for physical vapor deposition. Anisotropic particles with new structures are desired for new properties since the properties of BJPs are most likely limited to

metals. In the third section of Chapter 3, two approaches, post-fabrication transformation and intermediate transformation, are demonstrated to transform BJPs into other types of Janus particles with various combinations of metals, metal oxides and metal sulfides through solid-gas heterogeneous reactions. The heterogeneous reactions include native oxidation under atmospheric conditions, induced oxidation in an air plasma, and sulfidation reaction with hydrogen sulfide. These reactions are chosen for cleanness and no need for post-reaction purification and separation. Characterization of the resulting Janus particles by SEM, XPS, EDS, and XRD clearly demonstrates that the chemical transformation of the parent metal/metal BJPs produces a wide array of previously unavailable JP types, including metal/metal oxide, metal/metal sulfide, metal oxide/metal oxide, metal sulfide/metal sulfide, and metal oxide/metal sulfide. This vast library of anisotropic particulate building blocks provides a powerful arsenal for engineering the assembly of specific targeted structures and systems.

The morphological change, if any, in the metal coating before and after chemical transformation can be clearly visualized via SEM. The change in crystal structure can also be determined by using XRD. Due to curved structure of the particle surface, however, XPS is only able to provide the information on the surface, and thus, it is hard to characterize the compositional change in the entire film. To further understand the chemical transformation of the metal coatings on BJPs, metal coatings with same thickness on flat silicon substrates are used as a model system for comparison with the curved surface. In the fourth section of Chapter 3, the oxidation and sulfidation of various metal thin films, including aluminum, titanium, cobalt, nickel, and silver, under the same reaction condition for chemical transformation of BJPs is investigated. SEM clearly demonstrates the morphological change and the XPS depth profiling and X-ray reflectivity reveal the stratified structures of the metal thin films upon oxidation and sulfidation.

The previous work of autonomous motion (non-Brownian motion) of bimetallic nanorods in a fuel solution encouraged us to design and prepare spherical Janus particles. In those cases, the bimetallic nanorods move with the catalytic metals such as platinum and nickel in the forward direction. The proposed mechanism for motion involves a

process of electron transfer between the inert and active metals. However, the prepared bimetallic Janus particles do not behave similarly due to the gap between the metal coatings. Furthermore, only one catalytic metal such as platinum is found to be sufficient to propel the particle move in the solution of hydrogen peroxide. In the third section of Chapter 4, we demonstrate that silica microspheres that are half-coated with platinum metal undergo autonomous motion in solutions of hydrogen peroxide, with the average speed increasing with increasing H_2O_2 concentration. On average, the particles move with the platinum-coated region oriented opposite to the direction of motion. Velocity autocorrelation and motion direction analyses show that the direction of motion is highly correlated with the particle orientation. The observation time scale may correspond to a regime of Brownian-like motion, where the observation occurs on a longer time scale than the rotational diffusion time, or to a regime of directed propulsion, where the observation occurs on a shorter time scale than the rotational diffusion time.

Autonomous motion is clearly different from the Brownian motion. Due to the ubiquitous Brownian effect, the direction of Janus particles is always interrupted, leading to an ultimately randomized motion over a long time scale. In the case of autonomous motion, however, the particles move in the same direction for relatively long periods of time. By taking advantage of the self-propulsion force present in the system, and therefore, steering the Janus particle from a place to another, huge benefit can be obtained for practical uses in targeted delivery. In the fourth section of Chapter 4, a new self-motile magnetic Janus particle system undergoing autonomous motion with controlled pathway in the presence of external magnetic field is described. The magnetic Janus particles are composed of silica colloidal spheres half-coated with nickel and platinum. Platinum is responsible for the self-propulsion in solutions of hydrogen peroxide, and nickel is incorporated for remote orientation control using external magnetic field. The magnetic Janus particles respond immediately to the magnetic field, orienting themselves with the equatorial plane parallel to the direction of the applied field, and rotate following with the rotating field. Our analyses show that a more preferred directionality is observed compared to the autonomous motion without the influence of applied field.

Janus particles are featured as physically and/or chemically anisotropic structures. Due to the dual functionality, the Janus particles considered as a group of unique building blocks are promising for assembly to create complex structures. In the third section of Chapter 5, the behavior of the functionalized Janus particles at interfaces is demonstrated. The Au/Ni-SiO_2 Janus particles are chemisorbed with organosulfur species (alkanethiol) on the metal coatings, resulting in amphiphilic Janus particles. These new JPs are confined at the interfaces of water/air and water/oil with the hydrocarbon-modified metal coatings pointing to the atmosphere or the oil phase. The JPs' preferential orientation in the same direction at interface allows for direct transfer or selective modification of particles. Direct transfer of the "face-down" configuration onto a supporting substrate provides an alternative approach to prepare bimetallic Janus particles.

Self-assembling uniform colloidal particles typically results in ordered *fcc* or *hcp* structures. A similar structure composed of anisotropic particles is highly desired in the area of photonic crystals and devices. In most cases, however, self-assembly through anisotropic particles, for instance, the metal half-coated Janus particles, leads to a distribution of particles with random orientation. External intervention is sought to direct the assembly of Janus particles, producing 2D or 3D desired superstructures. In the fourth section of Chapter 5, the specific assembly of the magnetic Janus particles (Ni-SiO_2 JPs) is demonstrated in the presence of external uniform magnetic field. Staggered chain structures are formed with the orientation aligned along the direction of the applied field (parallel to the substrate surface). By changing the direction of applied field to perpendicular to the substrate surface, the magnetic JPs disassemble from the chains and, in most cases, form dimeric clusters. However, the 2D chain structures cannot be maintained during evaporation of the solvent (water) due to the capillary force. A method is demonstrated to retain the chain structures by replacement of water with a saturated solution of $(NH_4)_2CO_3$. The $(NH_4)_2CO_3$ re-crystallizes during evaporation and the recrystallization locks the chain structures in place. At temperature of 60 °C, the $(NH_4)_2CO_3$ can be removed completely due to decomposition into gas molecules, leaving the particle chains aligned on the substrate.

Chapter 6 summaries the research work described in this dissertation. In addition, an outlook for the related future work is discussed.

References

(1) Glotzer, S. C. *Science* **2004**, *306*, 419-420.

(2) Whitesides, G. M.; Boncheva, M. *Proceedings of the National Academy of Sciences* **2002**, *99*, 4769-4774.

(3) Whitesides, G. M.; Mathias, J. P.; Seto, C. T. *Science* **1991**, *254*, 1312-1319.

(4) Xia, Y.; Gates, B.; Li, Z. Y. *Advanced Materials* **2001**, *13*, 409-413.

(5) Vlasov, Y. A.; Bo, X.-Z.; Sturm, J. C.; Norris, D. J. *Nature* **2001**, *414*, 289-293.

(6) Smith, W. F. *Nat Nano* **2007**, *2*, 77-78.

(7) Anker, J. N.; Hall, W. P.; Lyandres, O.; Shah, N. C.; Zhao, J.; Van Duyne, R. P. *Nat Mater* **2008**, *7*, 442-453.

(8) Haynes, C. L.; Van Duyne, R. P. *The Journal of Physical Chemistry B* **2001**, *105*, 5599-5611.

(9) Fejer, S. N.; Chakrabarti, D.; Wales, D. J. *Soft Matter* **2011**, *7*, 3553-3564.

(10) Yethiraj, A.; van Blaaderen, A. *Nature* **2003**, *421*, 513-517.

(11) Leunissen, M. E.; Christova, C. G.; Hynninen, A.-P.; Royall, C. P.; Campbell, A. I.; Imhof, A.; Dijkstra, M.; van Roij, R.; van Blaaderen, A. *Nature* **2005**, *437*, 235-240.

(12) Du, J.; O'Reilly, R. K. *Chem. Soc. Rev.* **2011**, *40*, 2402-2416.

(13) Lee, K. J.; Yoon, J.; Lahann, J. *Curr. Opin. Colloid Interface Sci.* **2011**, *16*, 195-202.

(14) Glotzer, S. C.; Solomon, M. J. *Nat. Mater.* **2007**, *6*, 557-562.

(15) van Blaaderen, A. *Nature* **2006**, *439*, 545-546.

(16) Glotzer, S. C.; Solomon, M. J.; Kotov, N. A. *AIChE Journal* **2004**, *50*, 2978-2985.

(17) Gangwal, S.; Cayre, O. J.; Velev, O. D. *Langmuir* **2008**, *24*, 13312-13320.

(18) Gangwal, S.; Pawar, A.; Kretzschmar, I.; Velev, O. D. *Soft Matter* **2010**, *6*, 1413-1418.

(19) Smoukov, S. K.; Gangwal, S.; Marquez, M.; Velev, O. D. *Soft Matter* **2009**, *5*, 1285-1292.

(20) Velev, O. D.; Bhatt, K. H. *Soft Matter* **2006**, *2*, 738-750.

(21) Montagna, W.; Parakkal, P. F. *The structure and function of skin*; 3rd ed.; Academic Press: New York, 1974.

(22) Bensouilah, J.; Buck, P. *Aromadermatology: aromatherapy in the treatment and care of common skin conditions*; Radcliffe Publishing Ltd: London, 2006.

(23) *Nanoengineering of Structural, Functional and Smart Materials*; Schulz, M. J.; Kelkar, A. D.; Sundaresan, M. J., Eds.; CRC Press: New York, 2005.

(24) *Biomimetics: Biologically Inspired Technologies*; Bar-Cohen, Y., Ed.; CRC Press, 2006.

(25) Perro, A.; Reculusa, S.; Ravaine, S.; Bourgeat-Lami, E.; Duguet, E. *J. Mater. Chem.* **2005**, *15*, 3745-3760.

(26) Jiang, S.; Chen, Q.; Tripathy, M.; Luijten, E.; Schweizer, K. S.; Granick, S. *Adv. Mater.* **2010**, *22*, 1060-1071.

(27) Pawar, A. B.; Kretzschmar, I. *Macromol. Rapid Comm.* **2010**, *31*, 150-168.

(28) Walther, A.; Muller, A. H. E. *Soft Matter* **2008**, *4*, 663-668.

(29) de Gennes, P. G. *Rev. Mod. Phys.* **1992**, *64*, 645.

(30) Wurm, F.; Kilbinger, A. F. M. *Angew. Chem. Int. Ed.* **2009**, *48*, 8412-8421.

(31) Dendukuri, D.; Doyle, P. S. *Adv. Mater.* **2009**, *21*, 4071-4086.

(32) Paunov, V. N. *Langmuir* **2003**, *19*, 7970-7976.

(33) Paunov, V. N.; Cayre, O. J. *Adv. Mater.* **2004**, *16*, 788-791.

(34) Zhang, J.; Jin, J.; Zhao, H. *Langmuir* **2009**, *25*, 6431-6437.

(35) Zhang, J.; Wang, X.; Wu, D.; Liu, L.; Zhao, H. *Chem. Mater.* **2009**, *21*, 4012-4018.

(36) Biji, P.; Sarangi, N. K.; Patnaik, A. *Langmuir* **2010**, *26*, 14047-14057.

(37) Nie, L.; Liu, S.; Shen, W.; Chen, D.; Jiang, M. *Angew. Chem. Int. Ed.* **2007**, *46*, 6321-6324.

(38) Perro, A.; Meunier, F.; Schmitt, V.; Ravaine, S. *Colloids Surfaces A* **2009**, *332*, 57-62.

(39) Hong, L.; Jiang, S.; Granick, S. *Langmuir* **2006**, *22*, 9495-9499.

(40) Jiang, S.; Schultz, M. J.; Chen, Q.; Moore, J. S.; Granick, S. *Langmuir* **2008**, *24*, 10073-10077.

(41) Petit, L.; Manaud, J.-P.; Mingotaud, C.; Ravaine, S.; Duguet, E. *Mater. Lett.* **2001**, *51*, 478-484.

(42) Fujimoto, K.; Nakahama, K.; Shidara, M.; Kawaguchi, H. *Langmuir* **1999**, *15*, 4630-4635.

(43) Petit, L.; Sellier, E.; Duguet, E.; Ravaine, S.; Mingotaud, C. *J. Mater. Chem.* **2000**, *10*, 253-254.

(44) Gu, H.; Yang, Z.; Gao, J.; Chang, C. K.; Xu, B. *J. Am. Chem. Soc.* **2004**, *127*, 34-35.

(45) Takahara, Y. K.; Ikeda, S.; Ishino, S.; Tachi, K.; Ikeue, K.; Sakata, T.; Hasegawa, T.; Mori, H.; Matsumura, M.; Ohtani, B. *J. Am. Chem. Soc.* **2005**, *127*, 6271-6275.

(46) Ye, S.; Carroll, R. L. *ACS Appl. Mater. Interfaces* **2010**, *2*, 616-620.

(47) Choi, J.; Zhao, Y.; Zhang, D.; Chien, S.; Lo, Y. H. *Nano Lett.* **2003**, *3*, 995-1000.

(48) Chen, R. T.; Muir, B. W.; Such, G. K.; Postma, A.; McLean, K. M.; Caruso, F. *Chem. Commun.* **2010**, *46*, 5121-5123.

(49) Takei, H.; Shimizu, N. *Langmuir* **1997**, *13*, 1865-1868.

(50) Lu, Y.; Xiong, H.; Jiang, X.; Xia, Y.; Prentiss, M.; Whitesides, G. M. *J. Am. Chem. Soc.* **2003**, *125*, 12724-12725.

(51) Suzuki, D.; Kawaguchi, H. *Colloid Polym. Sci.* **2006**, *284*, 1471-1476.

(52) Pawar, A. B.; Kretzschmar, I. *Langmuir* **2009**, *25*, 9057-9063.

(53) Love, J. C.; Gates, B. D.; Wolfe, D. B.; Paul, K. E.; Whitesides, G. M. *Nano Lett.* **2002**, *2*, 891-894.

(54) Pawar, A. B.; Kretzschmar, I. *Langmuir* **2007**, *24*, 355-358.

(55) Zhang, G.; Wang, D.; Möhwald, H. *Angew. Chem. Int. Ed.* **2005**, *44*, 7767-7770.

(56) Zhang, G.; Wang, D.; Mohwald, H. *Nano Lett.* **2004**, *5*, 143-146.

(57) Ling, X.; Phang, I.; Acikgoz, C.; Yilmaz, M. D.; Hempenius, M. A.; Vancso, G. J.; Huskens, J. *Angew. Chem. Int. Ed.* **2009**, *48*, 7677-7682.

(58) McConnell, M. D.; Kraeutler, M. J.; Yang, S.; Composto, R. J. *Nano Lett.* **2010**, *10*, 603-609.

(59) Jang, S. G.; Choi, D.-G.; Heo, C.-J.; Lee, S. Y.; Yang, S.-M. *Adv. Mater.* **2008**, *20*, 4862-4867.

(60) Anderson, K. D.; Luo, M.; Jakubiak, R.; Naik, R. R.; Bunning, T. J.; Tsukruk, V. V. *Chem. Mater.* **2010**, *22*, 3259-3264.

(61) Cui, J.-Q.; Kretzschmar, I. *Langmuir* **2006**, *22*, 8281-8284.

(62) Yake, A. M.; Snyder, C. E.; Velegol, D. *Langmuir* **2007**, *23*, 9069-9075.

(63) Snyder, C. E.; Yake, A. M.; Feick, J. D.; Velegol, D. *Langmuir* **2005**, *21*, 4813-4815.

(64) Charnay, C.; Lee, A.; Man, S.-Q.; Moran, C. E.; Radloff, C.; Bradley, R. K.; Halas, N. J. *J. Phys. Chem. B* **2003**, *107*, 7327-7333.

(65) Erb, R. M.; Jenness, N. J.; Clark, R. L.; Yellen, B. B. *Adv. Mater.* **2009**, *21*, 4825-4829.

(66) Jiang, S.; Granick, S. *Langmuir* **2009**, *25*, 8915-8918.

(67) Koo, H. Y.; Yi, D. K.; Yoo, S. J.; Kim, D. Y. *Adv. Mater.* **2004**, *16*, 274-277.

(68) Li, Z.; Lee, D.; Rubner, M. F.; Cohen, R. E. *Macromolecules* **2005**, *38*, 7876-7879.

(69) Cayre, O.; Paunov, V. N.; Velev, O. D. *Chem. Commun.* **2003**, 2296-2297.

(70) Cayre, O.; Paunov, V. N.; Velev, O. D. *J. Mater. Chem.* **2003**, *13*, 2445-2450.

(71) Nisisako, T.; Torii, T.; Takahashi, T.; Takizawa, Y. *Adv. Mater.* **2006**, *18*, 1152-1156.

(72) Roh, K.-H.; Martin, D. C.; Lahann, J. *Nat. Mater.* **2005**, *4*, 759-763.

(73) Nie, Z.; Li, W.; Seo, M.; Xu, S.; Kumacheva, E. *J. Am. Chem. Soc.* **2006**, *128*, 9408-9412.

(74) Shepherd, R. F.; Conrad, J. C.; Rhodes, S. K.; Link, D. R.; Marquez, M.; Weitz, D. A.; Lewis, J. A. *Langmuir* **2006**, *22*, 8618-8622.

(75) Roh, K.-H.; Martin, D. C.; Lahann, J. *J. Am. Chem. Soc.* **2006**, *128*, 6796-6797.

(76) Yuet, K. P.; Hwang, D. K.; Haghgooie, R.; Doyle, P. S. *Langmuir* **2009**, *26*, 4281-4287.

(77) Erhardt, R.; Boker, A.; Zettl, H.; Kaya, H.; Pyckhout-Hintzen, W.; Krausch, G.; Abetz, V.; Muller, A. H. E. *Macromolecules* **2001**, *34*, 1069-1075.

(78) Erhardt, R.; Zhang, M.; Boker, A.; Zettl, H.; Abetz, C.; Frederik, P.; Krausch, G.; Abetz, V.; Muller, A. H. E. *J. Am. Chem. Soc.* **2003**, *125*, 3260-3267.

(79) Gu, H.; Zheng, R.; Zhang, X.; Xu, B. *J. Am. Chem. Soc.* **2004**, *126*, 5664-5665.

(80) Tanaka, T.; Okayama, M.; Kitayama, Y.; Kagawa, Y.; Okubo, M. *Langmuir* **2010**, *26*, 7843-7847.

(81) Christian, D. A.; Tian, A.; Ellenbroek, W. G.; Levental, I.; Rajagopal, K.; Janmey, P. A.; Liu, A. J.; Baumgart, T.; Discher, D. E. *Nat. Mater.* **2009**, *8*, 843-849.

(82) Tang, C.; Zhang, C.; Liu, J.; Qu, X.; Li, J.; Yang, Z. *Macromolecules* **2010**, *43*, 5114-5120.

(83) Dupont, J.; Liu, G. *Soft Matter* **2010**, *6*, 3654-3661.

(84) Mulvaney, P.; Giersig, M.; Ung, T.; Liz-Marzán, L. M. *Adv. Mater.* **1997**, *9*, 570-575.

(85) Steve, G.; Shan, J.; Qian, C. *Janus particles*; AIP, 2009; Vol. 62.

(86) Hong, L.; Cacciuto, A.; Luijten, E.; Granick, S. *Nano Lett.* **2006**, *6*, 2510-2514.

(87) Hong, L.; Cacciuto, A.; Luijten, E.; Granick, S. *Langmuir* **2008**, *24*, 621-625.

(88) Yan, L.-T.; Popp, N.; Ghosh, S.-K.; Boker, A. *ACS Nano* **2010**, *4*, 913-920.

(89) Edwards, E. W.; Wang, D.; Möhwald, H. *Macromol. Chem. Phys.* **2007**, *208*, 439-445.

(90) Yang, S.-M.; Kim, S.-H.; Lim, J.-M.; Yi, G.-R. *J. Mater. Chem.* **2008**, *18*, 2177-2190.

(91) Walther, A.; Hoffmann, M.; Müller, A. H. E. *Angew. Chem. Int. Ed.* **2008**, *47*, 711-714.

(92) Tanaka, T.; Okayama, M.; Minami, H.; Okubo, M. *Langmuir* **2010**, *26*, 11732-11736.

(93) Sundararajan, S.; Lammert, P. E.; Zudans, A. W.; Crespi, V. H.; Sen, A. *Nano Lett.* **2008**, *8*, 1271-1276.

(94) Burdick, J.; Laocharoensuk, R.; Wheat, P. M.; Posner, J. D.; Wang, J. *J. Am. Chem. Soc.* **2008**, *130*, 8164-8165.

(95) Kim, S. H.; Jeon, S. J.; Jeong, W. C.; Park, H. S.; Yang, S. M. *Adv. Mater.* **2008**, *20*, 4129-4134.

(96) Anthony, S. M.; Hong, L.; Kim, M.; Granick, S. *Langmuir* **2006**, *22*, 9812-9815.

(97) Ozin, G. A.; Manners, I.; Fournier-Bidoz, S.; Arsenault, A. *Advanced Materials* **2005**, *17*, 3011-3018.

(98) Ismagilov, R. F.; Schwartz, A.; Bowden, N.; Whitesides, G. M. *Angewandte Chemie International Edition* **2002**, *41*, 652-654.

(99) Paxton, W. F.; Kistler, K. C.; Olmeda, C. C.; Sen, A.; St. Angelo, S. K.; Cao, Y.; Mallouk, T. E.; Lammert, P. E.; Crespi, V. H. *Journal of the American Chemical Society* **2004**, *126*, 13424-13431.

(100) Fournier-Bidoz, S.; Arsenault, A. C.; Manners, I.; Ozin, G. A. *Chem. Commun.* **2005**, 441-443.

(101) Kline, T. R.; Paxton, W. F.; Mallouk, T. E.; Sen, A. *Angew. Chem. Int. Ed.* **2005**, *44*, 744-746.

(102) Zhang; Glotzer, S. C. *Nano Letters* **2004**, *4*, 1407-1413.

(103) Heath, J. R.; Vossmeyer, T.; DeIonno, E.; Markovich, G. In *Nanostructured Materials*; American Chemical Society: 1997; Vol. 679, p 1-6.

(104) Jonathan, R. H.; Richard, A. L. J.; Anthony, J. R.; Tim, G.; Reza, V.; Ramin, G. *Phys. Rev. Lett.* **2007**, *99*, 048102.

(105) Ke, H.; Ye, S.; Carroll, R. L.; Showalter, K. *J. Phys. Chem. A* **2010**, *114*, 5462-5467.

(106) Ye, S.; Carroll, R. L. *manuscript submitted*.

(107) Ye, S.; Carroll, R. L. *manuscript submitted*.

Chapter 2

Bimetallic Janus Particles

2.1 Background

"Janus" particles are particles having two different materials on opposite faces.[1] Due to their unique structures, they have a wide range of potential applications in drug delivery, microfluidic systems, optical biosensors, and electronic devices.[2-7] A primary feature of all Janus particles is anisotropy, whether due to the presence of a chemically or physically asymmetric structure. The availability of two or more different materials in one single unit would allow varied physical or chemical functionalities. Structurally, Janus particles may be considered as unique building blocks to prepare advanced ordered structures based upon their anisotropic attributes.[8-13] In addition, the surface multi-functionality of Janus particles provides potential uses in surface assembly and cargo transport. Of particular interest is recent work demonstrating that Pt-silica asymmetric particles and bimetallic nanorods undergo autonomous motion due to the conversion of stored chemical energy to mechanical movement without external intervention, which is promising to apply these self-propelled devices as micro- or nano-scale engines for targeted cargo transport.[14-16] One of the driving forces behind our research on bimetallic Janus particles was to produce analogous spherical materials.

Currently, there are many methods to prepare Janus particles for various purposes.[2,17-40] In section 2.2, a novel approach is developed in our laboratory to prepare bimetallic Janus particles, comprised of silica particles with different metals on opposite hemispheres. These bimetallic Janus particles have been thoroughly characterized by scanning electron microscopy (SEM) and energy dispersive X-ray spectroscopy (EDS), which indicate that all silica beads are capped with two different metals, typically leaving an equatorial belt around the particle composed of uncoated silica. Subsequent possible chemical modification and transformation of these bimetallic Janus particles would provide increased functionality. For instance, metals on the Janus particle can be transformed by heterogeneous phase reactions to form other species. This transition is expected to prepare new types of Janus particles with different electronic, optical, and magnetic properties.

In section 2.3, the structure of metal coatings deposited on the particle surfaces is investigated in order to understand the formation of the equatorial silica belts. In

addition, the 3D metal dot arrays on flat substrates were prepared through geometrically structured dynamic shadowing lithography (GSDSL), and the evolution of these 3D structures was characterized using scanning electron microscopy (SEM) and atomic force microscopy (AFM) in order to visualize structural features of individual morphological structures. This experimental work, including development of a numerical model of shadowed growth, is aimed to broaden the scope of nanosphere lithography, providing new insights into fabrication of structures using SL.

2.2 Experimental

2.2.1 Fabrication of Bimetallic Janus Particles.

A typical approach to make bimetallic Janus particles using electron beam vacuum evaporation is described below (Figure 2-1). Uniform silica submicro- and microspheres were purchased from Bangs Laboratories, Inc. As an initial support, glass substrates were treated with piranha solution (H_2O_2:H_2SO_4 = 1:3) to form a hydrophilic surface. The substrates were immersed in the piranha solution for 30 minutes, then rinsed with DI water, and finally dried in a stream of dry nitrogen. After drying, delivery of a drop (~20 μL) of a suspension of beads (~1% solids) to the surface produced a predominately close-packed monolayer of beads on the glass substrate. Whether the particles form monolayer or multilayer can be easily differentiated through the optical microscope or by the diffraction difference from the substrate surface. The self-assembled beads on substrate were placed in the vacuum chamber of the e-beam evaporator with the substrate plane perpendicular to the metal vapor source, and then coated with one selected metal. Metal evaporation was performed on an electron-beam evaporator (Temescal BJD-2000). After evaporation, the metal half-coated beads were adhered to an adhesive support (the adhesive support was mounted on a flexible substrate, attached to a cylindrical vial, then roll over the evaporated particles), the flexible substrate was then detached and mounted on a flat substrate. The inverted particles on the support were placed again in the vacuum chamber with the bare silica hemispheres orienting to the metal vapor source, then deposited a thin film of another metal, typically 20 nm thick, through e-beam evaporation. Finally, the beads were released from their support by sonication in acetone, washed with acetone three times,

and then re-suspended in water. Various combinations of different metals have been successfully deposited on opposite sides of the silica beads to form bimetallic Janus particles. Metals that have been used include gold, platinum, silver, nickel, cobalt, and aluminum. Titanium was added as intermediate adhesion layer between gold and silica – other metals were used with no adhesion layer. For instance, 4 μm Au/Pt bimetallic Janus particles were produced by evaporation of 5 nm thick Ti and 20 nm Au on one side and then 20 nm Pt on the other.

2.2.2 Plasma oxidation of bimetallic Janus particles.

A droplet (100 μL) of bimetallic Janus particles aqueous solution was dried onto a clean silicon substrate. The plasma oxidation reaction was carried out in a radio frequency air-oxygen plasma cleaner chamber (Harrick PDC-3XG, 100 W) for 30 min.

2.2.3 Preparation of 3D metal dot arrays.

To study the evolution of these structures, an increasing thickness of metal was deposited on two different bead sizes via electron beam evaporation. A monolayer of silica beads of either 865 ± 7 nm or 143 ± 7 nm in radius was deposited onto a clean glass substrate, then gold of nominal thickness ranging from 5 to 500 nm (as measured by a quartz crystal resonator) was deposited on the bead monolayer using electron beam evaporation at pressure of ~10^{-5} torr (Temescal BJD-2000).

2.2.4 Characterization.

Scanning electron microscopy (SEM, JEOL JSM-6490LV) was used to image the particles at each step of the procedure. An energy dispersive X-ray spectroscopy (EDS or EDX) detector coupled with SEM was used for elemental analysis. X-ray photoelectron spectroscopy (XPS, Phi 5000 Versaprobe, monochromated Al Kα source) was used to characterize the oxidation state of metals after air-oxygen plasma exposure. Binding energies of XPS spectra were corrected by referencing the C 1s signal of adventitious hydrocarbon to 284.8 eV. Fourier transform infrared spectroscopy (FTIR) measurements were performed at 1 cm^{-1} resolution averaged over 16 scans. The bead monolayer was stripped from samples using adhesive tape, and the height and morphology of the

resulting SL-defined structures were analyzed by SEM and AFM (Asylum Research MFP-3D).

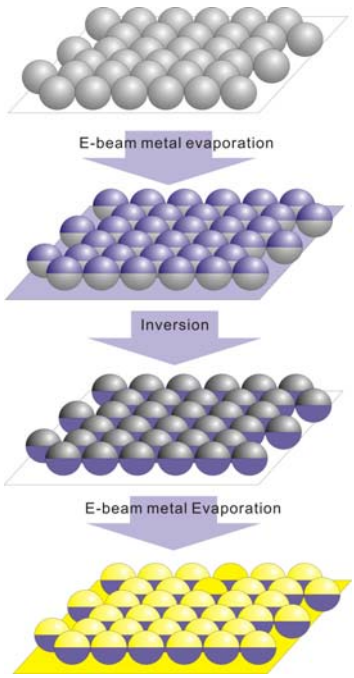

Figure 2-1. Schematic strategy to create bimetallic Janus particles. This strategy includes (1) e-beam evaporation; (2) inversion; (3) e-beam evaporation; and (4) dispersion.

2.3 Design and fabrication of bimetallic Janus particles (BJPs)*

A schematic representation of four-step approach to fabricate the bimetallic Janus particles is summarized in Figure 2-1. A single layer of self-assembled silica beads are coated with one metal using e-beam evaporation. The beads are then inverted, and coated with another metal. Finally, the formed bimetallic Janus particles are dispersed in solution by sonication. As shown in Figure 2-2a, the self-assembled monolayer of 1 μm silica particles were deposited with 5 nm of titanium and then 20 nm of gold. Metal evaporation caused no apparent damage to the packing of the beads. Note that "shadows" formed underneath the spheres during the process of e-beam evaporation (Figure 2-2b). In contrast to metal deposition by sputter coating, e-beam evaporation is a ballistic

* Part of this work is published on ACS Applied Materials & Interfaces (2010).

process, in which atoms emitted from the source crucible travel in straight lines in vacuum and uniformly coat the metal in a line-of-sight fashion onto beads, producing a "shadow" of metal on the substrate. This is due to the mean free path at vacuum (~10^{-5} torr) is greater than the distance between the sample substrate and metal source. In addition, only the top surface of the particle is coated with a thick layer of metal – because of the bead curvature, the metal thickness decreases as the "equator" of the bead is approached. The metal half-coated silica particles were dispersed in water and dried on a silicon substrate. Clear phase boundaries visible by SEM imaging easily differentiate the metal hemisphere from the silica (Figure 2-2c).

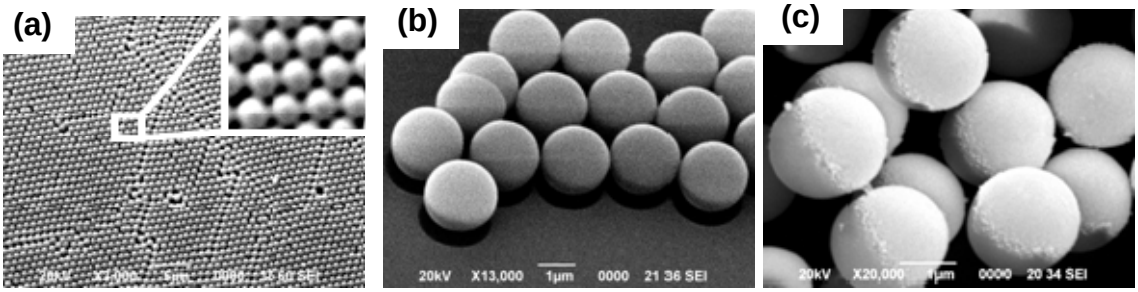

Figure 2-2. SEM images are shown of (a) hexagonally packed silica beads after first metal evaporation with gold with titanium used as adhesion layer (inset shows higher magnification view of the layer); (b) half-gold-coated silica beads on a 40°-tilted sample stage; (c) individual half-gold-coated silica beads. Scale bars 5 μm (a), 1 μm (b) and 1 μm (c).

An important requirement for successful fabrication of double-faced Janus particles was the identification of an appropriate adhesive substrate used to "flip" the beads. Three criteria were considered – adhesion to beads, heat tolerance and release characteristics. Adhesion to beads should be sufficient to pick up the submicron structure and hold them securely, but should not have a permanent effect on the metal already evaporated on the surface. The second evaporation of metal occurs with beads stuck on the adhesive substrate, so it must tolerate temperatures up to 150 ^{o}C (as measured inside the e-beam evaporation chamber during evaporation). Release characteristics were important in that an adhesive that did not release the beads would render them useless, and if the adhesive material remained adsorbed to the beads, it would interfere with the

desired properties, either by occluding the surface or adhering beads together. Ideally, the adhesive should be completely soluble in solvent or removable by other processes, leaving uncontaminated Janus particles.

Many adhesive substrates were tried, including commercial double-sided tapes, carbon tape used as a conductive adhesive for samples in SEM, epoxies, and sparingly cross-linked polydimethylsiloxane. The best substrate we have identified to invert the beads was the commercially available double-sided adhesive copper tape (Electron Microscopy Sciences, cat. # 77802-22), commonly used as a conductive adhesive for SEM substrates or EM shielding applications. Over 90% of beads on a substrate can be picked up by a single application of the copper tape. Most of the beads remained on the original substrate were from the secondary layers. As shown in Figure 2-3, the inversion process had no obvious effect on the packing of the beads but caused slight orientation change for a small portion of the beads. The copper tape adhesive is tolerant of the elevated temperature, showing no deformation or distortion over long periods of e-beam evaporation. Importantly, the acrylic adhesive on the tape is very soluble in acetone, providing a facile route to remove the beads from the substrate. Simple sonication in a solution of acetone releases the beads from the copper tape, and solvent washing with acetone produces Janus particles with no trace of adhesive adsorbed, as indicated by IR and XPS spectroscopy (Figure 2-4 and 2-5).

The FT-IR spectra shown in Figure 2-4 indicates that, though the silica bead spectrum obscures the region from 650-1300 cm^{-1}, the peaks at 1375 and 1450 cm^{-1} (assigned to methyl bending vibrations), 1735 cm^{-1} (assigned to an aliphatic C=O stretch) and 2875-2960 cm^{-1} (due to the C-H stretches) are completely consistent with those observed from the adhesive alone. Their presence in the beads before any exposure to adhesive is consistent with the ubiquitous hydrocarbon contamination. However, these peaks are virtually absent in the washed beads, indicating a complete removal of the adhesive from the particles by purification in acetone. As shown in the XPS spectra in Figure 2-5, the peak at 284.8 eV likely arises from atmospheric hydrocarbon contamination (primarily sp^3). The peak at ~287.1 eV corresponds to additional hydrocarbon sources, indicating the presence of adhesive. The disappearance of this

shoulder peak after purification indicates the successful removal using our approach, which is consistent with the IR results.

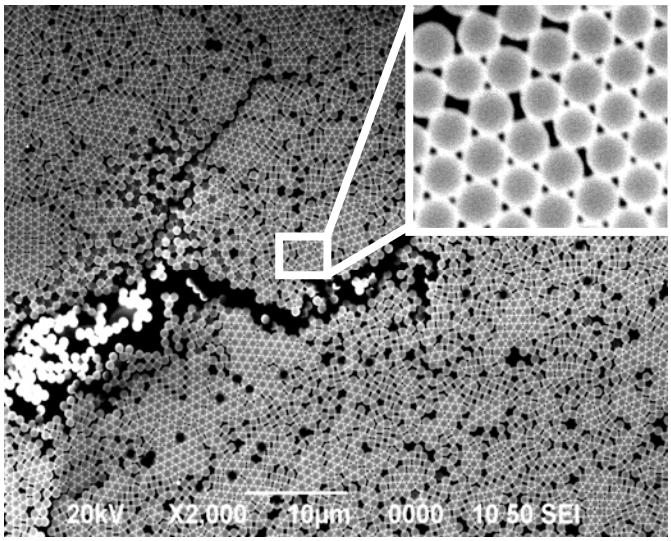

Figure 2-3. Half-gold-coated silica beads inverted on the copper tape followed by evaporation of 20 nm thick platinum (inset shows higher magnification view of the layer). Scale bar: 10 μm.

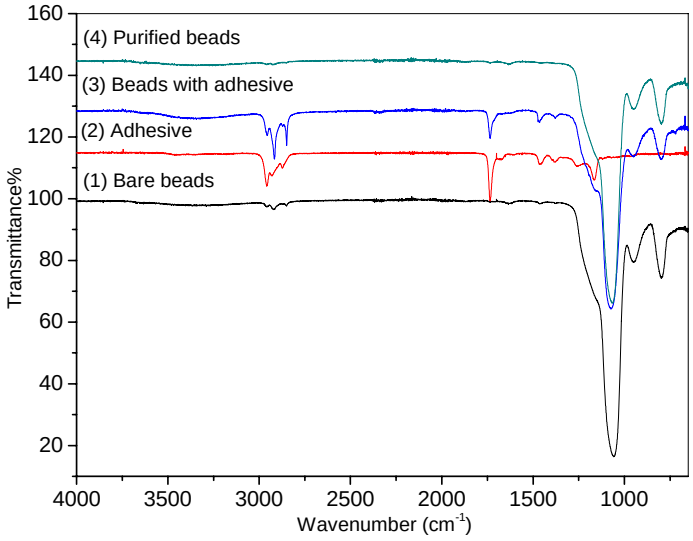

Figure 2-4. ATR-FTIR spectra of (1) silica beads before adherence to tape, washed with water; (2) acrylic adhesive, dissolved in acetone, and deposited on ATR crystal; (3) silica beads after release from tape, with no additional efforts to remove adhesive; (4) silica beads released from tape, purified by washing 3x with acetone.

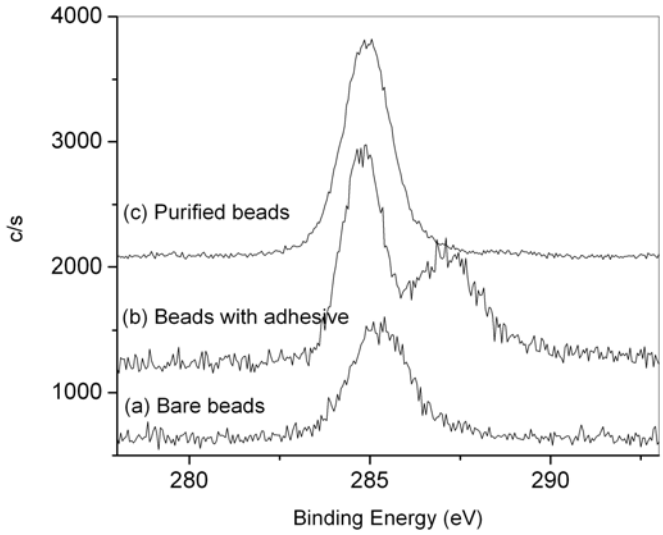

Figure 2-5. XPS spectra of the C 1s peak on: (a) bare silica beads; (b) silica beads after release from tape, with no additional efforts to remove adhesive; and (c) silica beads purified by washing 3x in acetone.

Silica beads of sizes ranging from 0.8 μm to 4.0 μm in diameter have been successfully inverted and evaporated with two different metals. Initial expectations were that the silica beads would be fully covered by two metals, one on each side, with an overlap or contact between the metals at the equatorial ring around the particles. As described above, however, the deposited metal thins as the equatorial region of the bead is approached. The structure of the metal coating on the particles will be discussed in details in the subsequent section. With metals deposited on both sides, both metal coatings become thin to nonexistence at the equator, leaving an uncoated belt of silica on each bimetallic Janus particle. EDS mapping verified this result, demonstrating that the metals do not fully coat on the bead hemisphere. Figure 2-6 shows a typical SEM image and EDS mapping result of those Au/Pt bimetallic Janus particles that are made with our approach. As indicated in Figure 2-6a, the edge of Au tends to be smooth and extends to the equator whereas the edge of Pt remains sharp, and the size of metal "cap" is smaller. This is due to the presence of Ti as an adhesion layer; Ti adheres more favorably to the silica substrate than Au and Pt, and acts to improve their adhesion, and therefore, reduces the interfacial energy between the silica and Au (or Pt).[41] We have found that the addition of Ti in between Pt and silica also improved the wettability of Pt, and thus narrowed the

belt gap between two capping metals. To further understand the interfacial interaction between metals and the silica substrate, the effect of metal deposition rate, local temperature at the substrate surface during deposition, curvature of the surface, and the effect of surface chemistry on the total coverage of the metal on the silica particles need to be further investigated. From the SEM image shown in Figure 2-6a, the silica particles appeared to be coated with two metals on opposite hemispheres, leaving unmodified silica belts around the equatorial region. The colored mapping results, along with the EDS spectrum in Figure 2-6b, indentify the two metals on each bimetallic Janus particle, and verify the presence of the uncoated equatorial silica belts.

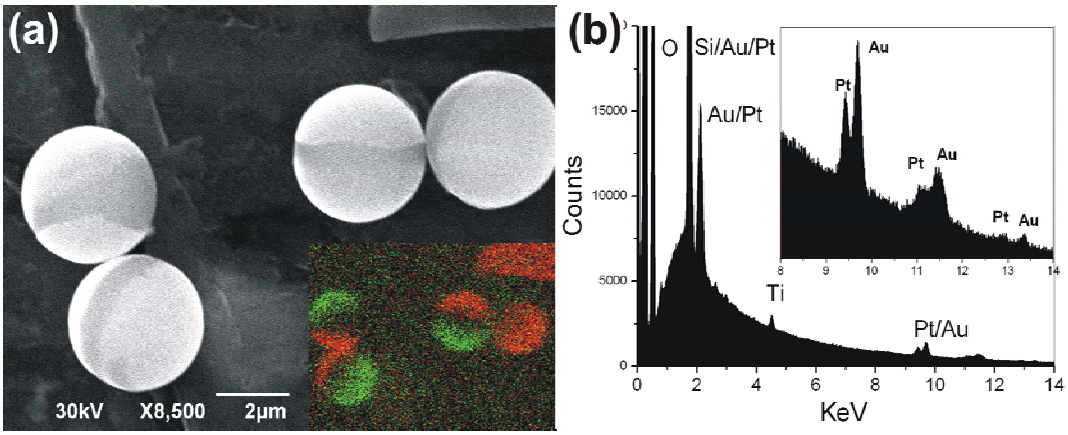

Figure 2-6. SEM image and EDS mapping results for 4 μm Au/Pt bimetallic Janus particles (Ti as adhesion layer between Au and SiO_2); (a) secondary electron image, inset: EDS mapping indicating Au (green) and Pt (red); Scale bar: 2 μm. (b) X-ray energy dispersive spectrum, inset: enlarged region of the EDS trace.

This approach through e-beam evaporation seems to be generally applicable for any metal which can be deposited by evaporation. A broad variety of metals, including ferrous metals, reactive metals, and noble metals have been used to fabricate various combinations of bimetallic Janus particles. Analysis of the resulting particles by SEM and EDS clearly indicates the presence of two metals, one at each hemisphere of the silica beads with uncoated equatorial silica belts. An additional example of SEM imaging and EDS mapping for Co/Ni bimetallic Janus particles is shown in Figure 2-7. The 4 μm Co/Ni bimetallic Janus particles were clearly visualized with a silica belt gap between Co

and Ni in Figure 2-7a. The corresponding EDS mapping result (Figures 2-7a inset and 2-7b) confirmed the particle composition, the locations of the metals and the silica belts.

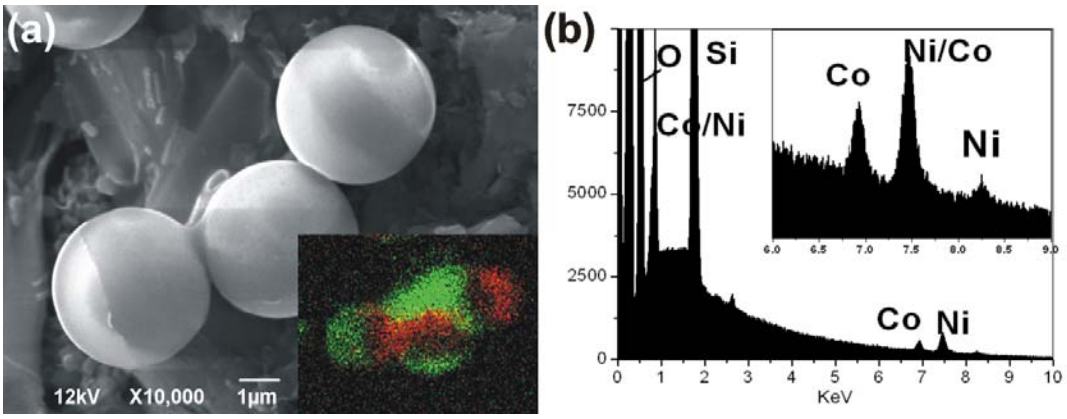

Figure 2-7. SEM image and EDS mapping results for 4 μm Co/Ni bimetallic Janus particles; (a) secondary electron image, inset: EDS mapping indicating Ni (green) and Co (red); Scale bar: 1 μm. (b) X-ray energy dispersive spectrum, inset: enlarged region of the EDS trace.

A potential advantage of these bimetallic systems is that selective chemical modification of each of the metals and the silica belt can facilitate multifunctional materials. This would be useful in fabrication of novel anisotropic building blocks and study of assembled complex structures. Possible modifications include chemical adsorption, formation of self-assembled monolayers, covalent coupling, and chemical transformation of metals into other materials, which is demonstrated in Chapter 3. Here, transformation of metal surfaces to metal oxides through direct exposure of the Janus particles to air-oxygen plasma is demonstrated. Due to their ease of oxidation, thin films of Ag, Ni, Co, and Al are susceptible to air oxidation, and spontaneously transform, at least in part, into corresponding metal oxides. Direct heterogeneous oxidation reactions were performed by exposing bimetallic Janus particles to radio frequency-generated air-oxygen plasma for several minutes. The metal oxides are marked by changes in composition, but also by changes in morphology and structure. For example, the SEM images shown in Figure 2-8a and 2-8b demonstrate the corresponding morphological change of Ag to Ag_2O on Ag/Au bimetallic Janus particles before and after plasma exposure, respectively. The silver coating changed into needle structures after oxidation,

forming silver oxide. The Ni/Au bimetallic Janus particles, however, do not show any significant change in morphology upon exposure to oxidation (Figure 2-8c and 2-8d).

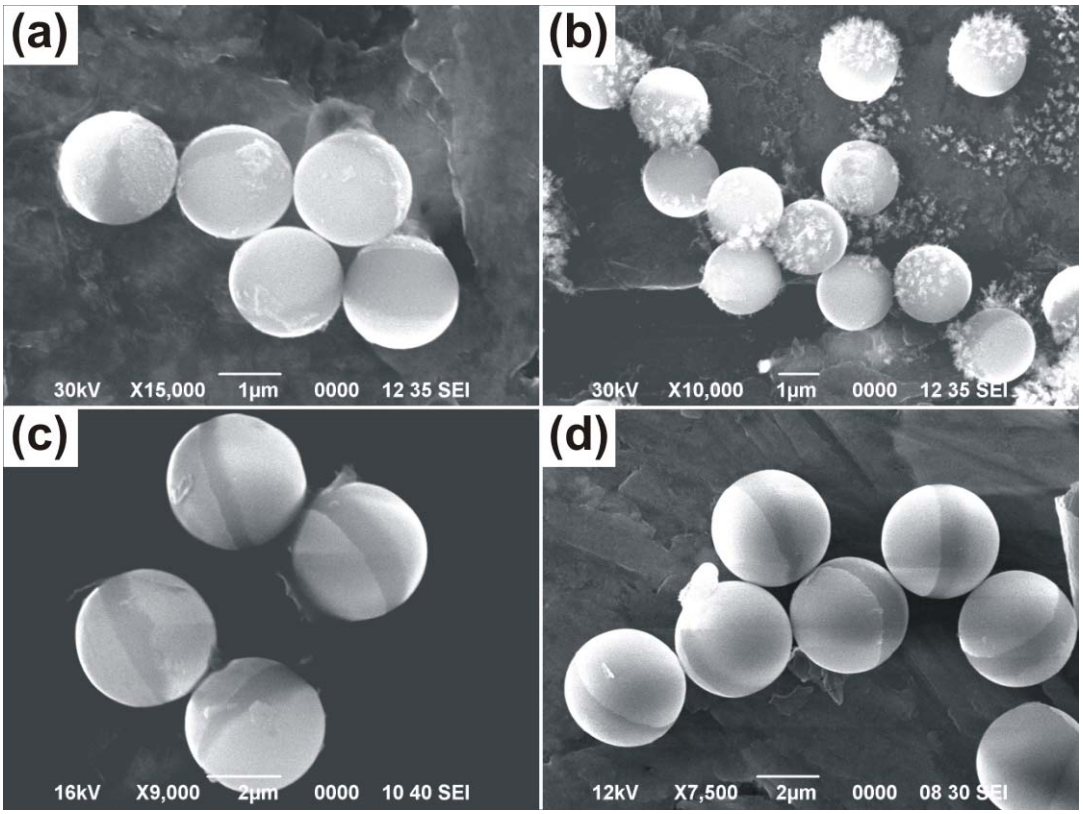

Figure 2-8. SEM images of 2 μm Au/Ag bimetallic Janus particles (a) before and (b) after oxygen plasma exposure and 4 μm Au/Ni bimetallic Janus particles (c) before and (d) after oxygen plasma exposure. Scale bars: 1 μm (a, b) and 2 μm (c, d).

XPS indicates transformation to the oxide, but randomly oriented bimetallic Janus particles show SiO_2 making assessment of extent of transformation difficult. Thus, a simpler system, of the metals on flat substrates was used to understand the transformation processes. Characterization by XPS of silver and nickel films (20 nm) on flat silicon substrates exposed to oxygen plasma for same amount of time clearly indicates the occurrence of oxidation reaction due to the presence of an intensified oxygen peak and the binding energy shift of metal peaks (Figure 2-9). The SEM images verify the similar morphological change of both Ag and Ni thin film on the flat surface. Due to the discrete feature of the formed silver oxide, the increased oxygen signal after oxidation is most likely due to the exposed silica surface and oxidized silicon substrate surface (Figure 2-

9a). However, the binding energy of the Ag 3d peaks shifted to lower binding energy side, indicating the change in the oxidation state of the metal (Figure 2-9b). After oxidation, the nickel thin film appeared no apparent morphological change but both the increased oxygen signal and the observed shift in the binding energy of Ni 2p from the XPS spectra (Figure 2-9c, d) confirmed that the oxidation occurred to the nickel film, at least on the surface.

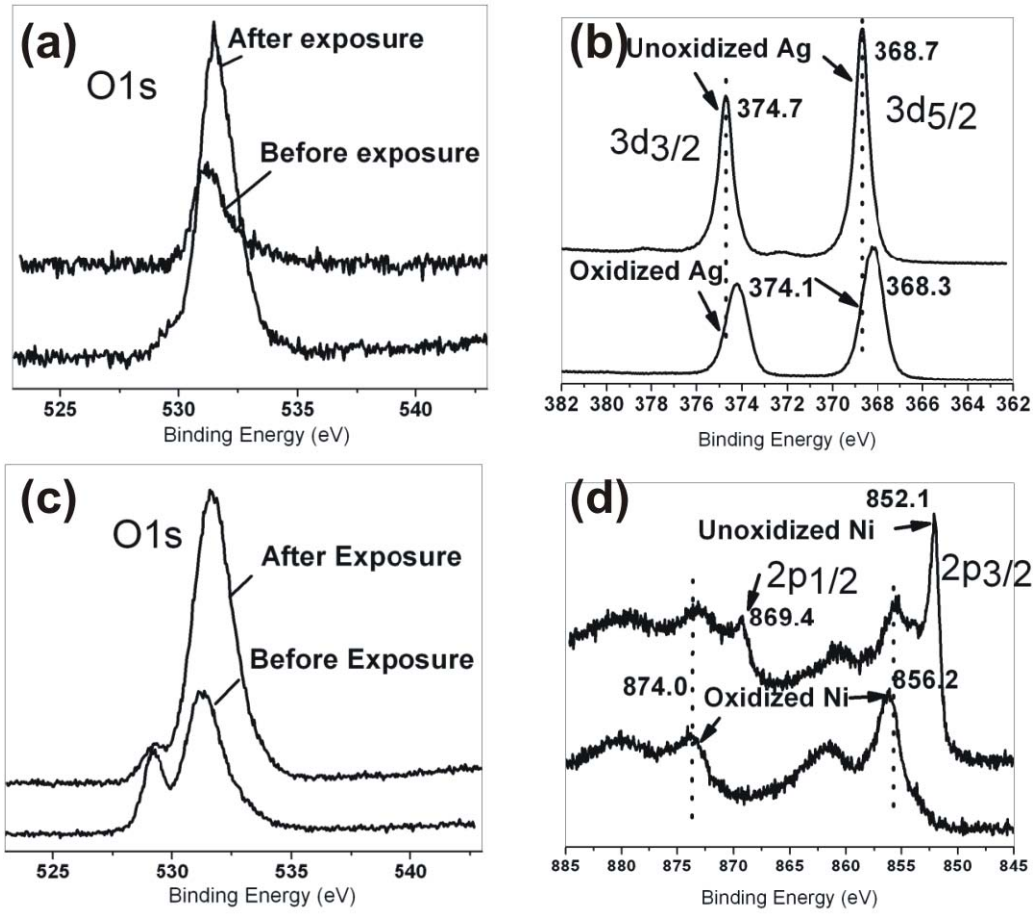

Figure 2-9. XPS patterns of thin film Ag (a, b) and Ni (c, d) on Si (111) after oxygen plasma exposure.

In summary, a simple approach has been applied to fabricate bimetallic Janus particles, which are comprised of colloidal silica particles, capped with various metals on opposite faces, leaving an uncoated equatorial silica belt around the particle. Chemical transformation of bimetallic Janus particles with some of the metals (silver, nickel) can

be achieved simply by heterogeneous oxidation reaction to form metal-metal oxide type of Janus particles. Other chemical transformation approaches are possible to convert the BJPs to other types of Janus particles for other applications. The presence of the uncoated silica belt also provides an opportunity to assemble various useful functionalities. We believe the bimetallic Janus particle can be applied to a variety of fields, such as photochemistry, photocatalysis, device photonics, and novel magnetic and semiconductor materials.

2.4 Fabrication of 3D Metal Dot Arrays by Geometrically Structured Dynamic Shadowing Lithography (GSDSL)[†]

Nanostructures and nanoparticles, which comprise with an assembly of atoms into clusters with dimensions and periodicity on nanometer scale, attract enormously widespread interest due to their size-dependent nonlinear properties. Such nanostructured materials are becoming increasingly important for advanced performance and enhanced functionality in microelectronics, data storage, communications industries, and sensor devices. Sophisticated new laboratory techniques allow researchers to fabricate, measure and manipulate matter on the nanoscale.[42,43] There are many difficult challenges remaining in translation of effective laboratory techniques for generation of nanoscale features into processes suitable for fabrication facilities and large-scale chip and device manufacturing. The most notable are the control of critical dimensions in extremely small feature sizes, and the increase of throughput for high resolution processes.[44,45] Conventional and developing approaches, including photolithography, extreme ultraviolet lithography, X-ray lithography, electron beam lithography and other techniques, provide an optimistic view for the development of new processes.

Optical lithographic techniques, or photolithography (PL),[46] is the predominantly utilized tool in the manufacture of microelectronic circuitry. PL employs an energy source (for example, an ultraviolet light source) to transfer a geometrical pattern from a mask to a photosensitive polymer, or photoresist, which accurately facilitates transfer of

[†] Part of this work is published on Langmuir (2011).

the pattern into an underlying substrate (through etching or ion implantation), or which acts as a mask for the deposition of subsequent materials (such as metals or dielectric materials). Due to physical limitations arising from diffractive effects, the smallest feature size that photolithography can produce is comparable to the wavelength of light used, necessitating continuous expensive shifts towards shorter wavelength light sources and resolution enhancement techniques.[47,48] Next generation lithographic techniques, which take advantage of shorter wavelength light sources, including extreme ultraviolet and X-ray lithography, as well as electron beam lithography are being actively explored to lower resolution constraints and further reduce the critical dimension of possible structures.

Extreme ultraviolet (EUV) lithography[49,50] is considered as the most promising next generation lithographic technique in large scale integrated circuits production for replacing more conventional optical lithography. With the short wavelength of 13.5 nm, EUV lithography may realize structures smaller than 20 nm with high yield and productivity. While fundamentally very similar to conventional PL processes, EUV lithography faces unique challenges such as production of a high power light source and a defect-free mask, which keeps delaying this long-anticipated printing method from being adopted as the industrial standard.

Another burgeoning technique is X-ray lithography (XRL),[51,52] in which collimated X-rays illuminate the thin membrane mask held in close proximity to the substrate surface, which serves to absorb and transmit the X-rays in a designed pattern, 'printing' the pattern from the mask to the substrate. The X-ray wavelength in XRL (0.4 nm) results in very high resolution from proximity printing. XRL approaches under development are characterized by parallel production of minimum feature sizes of 10-20 nm; however, high capital costs and special mask and resist requirements are significant impediments to implementation of large-scale XRL.[53]

In electron beam lithography (EBL),[54-56] a highly focused electron-beam exposes a resist coated on a substrate, directly producing patterns on surfaces. The high energy (and thus short wavelength) electrons used in EBL provides much higher patterning resolution (~10 nm) than is possible with diffraction-limited conventional PL.

Limitations to resolution of EBL arise from scattering of electrons in the resist and through aberrations present in electron optics. The primary drawback of EBL is the (currently) direct-write serial nature of available systems, limiting throughput; this is one of the primary focus areas for research and development in improving EBL capabilities.

The recent development of several other conventional lithographic approaches demonstrates great promise for the fabrication of patterned structures with feature sizes in the nanoscale regime. These include nano-imprint lithography,[57-59] near field optical lithography,[60-62] interference lithography,[63,64] and scanning tunneling microscopy[65,66] and atomic force microscopy lithographic techniques.[43,67,68] These techniques have produced, in many cases, single nanometer resolution, or even lower, but at the expense of impractically low throughput. Nanosphere lithography, or sphere lithography stands out as a possible alternative, highly parallel lithographic technique, based on a completely different principle and under active exploration.

Nanosphere lithography (NSL)[69-72] was pioneered in the work of van Duyne et al., who systematically investigated the size-dependent optical properties of nanoparticles and developed NSL materials in the field of chemical and biological nanosensors. The use of larger template spheres, up to microns in diameter, is more properly called sphere lithography (SL), and will be referred to as such. In general, SL involves three major steps: (1) self-assembly of size monodisperse micro- or nanospheres to form a 2D colloidal crystal as deposition mask on a flat substrate; (2) deposition of selected lithographic material onto the colloidal crystal, and, through the openings between packed particles, onto the substrate; (3) removal of the colloidal array, leaving behind the deposited material on the substrate as micro- or nanostructures (denoted as the SL array). Figure 2-10 illustrates the simplest scenario of SL using a single layer of hexagonally closest packed spheres as the deposition mask. Note that particles in a hexagonally closest packed configuration produce triangular holes between adjacent particles, resulting in triangular features on the substrate. Alternative arrangements of particles (such as cubic or binary packing) would generate SL arrays of different configurations, but would require field interaction or templating to form under normal circumstances. In Figure 2-11 the FE-SEM images show a close-packed single layer of silica particles as the deposition mask and the resulting triangular structures remaining after removal of the

silica particles. The size of the triangular SL array structures and the interparticle spacing can be geometrically predicted with known sphere diameter, allowing some degree of tunability to the system. Double layers of sphere templates could be also prepared through control of the sphere deposition process and other parameters, leading to a six-fold regular pattern of hexagonal SL arrays at smaller coverage. Only the triangular SL arrays formed by deposition through single layer SL masks will be our interest and focus in this section.

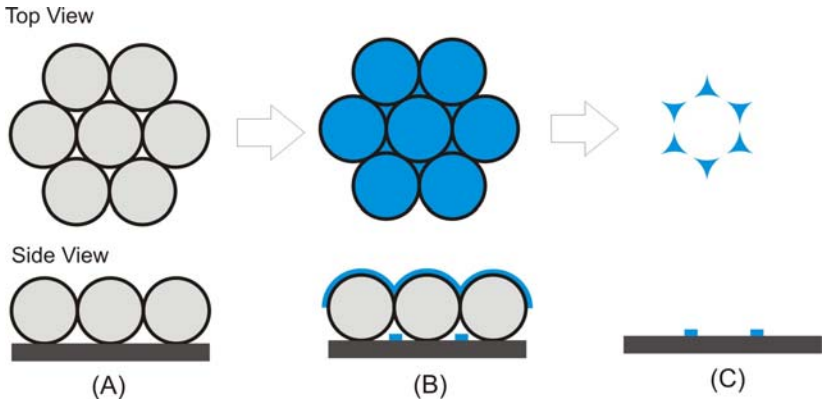

Figure 2-10. Schematic illustration of nanosphere lithography. (A) A monolayer of hexagonally close-packed spheres serves as a shadow mask. (B) A metal or other material deposited from a source normal to the substrate through the SL mask. (C) An array of triangularly shaped structures with P_{6mm} symmetry remains on the substrate after removal of the SL mask.

In addition to production of two-dimensional periodic particle arrays with controlled size, shape and interparticle spacing, SL also serves as a versatile nanofabrication tool featured with general materials applicability, high throughput, elegance of simplicity, and relatively low cost. Within the past two decades, a broad range of inorganic and organic materials have been used as lithographic source to fabricate SL arrays of nanostructures. These include metals,[69-71,73-79] metal oxides and halides,[70,80-83] semiconductors,[84,85] organometallics,[70] and hydrocarbons.[86] In addition, the effects on the array structure, feature shape, optical and chemical properties, caused by the substrate material,[87] the external dielectric medium,[88] and the adsorbed self-assembled monolayer,[89] have been thoroughly investigated. Equilateral triangular

nanostructures are the typical motif in the process of SL; other geometries, including distorted triangular structures, chains,[90] rings,[79,86,91] spheroids,[73] nets[92] or nanograils[93] can be attained by the proper selection of materials, variation of the incidence flux angle, multiple depositions, and post-treatment of the SL arrays. Combined with reactive ion etching, the SL arrays can be used as etch masks to generate nanostructures with high aspect ratio such as nanowells[94,95] and nanopillars.[84,96] The flexible control in both size and shape of the prepared structures facilitates the broad use of SL to study the size- and shape-dependent optical, magnetic, electronic, and catalytic properties of materials.

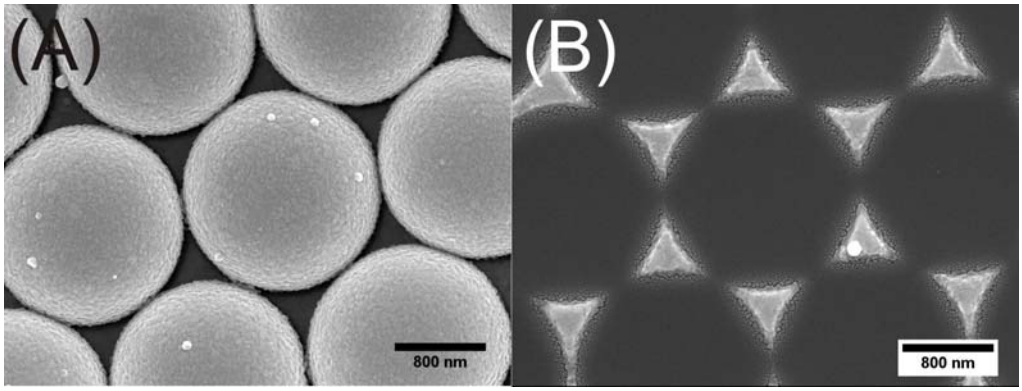

Figure 2-11. FE-SEM images: (A) single layer of hexagonally closest packed 865 nm silica particles after deposition with 100 nm of gold; (B) corresponding triangular structure array after removal of the mask.

A great portion of previous SL/NSL research was focused on the fabrication of noble metal nanostructure arrays, such as gold and silver, due to their unique optical properties, including localized surface plasmon resonance.[69,71,97-102] These substrates have been found to be effective for surface enhanced Raman spectroscopy,[103-106] chemical and biological sensors, and optical devices.[107-116] SL has also been employed as a powerful fabrication tool to pattern polymers,[117] proteins[118] and carbon nanotubes.[119,120]

Use of SL-defined features for single molecule detection and surface enhanced spectroscopy has been a significant area of study. Well-defined, easily produced three dimensional particles on a substrate also have other potential impact areas. Structured bi- and multi-metallic materials have shown potential as catalysts for hydrogenation reactions,[121] and SL-defined arrays of these materials would have exciting potential in

screening new heterogeneous catalysts. Layered electronic and optical devices, including ferroelectrics, multiferroics, and semiconductor quantum well structures have great potential in next-generation computational and storage devices, but are challenging to fabricate on large scales.

Since most research in SL systems has focused on two dimensional arrays, insufficient understanding of the vertical growth of the SL features exists. In this section, the preparation of vertically structured metal dot arrays by geometrically structured dynamic shadowing lithography (GSDSL), with particular focus on the structural evolution of features in this system, is demonstrated. Changes in the SL mask over the course of an evaporative deposition allow controlled variation in the resulting feature size and shape. An empirically derived model of structural growth is developed to compare features at two different length scales. The nomenclature, geometrically structured dynamic shadowing lithography, demonstrates similarities to other shadow-masking lithographic fabrication techniques, but our emphasis is on the dynamic shadowing effect and its consequence toward the 3D nanostructure. The experimental work, as well as the numerical model of shadowed growth, is aimed to broaden the scope of SL, providing new insights into fabrication of structures and resulting in new applications.

Growth Model

In SL, a mask is formed from a monolayer of colloidal spheres, through which a metal or other material is deposited onto the substrate, forming an array of periodic patterned structures. The techniques used to deposit materials in SL are typically thermal evaporation, electron beam evaporation, sputter coating, pulsed laser deposition, or chemical vapor deposition.[122] E-beam evaporation is a line-of-sight deposition technique. In e-beam evaporation, a target anode is bombarded with a pre-aligned rapidly rastering electron beam of high energy, which melts and vaporizes or sublimes material under the e-beam. The vaporized material travels ballistically through the vacuum (typically 10^{-4}-10^{-5} Pa) to the substrate, where the metal vapor condenses to form a solid film on the substrate. In a typical e-beam evaporation configuration, the angle of vapor flux is normal to the substrate plane. The result is that only the substrate which is in direct line-

of-sight to the source material receives the material vapor is deposited, forming a "shadow" of the mask.

In SL, the mask is made of a hexagonally close-packed monolayer of silica colloidal spheres, in which the triangular interstitial holes are formed by three adjacent spherical particles in contact with one another, and sitting on the substrate. To form metal structures, a metal is used as the vaporization source. During the process of metal deposition, part of the metal vapor deposits on the silica spheres while the other part travels through the mask and into the interstitial holes, depositing on the substrate below the silica spheres. For low amounts of metal deposition, the accumulation of the metal leads to triangular-shaped structures, following the pattern of the masking interstitial holes on the substrate. Under high resolution imaging, the shape of the deposited area is found to be the same as the projection of an interstitial hole onto the substrate, which are equilateral "triangles" with three arcs as the edges, instead of straight lines (Figure 2-11B and 2-12A). An increase in the thickness of the deposited material creates a pseudo-trigonal prism structure (Figure 2-12B). This "trigonal prism" is the ideal situation occurring when the features of the mask are faithfully duplicated onto the substrate, and in the limit of very thin metal deposition, represents a reasonable estimate of the SL-derived structure.

With increased metal thickness, however, the initial thin film planar structures grow normal to the substrate plane. However, the predicted structure in Figure 2-12C is not the result. Notably, when larger amounts of metal are deposited through a shadowing mask, growth of the film normal to the substrate is accompanied by metal deposition laterally on the masking structure, reducing the masked feature size. The growth of the metal in a lateral direction perpendicular to the vapor flux is a fundamental phenomenon, which for a given material and substrate is dependent on the angle of vapor flux relative to the substrate.

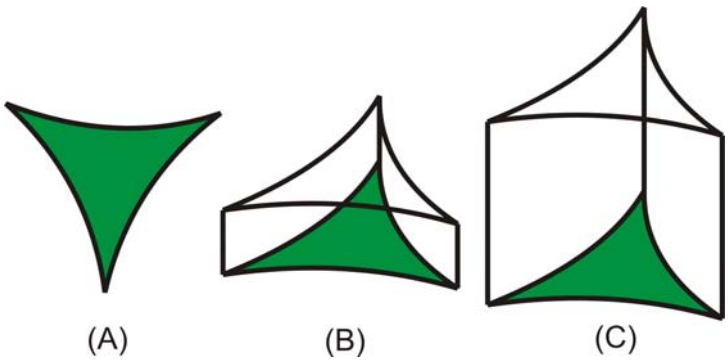

Figure 2-12. Schematic illustration of a typical structural transition beginning with an initial pseudo-triangularly shaped structure (A), and then growing into idealized pseudo-trigonal prisms with difference in height (B, C) in an SL-masked electron beam deposition. The height of the trigonal prism is related to the deposited thickness of evaporative material.

Control of the lateral growth of deposited material has been exploited to produce materials in glancing angle deposition and oblique angle deposition.[123-125] The material deposition at some non-normal angle on the surface produces the desired structures. In the case described here, however, the lateral deposition of metal (on the masking feature) causes an effect on the desired structure (on the substrate). The masking particles and the laterally growing material are stripped from the substrate, leaving patterned particles on the substrate. This case bears strong similarity to the deposition of field emission tips using the Spindt process,[126] in which a cone-shaped tip is produced in the bottom of a well structure due to lateral deposition of material on the edge of the well. The laterally grown, masking material is subsequently stripped and removed.

The amount of deposited material per unit area of the substrate is uniform. For a sphere of radius r, the surface area of one hemisphere of the sphere ($2\pi r^2$) exposed to the evaporative flux is two times greater than the projected area (πr^2) of the same sphere on a flat substrate. Thus, since the same amount of metal is being distributed over a larger area, a thinner film should be expected. Due to increasing curvature, the coating on the hemisphere is not uniform, varying from maximum thickness at the pole positions to (nominally) zero at equator. In addition, the film microstructure is dependent on the incidence flux angle; the microstructure of a thin gold film deposited on the spherical

bead surface changes from a dense continuous film (at the pole) to a porous film with distinct islands (near the equator). In Figure 2-13, 865 nm silica particles coated with 25 nm of gold (using e-beam evaporation) show this gradual transition from dense capping film to porous and grainy structure.

When depositing a given material on an inclined substrate, the thickness of the deposited material is determined by the angle θ of the surface normal with respect to the vapor flux vector ***F***. In SL, spherical colloids act as masking particles, and the surface normal varies from pole of the particles to equator. Along the spherical surface, θ = 0º, at the pole position ("top" of the masking particles, where the surface tangent plane is parallel to the substrate), and varies to θ = 90° at the equator ("side" of the masking particles, with a tangent plane perpendicular to the substrate) (Figure 2-14). These geometrical relationships are illustrated in Figure 2-14A.

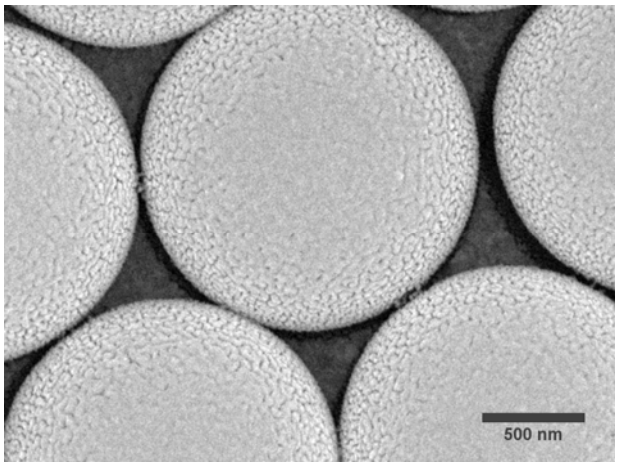

Figure 2-13. FE-SEM image of an array of 865 nm silica particles coated with 25 nm thick of gold using e-beam evaporation. The gold coating gradually evolves from the dense capping structure at the pole positions to the porous, grainy film near the equators.

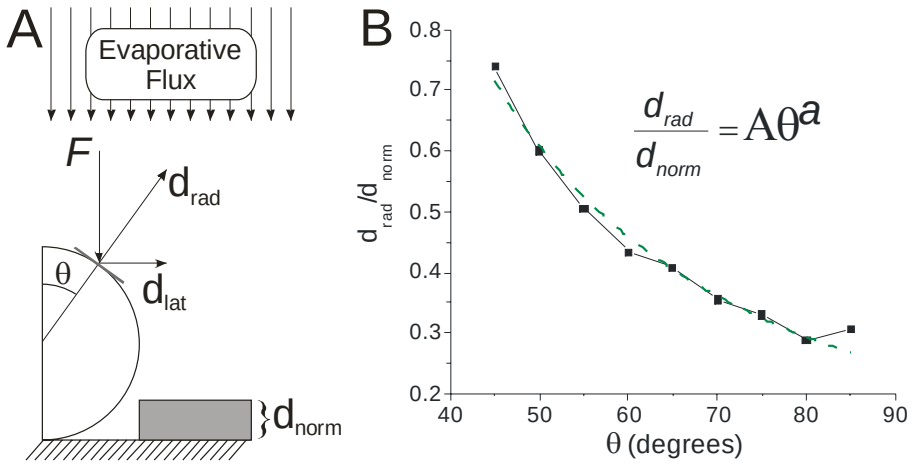

Figure 2-14. (A) Schematic illustration of the geometrical relationship of metal deposition on the sphere surface. (B) Power law fit of the ratio of metal thickness on an inclined flat substrate (as an approximation of d_{rad}) and metal thickness on a substrate oriented normal to the evaporative flux (d_{norm}) as θ is varied from 45º to 85º.

The radial thickness of metal deposited locally on the sphere surface, d_{rad}, depends on θ and the nominal thickness of metal as measured at a deposition monitor or on a flat substrate (d_{norm}, where θ = 0º). Of particular importance in the GSDSL process is the occlusion of the triangular opening between three particles as metal is deposited. The occlusion arises from lateral growth (parallel to the substrate) of the deposited metal film. The lateral growth of the metal film, d_{lat}, depends on the thickness of the metal film on the sphere surface:

$$d_{lat} = d_{rad} \sin \theta \qquad (1)$$

The direct shadowing effect of the laterally growing film on the substrate depends on the curvature of the sphere. If d_{lat} is greater than the projected edge of the sphere, the deposited metal film on the sphere will shadow the substrate, reducing the effective size of the hole. Based on considerations of the geometry of packed particles, the hole will be completely occluded such that no material can pass through it when

$$d_{lat} - (r - r \sin \theta) = 0.154r \qquad (2)$$

where r is the radius of the masking spheres.

Models to describe the thickness of films deposited on inclined surfaces have included power law growth exponents,[127-132] but a full understanding of the growth of thin films on inclined surfaces is still under development. To facilitate understanding of the deposition of gold on the spherical surface (which is very difficult to measure experimentally), a series of flat inclined surfaces was prepared, with the inclination angle θ ranging from 45º to 85º, and the resulting thickness of the deposited metal on each surface was analyzed by SEM. The ratio between the thickness of the deposited metal on the inclined surfaces and a normal surface is plotted as a function of θ in Figure 2-13B. The system was fit by a power law

$$\frac{d_{rad}}{d_{norm}} = A\theta^{a} \qquad (3)$$

with R^2 = 0.9796 shown as dashed line in Figure 2-14B, where A (=256.8) is a scaling factor and the growth exponent *a* = -1.55. With the empirical data of metal deposition on inclined surfaces, the prediction of metal thickness threshold for complete occlusion of the masking hole can be made as particle size is varied.

When the evaporation of a thin film of metal on a layer of close packed spheres is considered, the amount of shadowing of the substrate is dependent on the thickness of metal deposited and the radius of the masking spheres. This factor is included in the model through the use of χ, the ratio of the thickness of metal deposited as measured on a normal flat substrate (d_{norm}) and the radius of the masking spheres (r). Combining Eqs. 1-3 and substituting the ratio χ, the following model for the occlusion of the substrate by the growing metal film can be considered:

$$\chi = \frac{2/\sqrt{3} - \sin\theta}{A\theta^{-1.55}\sin\theta} \qquad (4)$$

Occlusion occurs, and the hole is completely filled, when the lateral growth of the film from three adjacent close-packed spheres reaches the center of the hole, a condition met when the shadowing distance is equivalent to 0.154r. θ_{occ} (the angle at which the perpendicular growth to the curved surface causes occlusion) can be determined from the

derivative of Eq. 4; χ_{occ} (the corresponding value of χ) determined at this angle corresponds to the metal thickness that must be deposited to close the central hole. χ_{occ} was determined to be 0.6, at $\theta_{occ} = 81°$, independent of template size. It is difficult to verify the exact θ angle experimentally; due to the glancing angle deposition effect, however, it is can be observed (as in Figure 2-15) that the columnar structures near the equator have more shadowing effect than those at the equator. Furthermore, $\chi_{occ} = 0.6$ successfully predicts the occlusion for 865 nm masking particles, *vide infra*.

The lateral growth of material on the highly inclined near-equator region of the masking sphere results in columnar growth structures similar to those observed in glancing angle deposition. The columnar structures generally grow towards the center of the triangular hole between adjacent particles, casting a shadow of themselves on the substrate below. The edges of material which has been deposited on the substrate fall into the shadow and are effectively masked from the metal vapor. As material builds up close to the equatorial regions of the beads, this leads to a shrinkage in the size of the masking hole, as shown in Figure 2-15, and a reduction in the surface area of the deposited metal, forming a truncated pseudo-tetrahedral structure, and eventually, a pseudo-tetrahedron (Figure 2-16).

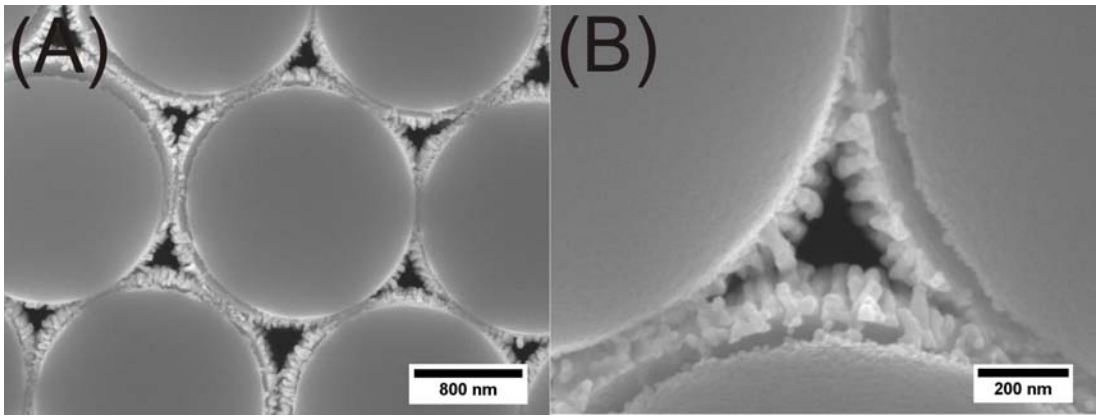

Figure 2-15. FE-SEM images of inverted gold coated silica beads (865 nm), showing the partially occluded holes between adjacent particles. The final holes (dark triangular regions shown in both A and magnified in B) are significantly reduced from the initial size due to the deposition of material on the equatorial region of the particles.

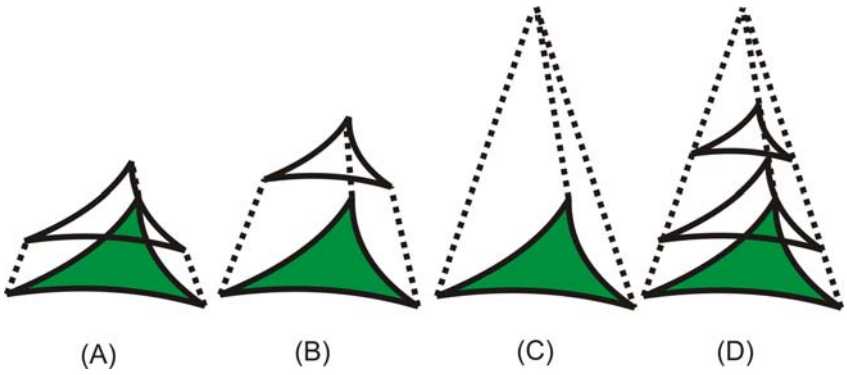

Figure 2-16. Schematic illustration of truncated tetrahedral structures and pseudo-tetrahedrons, exaggerated in the vertical dimension. A triangle grows into a short truncated tetrahedron (A), then a tall truncated tetrahedron (B), and finally a pseudo-tetrahedron (C). The overall transition in the geometry is shown in (D).

The initial vapor deposition creates an array of planar triangular nanostructures. The dynamic shadowing effect during metal deposition results in geometrically structured particles which evolve from two-dimensional planar structures to three-dimensional truncated tetrahedral prisms, which grow to become tetrahedrons (with some slight structural variations, *vide infra*). The out-of-plane height of all of these structures closely matches the overall deposited film thickness. As the planar features grow in the vertical direction, the triangular face on the top surface of a short truncated tetrahedron will shrink as the height of the structure grows. A pseudo-tetrahedral structure is expected to eventually form when the interstitial hole becomes completely blocked by the evaporative materials. Geometrical considerations indicate that the interstitial holes will be fully occluded when the film thickness near equatorial positions reaches 15.4% of the radius of the sphere. When this occurs, a continuous metallic coating will be formed on the top surface of the array of close-packed spheres. After reaching this point, the height of the pseudo-tetrahedron remains constant regardless of additional deposition of material.

Results and discussion

Field emission SEM (FE-SEM) technique offers a two dimensional visualization of the materials at a resolution of a few nanometers. The size and shape of the features

can be directly obtained from the SEM images, including the overall deposited film thickness, and the size and the height of the tetrahedral structures. As shown in Figure 2B, for instance, the projected area of initially formed triangular structures (the bottom face of ultimate tetrahedra), as well as the interparticle spacing, can be estimated given a large area of close-packed silica spheres. Cross-sectional imaging enables us to measure the out-of-plane height of the truncated tetrahedral structures and the overall deposited film thickness as well (Figure 2-17), by fracturing the silicon substrate and tilting the surface normal to 90º relative to the electron beam. As shown in Figure 2-17A, silica spheres with 865 nm radius were deposited with ~100 nm of gold. The bright regions on the silica spheres are the gold coating, showing the grain of the deposited metal. Visible on the substrate are the truncated pseudo-tetrahedrons, whose heights are at the length scale of ca. 100 nm. In Figure 2-17B, silica spheres with 143 nm radius were deposited with ~100 nm of gold. The island structures visible on the silicon substrate are pseudo-tetrahedrons. The variation of their height and shape is mainly due to grain effects. Also notable, the continuous metal film on the 143 nm silica beads was detached from many of them by the shock of substrate breakage. In addition, atomic force microscopy (AFM) provides morphological information on the metal coating and the pseudo-tetrahedral structures. The entire 3D AFM picture provides useful geometrical details of the resulting truncated tetrahedral structures, including the shape, size, height and the surface roughness as well.

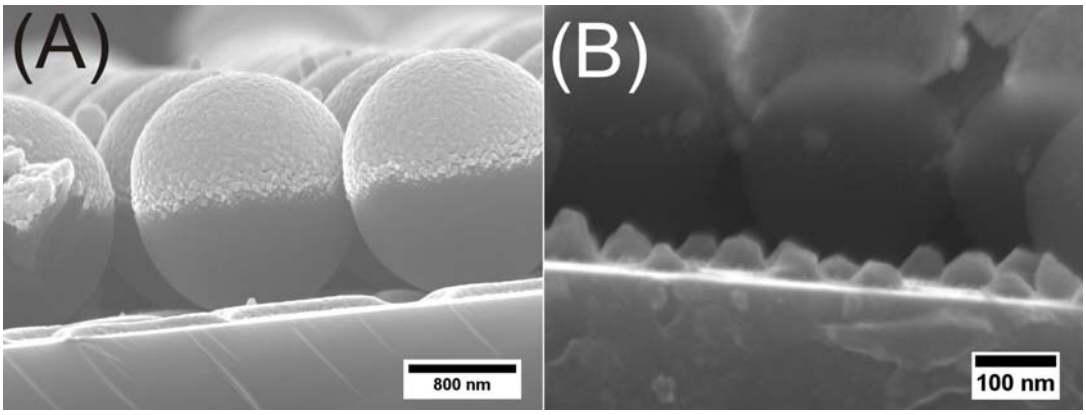

Figure 2-17. Side-view FE-SEM images of the silica colloidal spheres half-coated with gold on the silicon substrate. The silicon substrate was fractured through the feature regions.

By varying the overall deposited film thickness, the three-dimensional truncated tetrahedral structures of various heights were generated. Figure 2-18 depicts SEM and AFM images of the resulting representative truncated tetrahedral structures with four different heights. The AFM images of those three-dimensional structures are also accordingly shown side by side for comparison. As clearly seen in Figure 2-18, for structures generated from 865 nm masking particles, the structure evolves from nearly a two-dimensional planar triangle to a short truncated tetrahedron, and then, a tall truncated tetrahedron, and eventually, a pseudo-tetrahedron. In the case of truncated tetrahedron (Figure 2-18F, G), a plateau area can be clearly observed on the top of the structures, representing the top face of the truncated tetrahedrons. The grain structure of the deposited gold is apparent on the top face, as well as on the sidewall. Structure roughness appears to be due primarily to the grain size of the evaporative material. In addition, the edges of the structures are surrounded with nanoscale particulate features. The formation of these structures occurs through spontaneous diffusion processes of the adsorbed metal vapor on the substrate surface. Adatom diffusion terminates in one of several ways, including clustering, re-evaporation, or capture at defects.[133] These processes are governed by the physical properties of the evaporative materials and the substrate, and the interfacial energetics between the two materials. Surface diffusion can be also affected by the presence of impurities and environmental media.[133] In the case of the 865 nm radius masking particles, the grain size and the diffusion length are small compared to the size of the tetrahedral structures, and therefore have a role of lesser significance on the overall shape. Notably, however, most of the observed pseudo-tetrahedrons have blunt tips when the film thickness reaches the point of occlusion, due to the effect of grain size.

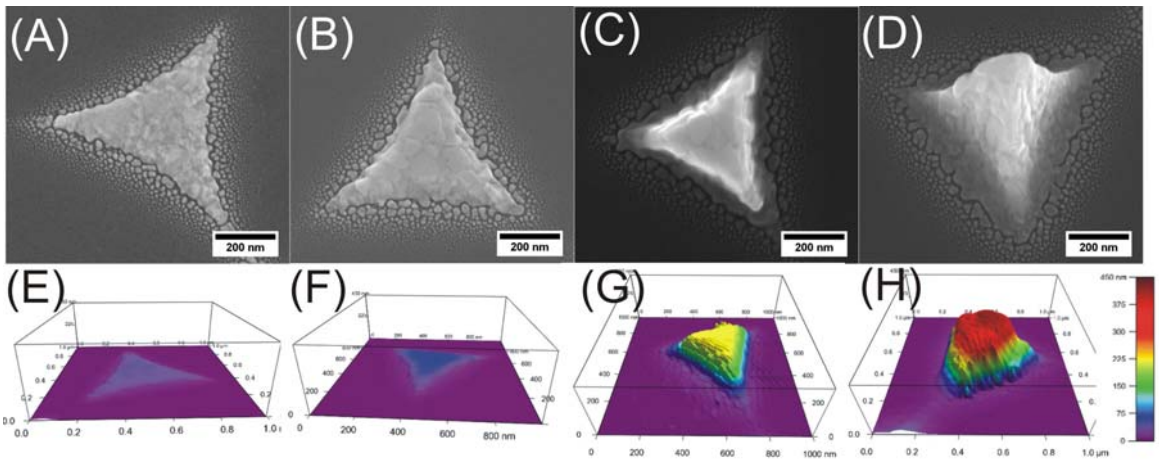

Figure 2-18. FE-SEM (A-D) and AFM images (E-H) of the truncated tetrahedrons, produced with the 865 nm masking silica colloidal spheres, at the overall deposited film thickness of (A,E) 40, (B,F) 66, (C,G) 250, and (D,H) 500 nm, respectively.

The grain size of gold has a more significant influence when producing features with sizes on the same scale as the grain structure. Figure 2-19 illustrates the SEM and AFM images of the tetrahedral structures produced from the use of 143 nm silica beads. A structural transition from flat triangular structure to pseudo-tetrahedron can be clearly observed with increasing film thickness. Unlike the case of 865 nm bead, however, these structures deviate significantly from regular truncated tetrahedrons, appearing much more rounded in AFM images. In high resolution FE-SEM imaging, each individual structure appears to be a crystalline gold particle (including facets in many cases), composed of one or more single crystals. The lack of uniform geometry in the structure implies that the GSDSL technique approaches a resolution limit with regard to structure size when the desired feature size is comparable to the grain size and diffusion length of the employed evaporative material. To fully understand this behavior will require further work with other materials, including finely-grained metals.

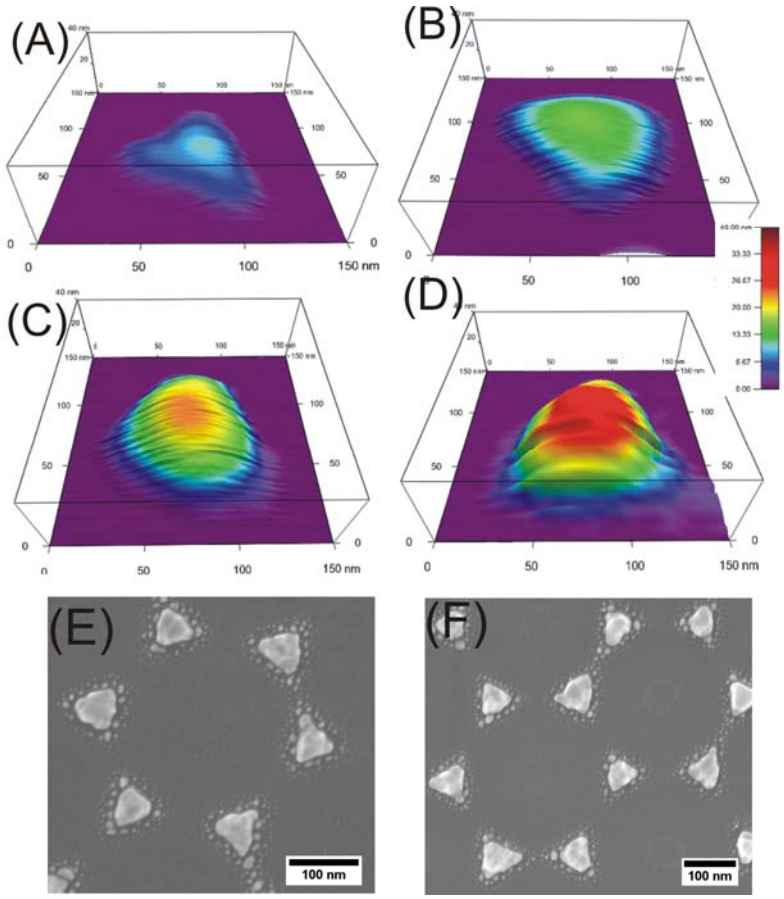

Figure 2-19. AFM (A-D) and FE-SEM images (E-F) of the truncated tetrahedrons, masked with 143 nm silica colloidal spheres, at the overall deposited film thickness of (A) 5, (B) 10, (C,E) 30, and (D,F) 40 nm, respectively.

The out-of-plane height of the structured features (h), as well as the overall deposited film thickness (d_{norm}), was determined using AFM for a range of metal thicknesses on both r = 865 nm silica spheres and on r = 143 nm silica spheres. As the cantilever scanned along the pathway from the substrate to the top face of the tetrahedral structure, and then, again, to the substrate (shown as red trace OO' in Figure 2-20A), a height profile of the resulting tetrahedral structure can be obtained. As shown in Figure 2-20B, for larger features templated by larger particles, the out-of-plane height increases with the overall deposited film thickness. The plateau observed in Figure 2-20B for 40, 66 and 250 nm is indicative of the flat top on the truncated tetrahedron while the relatively sharp head of 500nm indicates that the structured feature forms a pseudo-tetrahedron. All the curves appear to be asymmetric with the face of the structure (right

side of the curve) having a greater slope than the intersection of two faces (the left side), which is consistent with the geometry of the tetrahedral structures. In Figure 2-20C, however, which corresponds to the same type of data collected on smaller features templated by smaller particles, no plateau is clearly observed and the curves tend to be symmetric due to the influence of grain structure on the shape, and through the increasing influence of occlusion on the shape of the structure.

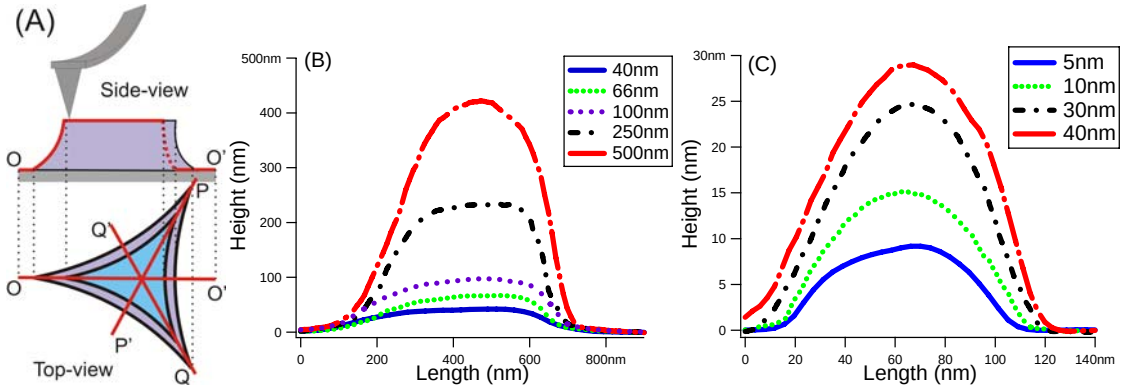

Figure 2-20. (A) Schematic illustration of a typical AFM tip scan; (B,C) height profiles of resulting tetrahedral structure using 865 nm (B) and 143 nm (C) masking silica beads. Each curve is an average of three scanning profiles (OO', PP', QQ') from at least three different tetrahedral structures.

The ratio of h to d_{norm} for both sets of bead templates is plotted in Figure 2-21A. With 865 nm silica beads as masking templates, the ratio of h to d_{norm} is approximately one and drops to 0.89 ± 0.02 when d_{norm} increases to ~490 nm (see curve in Figure 2-21A). This indicates that the average out-of-plane height of the tetrahedral structures matches well with the overall deposited film thickness before occlusion. From Figure 2-21A, χ_{occ} ~0.57, consistent with the above numerical model. In contrast, when 143 nm silica beads are used as masks (see curve in Figure 2-21A), the ratio of h to d_{norm} is less than one and decreases rapidly with increasing deposited film thickness. This behavior can be considered in terms of the interstitial hole size, that is, the triangular hole between three close-packed templating beads. With 865 nm beads, the interstitial hole may be described by an inscribed circle with a radius of 133 nm. This hole is much greater than the grain size of gold, and metal vapor can freely reach the masked substrate with little likelihood of deposition on the masking particles, until the hole has been partially/mostly

blocked by lateral growth of metal. With close-packed 143 nm beads, an inscribed circle in the interstitial hole has a radius of only 22 nm. This size is comparable to the smallest grain domain of gold deposited on the silica beads through e-beam evaporation. Metal vapor has a low flux through the narrowing interstitial opening, and has an increased probability of capture at the bead surface, rather than reaching the substrate and depositing in a shadowed configuration. The continuous flux of material leads to a continuous increase in the height of the structure over the deposition but at a decreased rate. The ratio drops more significantly when the interstitial holes approach occlusion.

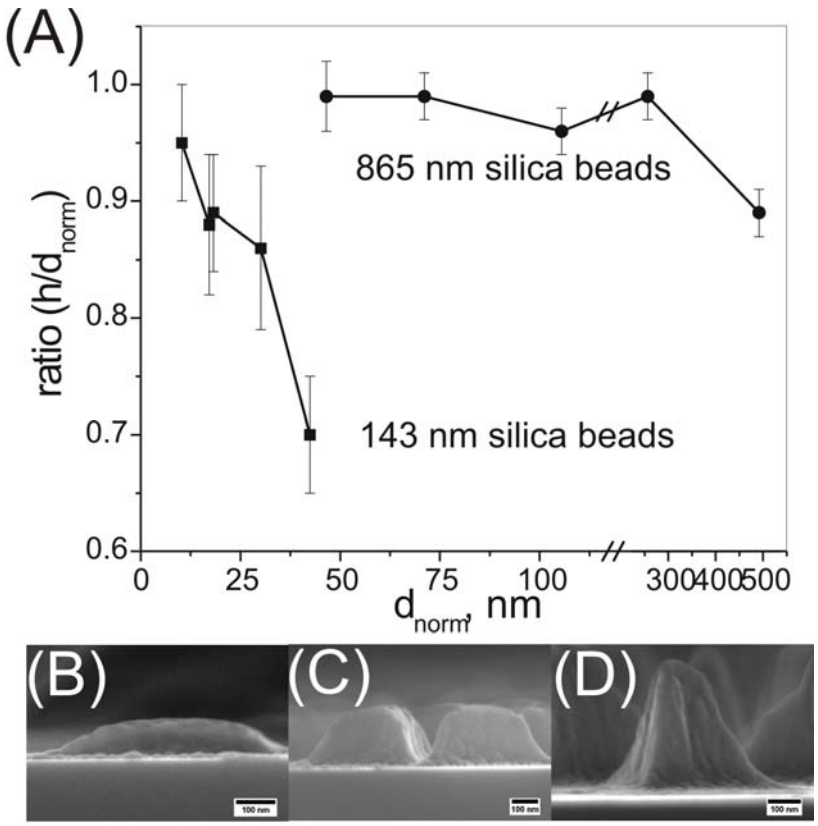

Figure 2-21. (A) Ratio of out-of-plane height (h, nm) to the overall deposited film thickness (d_{norm}, nm) in case of 865 nm and 143 nm silica beads. The h and d_{norm} were determined via height profiling in AFM (see Figure 2-20). Side-view FE-SEM images of (truncated) tetrahedral structures with deposited film thickness of (A) 100, (B) 250, and (C) 500 nm in case of 865 nm beads.

In summary, 3D nanostructures with controllable structure can be formed into high fidelity patterns by geometrically structured dynamic shadowing lithography. The shape and the morphology of the resulting structures were characterized by FE-SEM and AFM. In addition, the growth of structures have been thoroughly investigated to determine a structural growth model, including the overall deposited film thickness and the height of the three-dimensional truncated tetrahedral structures. Based on the predictive empirical model, the height and shape of the 3D metal dot arrays can be carefully controlled through deposition rate from the e-beam evaporation system. Gold structures showed significant variability of fine structural features, primarily due to the formation of large grains, an effect that was especially evident in fabrication of features with dimensions comparable to the grain size. Structure and morphology are anticipated to be strongly affected with other materials and substrates, including those with lower surface diffusion or smaller grain size. By understanding the nature of the evaporative materials, multilayered or other advanced hierarchical nanostructures can be easily attained through GSDSL. This empirical model also verified the minimal thickness of coating around the equatorial region, providing a valid explanation for the presence of the silica belt.

The combination of FE-SEM and AFM enables us to clearly visualize the geometrical transition in three dimensions. We believe that huge benefits can be garnered by knowledge of the detailed geometry of the deposited material with respect to the studied parameters. For instance, as the size and shape of the metal nanostructures changes, the localized surface plasmon resonance would change accordingly. This would allow further information on the physical and chemical properties of the SL substrates to be elucidated.

These structures also present an interesting substrate to perform studies of heterogeneous catalysts dependent on the interface of two metals.[134,135] The understanding of structures produced here would allow extremely uniform bimetallic materials with precisely controlled contact areas to be created. The effect of the metals' contact could then be easily studied in order to better understand these systems and optimize them for further use.

References

(1) Casagrande, C.; Fabre, P.; Raphael, E.; Veyssie, M. *Europhys. Lett.* **1989,** *9*, 251-255.

(2) Walther, A.; Muller, A. H. E. *Soft Matter* **2008,** *4*, 663-668.

(3) Ozin, G. A.; Manners, I.; Fournier-Bidoz, S.; Arsenault, A. *Adv. Mater.* **2005,** *17*, 3011-3018.

(4) Sundararajan, S.; Lammert, P. E.; Zudans, A. W.; Crespi, V. H.; Sen, A. *Nano Lett.* **2008,** *8*, 1271-1276.

(5) Wang, J. *ACS Nano* **2009,** *3*, 4-9.

(6) Nisisako, T.; Torii, T.; Takahashi, T.; Takizawa, Y. *Adv. Mater.* **2006,** *18*, 1152-1156.

(7) Anker, J. N.; Behrend, C. J.; Huang, H.; Kopelman, R. *J. Magn. Magn. Mater.* **2005,** *293*, 655-662.

(8) Walther, A.; Drechsler, M.; Rosenfeldt, S.; Harnau, L.; Ballauff, M.; Abetz, V.; Muller, A. H. E. *J. Am. Chem. Soc.* **2009,** *131*, 4720-4728.

(9) Smoukov, S. K.; Gangwal, S.; Marquez, M.; Velev, O. D. *Soft Matter* **2009,** *5*, 1285-1292.

(10) Gangwal, S.; Cayre, O. J.; Velev, O. D. *Langmuir* **2008,** *24*, 13312-13320.

(11) Glotzer, S. C.; Solomon, M. J. *Nat. Mater.* **2007,** *6*, 557-562.

(12) Hong, L.; Cacciuto, A.; Luijten, E.; Granick, S. *Nano Lett.* **2006,** *6*, 2510-2514.

(13) Zhang, Z.; Glotzer, S. C. *Nano Lett.* **2004,** *4*, 1407-1413.

(14) Paxton, W. F.; Kistler, K. C.; Olmeda, C. C.; Sen, A.; St. Angelo, S. K.; Cao, Y.; Mallouk, T. E.; Lammert, P. E.; Crespi, V. H. *J. Am. Chem. Soc.* **2004,** *126*, 13424-13431.

(15) Fournier-Bidoz, S.; Arsenault, A. C.; Manners, I.; Ozin, G. A. *Chem. Comm.* **2005**, 441-443.

(16) Jonathan, R. H.; Richard, A. L. J.; Anthony, J. R.; Tim, G.; Reza, V.; Ramin, G. *Phy. Rev. Lett.* **2007,** *99*, 048102.

(17) Perro, A.; Reculusa, S.; Ravaine, S.; Bourgeat-Lami, E.; Duguet, E. *J. Mater. Chem.* **2005,** *15*, 3745-3760.

(18) Jiang, S.; Schultz, M. J.; Chen, Q.; Moore, J. S.; Granick, S. *Langmuir* **2008,** *24*, 10073-10077.

(19) Ho, C. C.; Chen, W. S.; Shie, T. Y.; Lin, J. N.; Kuo, C. *Langmuir* **2008,** *24*, 5663-5666.

(20) Ahmad, H.; Saito, N.; Kagawa, Y.; Okubo, M. *Langmuir* **2008,** *24*, 688-691.

(21) Walther, A.; Andre, X.; Drechsler, M.; Abetz, V.; Muller, A. H. E. *J. Am. Chem. Soc.* **2007,** *129*, 6187-6198.

(22) Dendukuri, D.; Hatton, T. A.; Doyle, P. S. *Langmuir* **2007,** *23*, 4669-4674.

(23) Nie, L.; Liu, S.; Shen, W.; Chen, D.; Jiang, M. *Angew. Chem., Int. Ed.* **2007,** *119*, 6437-6440.

(24) Dendukuri, D. P.; Daniel, C.; Collins, J.; Hatton, T. A.; Doyle, P. S. *Nat. Mater.* **2006,** *5*, 365-369.

(25) Nie, Z.; Li, W.; Seo, M.; Xu, S.; Kumacheva, E. *J. Am. Chem. Soc.* **2006,** *128*, 9408-9412.

(26) Suzuki, D.; Kawaguchi, H. *Colloid Polym. Sci.* **2006,** *284*, 1471-1476.

(27) Roh, K. H.; Martin, D. C.; Lahann, J. *Nat. Mater.* **2005,** *4*, 759-763.

(28) Takei, H.; Shimizu, N. *Langmuir* **1997,** *13*, 1865-1868.

(29) Fujimoto, K.; Nakahama, K.; Shidara, M.; Kawaguchi, H. *Langmuir* **1999,** *15*, 4630-4635.

(30) Erhardt, R.; Boker, A.; Zettl, H.; Kaya, H.; Pyckhout-Hintzen, W.; Krausch, G.; Abetz, V.; Muller, A. H. E. *Macromolecules* **2001,** *34*, 1069-1075.

(31) Cayre, O.; Paunov, V. N.; Velev, O. D. *Chem. Comm.* **2003**, 2296-2297.

(32) Cayre, O.; Paunov, V. N.; Velev, O. D. *J. Mater. Chem.* **2003,** *13*, 2445-2450.

(33) Erhardt, R.; Zhang, M.; Boker, A.; Zettl, H.; Abetz, C.; Frederik, P.; Krausch, G.; Abetz, V.; Muller, A. H. E. *J. Am. Chem. Soc.* **2003,** *125*, 3260-3267.

(34) Lu, Y.; Xiong, H.; Jiang, X.; Xia, Y.; Prentiss, M.; Whitesides, G. M. *J. Am. Chem. Soc.* **2003,** *125*, 12724-12725.

(35) Paunov, V. N.; Cayre, O. J. *Adv. Mater.* **2004,** *16*, 788-791.

(36) Du, Y. Z.; Tomohiro, T.; Zhang, G.; Nakamura, K.; Kodaka, M. *Chem. Comm.* **2004**, 616-617.

(37) Perro, A.; Reculusa, S.; Pereira, F.; Delville, M. H.; Mingotaud, C.; Duguet, E.; Bourgeat-Lami, E.; Ravaine, S. *Chem. Comm.* **2005**, 5542-5543.

(38) Gu, H.; Yang, Z.; Gao, J.; Chang, C. K.; Xu, B. *J. Am. Chem. Soc.* **2005,** *127*, 34-35.

(39) Takahara, Y. K.; Ikeda, S.; Ishino, S.; Tachi, K.; Ikeue, K.; Sakata, T.; Hasegawa, T.; Mori, H.; Matsumura, M.; Ohtani, B. *J. Am. Chem. Soc.* **2005,** *127*, 6271-6275.

(40) Pawar, A. B.; Kretzschmar, I. *Langmuir* **2009**, *25*, 9057-9063.

(41) Lahiri, B.; Dylewicz, R.; De La Rue, R. M. ; Johnson, N. P. *Opt. Express* **2010**, *18*, 11202-11208.

(42) Cui, Z. Nanofabrications: Principles, Capability, and Limits; Springer: New York, 2008.

(43) Tseng, A. A. (ed.) Nanofabrication: Fundamentals and Applications; World Scientific: Singapore, 2008.

(44) Ito, T.; Okazaki, S. *Nature* **2000**, 406, 1027-1031.

(45) Peercy, P. S. *Nature* **2000**, 406, 1023-1026.

(46) Mack, C. Fundamental Principles of Optical Lithography: The Science of Microfabrication; Wiley: England, 2008.

(47) Okazaki, S. *J. Vac. Sci. Technol. B* **1991**, 9, 2829-2833.

(48) Timothy, A. B. *J. Vac. Sci. Technol. B* **2003**, 21, 2632-2637.

(49) Gwyn, C. W.; Stulen, R.; Sweeney, D.; Attwood, D. *J. Vac. Sci. Technol. B* **1998**, 16, 3142-3149.

(50) Stulen, R. H.; Sweeney, D. W. *IEEE J. Quantum Elect.* **1999**, 35, 694-699.

(51) Silverman, J. P. *J. Vac. Sci. Technol. B* **1997**, 15, 2117-2124.

(52) Heuberger, A. *J. Vac. Sci. Technol. B* **1988**, 6, 107-121.

(53) Silverman, J. P. *J. Vac. Sci. Technol. B* **1998**, 16, 3137-3141.

(54) Wallraff, G. M.; Hinsberg, W. D. *Chem. Rev.* **1999**, 99, 1801-1822.

(55) Mendes, P. M.; Jacke, S.; Critchley, K.; Plaza, J.; Chen, Y.; Nikitin, K.; Palmer, R. E.; Preece, J. A.; Evans, S. D.; Fitzmaurice, D. *Langmuir* **2004**, 20, 3766-3768.

(56) Donthu, S.; Pan, Z.; Myers, B.; Shekhawat, G.; Wu, N.; Dravid, V. *Nano Lett.* **2005**, 5, 1710-1715.

(57) Chou, S. Y.; Krauss, P. R.; Renstrom, P. J. *J. Vac. Sci. Technol. B* **1996**, 14, 4129-4133.

(58) Guo, L. J. *Adv. Mater.* **2007**, 19, 495-513.

(59) Zankovych, S.; Hoffmann, T.; Seekamp, J.; Bruch, J.-U.; Torres, C. M. S. *Nanotechnology* **2001**, 12, 91-95.

(60) Sun, S.; Chong, K. S. L.; Leggett, G. J. *J. Am. Chem. Soc.* **2002**, 124, 2414-2415.

(61) Alkaisi, M. M.; Blaikie, R. J.; McNab, S. J.; Cheung, R.; Cumming, D. R. S. *Appl. Phys. Lett.* **1999**, 75, 3560-3563.

(62) Aizenberg, J.; Rogers, J. A.; Paul, K. E.; Whitesides, G. M. *Appl. Optics* **1998**, 37, 2145-2152.

(63) Solak, H. H.; David, C.; Gobrecht, J.; Golovkina, V.; Cerrina, F.; Kim, S. O.; Nealey, P. F. *Microelectron. Eng.* **2003**, 67-68, 56-62.

(64) Lu, C.; Lipson, R. H. *Laser Photonics Rev.* **2010**, 4, 568-580.

(65) Stroscio, J. A.; Eigler, D. M. *Science* **1991**, 254, 1319-1326.

(66) Ross, C. B.; Sun, L.; Crooks, R. M. *Langmuir* **1993**, 9, 632-636.

(67) Liu, G.-Y.; Xu, S.; Qian, Y. *Acc. Chem. Res.* **2000**, 33, 457-466.

(68) Piner, R. D.; Zhu, J.; Xu, F.; Hong, S.; Mirkin, C. A. *Science* **1999**, 283, 661-663.

(69) Haynes, C. L.; Van Duyne, R. P. *J. Phys. Chem. B* **2001**, 105, 5599-5611.

(70) Hulteen, J. C.; Van Duyne, R. P. *J. Vac. Sci. Technol. A* **1995**, 13, 1553-1558.

(71) Jensen, T. R.; Malinsky, M. D.; Haynes, C. L.; Van Duyne, R. P. *J. Phys. Chem. B* **2000**, 104, 10549-10556.

(72) Kosiorek, A.; Kandulski, W.; Chudzinski, P.; Kempa, K.; Giersig, M. *Nano Lett.* **2004**, 4, 1359-1363.

(73) Tan, B. J. Y.; Sow, C. H.; Koh, T. S.; Chin, K. C.; Wee, A. T. S.; Ong, C. K. *J. Phys. Chem. B* **2005**, 109, 11100-11109.

(74) Chan, G. H.; Zhao, J.; Hicks, E. M.; Schatz, G. C.; Van Duyne, R. P. *Nano Lett.* **2007**, 7, 1947-1952.

(75) Cheng, S. L.; Wong, S. L.; Lu, S. W.; Chen, H. *Ultramicroscopy* **2008**, 108, 1200-1204.

(76) Weekes, S. M.; Ogrin, F. Y.; Murray, W. A. *Langmuir* **2004**, 20, 11208-11212.

(77) Lipson, A. L.; Comstock, D. J.; Hersam, M. C. *Small* **2009**, 5, 2807-2811.

(78) Cheng, S. L.; Lu, S. W.; Li, C. H.; Chang, Y. C.; Huang, C. K.; Chen, H. *Thin Solid Films* **2006**, 494, 307-310.

(79) Kosiorek, A.; Kandulski, W.; Glaczynska, H.; Giersig, M. *Small* **2005**, 1, 439-444.

(80) Bullen, H. A.; Garrett, S. J. *Nano Lett.* **2002**, 2, 739-745.

(81) Kei, C.-C.; Kuo, K.-H.; Su, C.-Y.; Lee, C.-T.; Hsiao, C.-N.; Perng, T.-P. *Chem. Mater.* **2006**, 18, 4544-4546.

(82) Coutts, M. J.; Zareie, H. M.; Cortie, M. B.; Phillips, M. R.; Wuhrer, R.; McDonagh, A. M. *ACS Appl. Mater. Interfaces* **2010**, 2, 1774-1779.

(83) Liu, D. F.; Xiang, Y. J.; Wu, X. C.; Zhang, Z. X.; Liu, L. F.; Song, L.; Zhao, X. W.; Luo, S. D.; Ma, W. J.; Shen, J.; Zhou, W. Y.; Wang, G.; Wang, C. Y.; Xie, S. S. *Nano Lett.* **2006**, 6, 2375-2378.

(84) Chen, L.-Y.; Huang, Y.-Y.; Chang, C.-H.; Sun, Y.-H.; Cheng, Y.-W.; Ke, M.-Y.; Chen, C.-P.; Huang, J. *Opt. Express* **2010**, 18, 7664-7669.

(85) Fuhrmann, B.; Leipner, H. S.; Hoche, H.-R.; Schubert, L.; Werner, P.; Gosele, U. *Nano Lett.* **2005**, 5, 2524-2527.

(86) Sarkar, D. K.; Farzaneh, M. *Appl. Surf. Sci.* **2008**, 254, 3758-3761.

(87) Duval Malinsky, M.; Kelly, K. L.; Schatz, G. C.; Van Duyne, R. P. *J. Phys. Chem. B* **2001**, 105, 2343-2350.

(88) Jensen, T. R.; Duval, M. L.; Kelly, K. L.; Lazarides, A. A.; Schatz, G. C.; Van Duyne, R. P. *J. Phys. Chem. B* **1999**, 103, 9846-9853.

(89) Malinsky, M. D.; Kelly, K. L.; Schatz, G. C.; Van Duyne, R. P. *J. Am. Chem. Soc.* **2001**, 123, 1471-1482.

(90) Haynes, C. L.; McFarland, A. D.; Smith, M. T.; Hulteen, J. C.; Van Duyne, R. P. *J. Phys. Chem. B* **2002**, 106, 1898-1902.

(91) Gwinner, M. C.; Koroknay, E.; Fu, L.; Patoka, P.; Kandulski, W.; Giersig, M.; Giessen, H. *Small* **2009**, 5, 400-406.

(92) Li, C.; Hong, G.; Qi, L. *Chem. Mater.* **2009**, 22, 476-481.

(93) Heo, C.-J.; Kim, S.-H.; Jang, S. G.; Lee, S. Y.; Yang, S.-M. *Adv. Mater.* **2009**, 21, 1726-1731.

(94) Hajiaboli, A. R.; Cui, B.; Kahrizi, M.; Truong, V.-V. *Phys. Status Solidi A* **2009**, 206, 976-979.

(95) Whitney, A. V.; Myers, B. D.; Van Duyne, R. P. *Nano Lett.* **2004**, 4, 1507-1511.

(96) Cheung, C. L.; Nikolic, R. J.; Reinhardt, C. E.; Wang, T. F. *Nanotechnology* **2006**, 17, 1339-1343.

(97) Zheng, Y. B.; Huang, T. J. *Journal of the Association for Laboratory Automation* **2008**, 13, 215-226.

(98) Hicks, E. M.; Zhang, X.; Zou, S.; Lyandres, O.; Spears, K. G.; Schatz, G. C.; Van Duyne, R. P. *J. Phys. Chem. B* **2005**, 109, 22351-22358.

(99) Sherry, L. J.; Jin, R.; Mirkin, C. A.; Schatz, G. C.; Van Duyne, R. P. *Nano Lett.* **2006**, 6, 2060-2065.

(100) Jensen, T. R.; Schatz, G. C.; Van Duyne, R. P. *J. Phys. Chem. B* **1999**, 103, 2394-2401.

(101) Haes, A. J.; Zhao, J.; Zou, S.; Own, C. S.; Marks, L. D.; Schatz, G. C.; Van Duyne, R. P. *J. Phys. Chem. B* **2005**, 109, 11158-11162.

(102) Ormonde, A. D.; Hicks, E. C. M.; Castillo, J.; Van Duyne, R. P. *Langmuir* **2004**, 20, 6927-6931.

(103) Hicks, E. M.; Lyandres, O.; Hall, W. P.; Zou, S.; Glucksberg, M. R.; Van Duyne, R. P. *J. Phys. Chem. C* **2007**, 111, 4116-4124.

(104) Willets, K. A.; Van Duyne, R. P. *Annu. Rev. Phys. Chem.* **2007**, 58, 267-297.

(105) Haynes, C. L.; Van Duyne, R. P. *J. Phys. Chem. B* **2003**, 107, 7426-7433.

(106) McFarland, A. D.; Young, M. A.; Dieringer, J. A.; Van Duyne, R. P. *J. Phys. Chem. B* **2005**, 109, 11279-11285.

(107) Haes, A. J.; Hall, W. P.; Chang, L.; Klein, W. L.; Van Duyne, R. P. *Nano Lett.* **2004**, 4, 1029-1034.

(108) Haes, A. J.; Van Duyne, R. P. *Anal. Bioanal. Chem.* **2004**, 379, 920-930.

(109) Haes, A. J.; Haynes, C. L.; McFarland, A. D.; Schatz, G. C.; Van Duyne, R. P.; Zou, S. *MRS Bull.* **2005**, 30, 368-375.

(110) Haes, A. J.; Zou, S.; Schatz, G. C.; Van Duyne, R. P. *J. Phys. Chem. B* **2004**, 108, 109-116.

(111) Haes, A. J.; Chang, L.; Klein, W. L.; Van Duyne, R. P. *J. Am. Chem. Soc.* **2005**, 127, 2264-2271.

(112) Riboh, J. C.; Haes, A. J.; McFarland, A. D.; Ranjit Yonzon, C.; Van Duyne, R. P. *J. Phys. Chem. B* **2003**, 107, 1772-1780.

(113) Haes, A. J.; Zou, S.; Schatz, G. C.; Van Duyne, R. P. *J. Phys. Chem. B* **2004**, 108, 6961-6968.

(114) Haes, A. J.; Van Duyne, R. P. *J. Am. Chem. Soc.* **2002**, 124, 10596-10604.

(115) McFarland, A. D.; Van Duyne, R. P. *Nano Lett.* **2003**, 3, 1057-1062.

(116) Hall, W. P.; Modica, J.; Anker, J.; Lin, Y.; Mrksich, M.; Van Duyne, R. P. *Nano Lett.* **2011**, 11, 1098-1105.

(117) Yi, D. K.; Kim, D.-Y. *Chem. Comm.* **2003**, 39, 982-983.

(118) Cai, Y.; Ocko, B. M. *Langmuir* **2005**, 21, 9274-9279.

(119) Kempa, K.; Kimball, B.; Rybczynski, J.; Huang, Z. P.; Wu, P. F.; Steeves, D.; Sennett, M.; Giersig, M.; Rao, D. V. G. L. N.; Carnahan, D. L.; Wang, D. Z.; Lao, J. Y.; Li, W. Z.; Ren, Z. F. *Nano Lett.* **2003**, 3, 13-18.

(120) Ryu, K.; Badmaev, A.; Gomez, L.; Ishikawa, F.; Lei, B.; Zhou, C. *J. Am. Chem. Soc.* **2007**, 129, 10104-10105.

(121) Zhou, S.; Mcllwrath, K.; Jackson, G.; Eichhorn, B. *J. Am. Chem. Soc.* **2006**, 128, 1780-1781.

(122) Ohring, M. Materials Science of Thin Films: Deposition and Structure (2 ed.); Academic Press: London, 2001.

(123) Matthew, M. H.; Michael, J. B. *J. Vac. Sci. Technol. A* **2007**, 25, 1317-1335.

(124) Robbie, K.; Sit, J. C.; Brett, M. J. *J. Vac. Sci. Technol. B* **1998**, 16, 1115-1122.

(125) Robbie, K.; Brett, M. J. *J. Vac. Sci. Technol. A* **1997**, 15, 1460-1465.

(126) Spindt, C. A.; Holland, C. E.; Brodie, I.; Mooney, J. B.; Westerberg, E. R. *IEEE T. Electron Dev.* **1989**, 36, 225-228.

(127) Dolatshahi-Pirouz, A.; Hovgaard, M. B.; Rechendorff, K.; Chevallier, J.; Foss, M.; Besenbacher, F. *Phys. Rev. B* **2008**, 77, 115427.

(128) Dolatshahi-Pirouz, A.; Sutherland, D. S.; Foss, M.; Besenbacher, F. *Appl. Surf. Sci.* **2011**, 257, 2226-2230.

(129) Karabacak, T.; Wang, G. C.; Lu, T. M. *J. Vac. Sci. Technol. A* **2004**, 22, 1778-1784.

(130) Meakin, P. *Phys. Rev. A* **1988**, 38, 994.

(131) Tang, F.; Karabacak, T.; Li, L.; Pelliccione, M.; Wang, G. C.; Lu, T. M. *J. Vac. Sci. Technol. A* **2007**, 25, 160-166.

(132) Tang, F.; Liu, D. L.; Ye, D. X.; Zhao, Y. P.; Lu, T. M.; Wang, G. C.; Vijayaraghavan, A. *J. Appl. Phys.* **2003**, 93, 4194-4200.

(133) Venables, J. A.; Spiller, G. D. T.; Hanbucken, M. *Rep. Prog. Phys.* **1984**, 47, 399-459.

(134) Wang, X.; Li, N.; Pfefferle, L. D.; Haller, G. L. *Catal. Today* **2009**, 146, 160-164.

(135) Dellamorte, J. C.; Lauterbach, J.; Barteau, M. A. *Appl. Catal. A* **2011**, 391, 281-288.

Chapter 3

Chemical Transformation of Bimetallic Janus Particles and Ultrathin Metal Films

3.1 Background

The incorporation of multiple functionalities in a single particle opens exciting areas of study in materials science, and allows for the production of versatile, efficient and highly specific building blocks in device development. Janus particles (JPs), a specific class of anisotropic particles,[1-6] are undergoing rapid development in such applications as microfluidic transport and cargo delivery,[7,8] self-assembly,[3,9-11] photonics,[12] imaging and sensing,[13,14] electronic papers,[15] and Pickering emulsion.[16]

In Chapter 2, our laboratory has successfully demonstrated the fabrication of bimetallic Janus particles (BJPs) through electron beam evaporation.[17] The Janus particles are composed of micron or sub-micron silica particles with metals deposited on opposite hemispheres. The general applicability of physical vapor deposition for solid materials allows the fabrication of multifunctional Janus particles with various properties, but is most commonly available to metals. Heterogeneous chemical reactions provide a facile route to modify the composition of the metals, changing not only electronic properties but also morphological structure.

In section 3.3, two approaches, post-fabrication transformation and intermediate transformation, were demonstrated to transform bimetallic Janus particles (BJPs) into multifunctional particles with various combinations of metals, metal oxides and metal sulfides through solid-gas heterogeneous reactions. The heterogeneous chemical reactions, including native oxidation under atmospheric conditions, induced oxidation in an air plasma, and sulfidation reaction with hydrogen sulfide in a heterogeneous reaction, are used to transform the metals into other species. Characterization by SEM, XPS, EDS, and XRD clearly demonstrates that the chemical transformation of the parent metal/metal BJPs ($M_1//M_2$, where M_1 is deposited first and M_2 is deposited through a second evaporation, "//" represents the equatorial silica belt) produces a wide array of previously unavailable Janus particle types, such as metal-oxide (M//MO), metal-sulfide (M//MS), oxide-oxide (MO//MO), sulfide-sulfide (MS//MS), and oxide-sulfide (MO//MS). Incorporation of two metals, semiconductors or dielectrics into one single unit is a novel development in the fabrication of anisotropic objects on submicron scale, and is expected

to bring additional versatility in electronic, magnetic, and optical devices constructed from these building blocks.

However, it is difficult to fully characterize the compositional change over the curved structures by SEM, XPS and XRD, especially in those cases where partial oxidation or sulfidation is occurred, resulting in formation of stratified structures. In contrast, metal coatings on flat substrates are relatively easy to characterize. Techniques such as XPS depth profiling and X-ray reflectivity are better characterization methods for stratified structures on the flat substrate. In order to further understand the chemical transformation reactions occurring on the bimetallic Janus particles, the metal coatings with same thickness deposited on flat substrates were studied under the same oxidation and sulfidation reaction condition.

In section 3.4, oxidation and sulfidation of aluminum, titanium, cobalt, nickel and silver thin films are investigated. The metal films were prepared by e-beam evaporation onto a flat silicon substrate. The oxidation reactions were carried out first in atmosphere, and then facilitated by air plasma. The sulfidation reactions were conducted in a solid-gas heterogeneous fashion. The X-ray photoelectron spectroscopy (XPS) and depth analysis clearly revealed varying degrees of oxidation and sulfidation for each metal, as well as the depth dependent change in valence state. Metallic thin films such as aluminum and titanium were both extremely susceptible to air, showing no sign of deeper oxidation or sulfidation afterwards. Only an ultrathin layer of native oxide was formed on the top of nickel and silver; air plasma enhanced the oxidation of nickel, whereas the morphology of silver changed along with the valence state. Similarly, both nickel and silver were quantitatively transformed into metal sulfides. Cobalt thin film spontaneously formed a thin layer of oxide after air exposure. The thickness of this oxide layer slightly increased with plasma exposure time. H_2S only reacted with the cobalt oxide at the surface, forming a sulfide layer on top, a layer of the oxide in the middle, sitting on the bulk cobalt film; however, an ultrathin layer of cobalt oxide was formed reversibly at the surface of the sulfide upon exposure to air. The preference of either oxidation or sulfidation can be explained using the thermodynamic data.

3.2 Experimental

3.2.1 Fabrication of transformed BJPs

Chemical transformation of the bimetallic Janus particles (BJPs) was carried out following the approaches illustrated in Figure 3-1. The post-fabrication transformation undergoes a pathway of metal evaporation - inversion - metal evaporation - chemical transformation, which includes (A) the first metal evaporation onto a self-assembled monolayer of silica colloidal particles, (B) inversion of the metal half-coated silica particles onto another substrate, (C) the second metal evaporation, and (D) chemical transformation of BJPs. The intermediate transformation undergoes a pathway of metal evaporation (E) - chemical transformation (F) - inversion (G) - metal evaporation (H) - chemical transformation (I), in which the initial chemical transformation is performed between the first metal evaporation (E) and inversion (G). The colloidal silica particles were purchased from the Bangs Laboratories, Inc. Metal evaporation was carried out in a Temescal BJD-2000 e-beam evaporator at ~10^{-5} torr. The plasma reactions were performed in a radio frequency air-oxygen plasma cleaner (Harrick PDC-3XG, 100 W) for, typically, 30 minutes. The sulfidation reactions were carried out in a vessel with hydrogen sulfide gas flow (Matheson Tri-Gas, 99.5%) for 24 hours.

3.2.2 Oxidation of ultrathin metal films

A thin layer of metal was deposited onto a flat Si (100) substrate through electron-beam evaporation of the metal (Temescal BJD-2000) at ~10^{-5} Torr. The metals deposited were aluminum, titanium, cobalt, nickel and silver with a typical thickness of 20 nm, which ensured to form a continuous thin layer on the substrate. Native oxidation is supposed to occur at the surface for all metals upon exposure to atmosphere. The plasma reactions were performed in a radio frequency air-oxygen plasma cleaner (Harrick PDC-3XG, 100 W) for, typically, 30 minutes. The sulfidation reactions were carried out in a vessel with hydrogen sulfide gas flow (Matheson Tri-Gas, 99.5%) in and out through the duration of the reactions, 24 hours in our case.

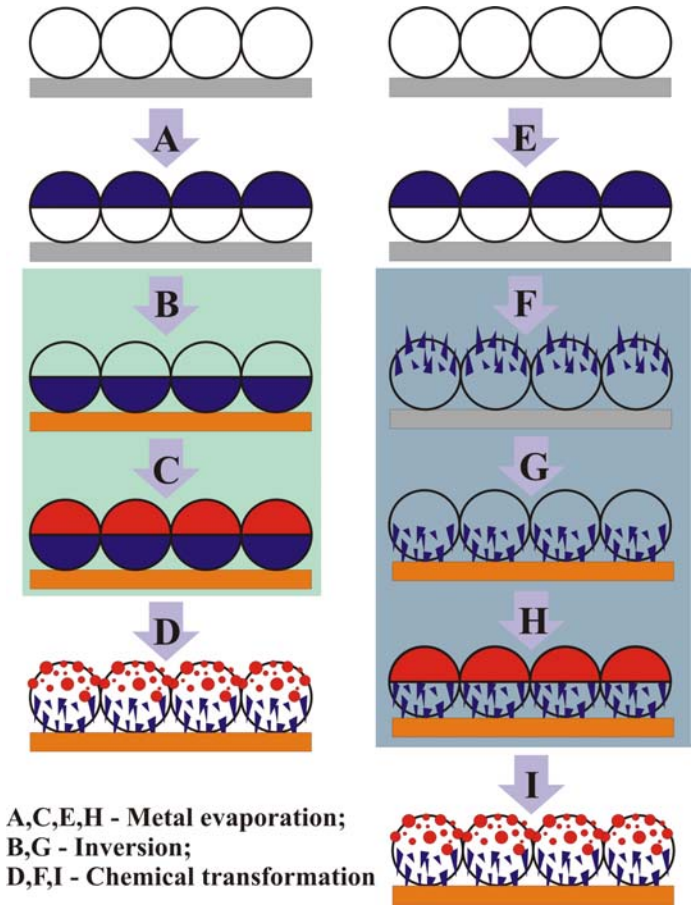

Figure 3-1. Post-fabrication transformation (pathway: metal evaporation (A) - inversion (B) - metal evaporation (C) - chemical transformation (D)) and intermediate transformation (pathway: metal evaporation (E) - chemical transformation (F) - inversion (G) - metal evaporation (H) - chemical transformation (I))

3.2.3 Characterization

XPS (Phi 5000 Versaprobe, monochromated Al Kα source) was applied to determine the valence state of metals, as well as the presence of oxygen and sulfur. Depth profiling was accomplished using controlled erosion of the surface by an argon ion sputter-etching at 2 kV. Binding energies of XPS spectra were corrected by referencing the C 1s signal of adventitious hydrocarbon to 284.8 eV. The etching time, coupled with the peak information of the desired elements, was recorded at a fixed etch power of the ion gun to determine the depth of each phase. XRD (Rigaku, Cu target, 50 kV, 160 mA) was used to determine the crystal structure of the metal caps and metallic thin films

before and after oxidation and sulfidation. Low angle x-ray reflectivity was also carried out to determine the phase composition and thickness of each layer for the sulfidized cobalt thin film. FE-SEM (JEOL 7600F) is used to record the morphological changes, and EDS is utilized to determine the elemental composition. The thickness of each film was monitored by a crystal detector during evaporation. Indeed, the actual thickness was calibrated using a surface profiler (KLA Tencor Alpha-Step IQ®).

3.3 Selective chemical transformation of bimetallic Janus particles

The chemical transformation of BJPs was carried out through solid-gas heterogeneous reactions. The resulting transformed BJPs were characterized by field emission – scanning electron microscopy (FE-SEM), x-ray energy dispersive spectroscopy (EDS), x-ray diffraction (XRD), and x-ray photoelectron spectroscopy (XPS).

Two motifs of BJP transformation were explored – post-fabrication transformation and intermediate transformation. In post-fabrication transformation, the heterogeneous chemical reactions were performed after the BJPs were obtained through two subsequent metal evaporations. In intermediate transformation, the initial chemical conversion was carried out after the first metal evaporation, followed by the second metal evaporation and, if necessary, a second chemical transformation (Figure 3-1). The first method was most efficient when only one type of chemical transformation was required. For instance, the MO//MO Janus particles were formed by exposure of a bimetallic particle to an air plasma. M//MO or M//MS Janus particles were prepared when one of the metals such as gold and platinum was inert in the reaction conditions. Post-fabrication transformation allows preparation of Janus particles such as Au//Ag_2O, Au//Ag_2S, Ag_2S//NiS, and Ag_2O//NiO with relative ease and minimal time. However, this method possesses the intrinsic disadvantage that multiple simultaneous transformations may be difficult to predict. This drawback can be compensated by using intermediate transformation. The metal on a metal-silica Janus particle is converted to a metal oxide or metal sulfide. The particles were inverted, and a second metal was deposited. If necessary, a second chemical transformation was carried out on the newly deposited

metal, subject to the limitations described below. Two chemical transformation steps one after another enabled the selective conversion of each metal hemisphere to oxides, sulfides and other species.

Of paramount importance is the thermodynamic stability of the first transformation product to the second transformation reaction conditions. Thermodynamically, the first product must be stable against further transformation since the first hemisphere is not protected from the subsequent reaction. Through intermediate transformation, Janus particles impossible through post-fabrication transformation were produced without the use of protection or de-protection, such as Ag_2S//Ag, Ag_2O//Ag and Al_2O_3//NiS.

Atmospheric oxidation occurs to some metals once exposed to atmospheric conditions. This spontaneous process was observed on some BJPs, which made it difficult to prepare some types of pure bimetallic JPs (M//M) unless the metals on both hemispheres were inert to air. For those BJPs composed of air-reactive metals such as aluminum and titanium, depending on the thickness of the deposited metals, M//MO and MO//MO types of JPs could be prepared by exposure to air. XPS analysis revealed some pure metal underlying these oxide films.

As shown in Figure 3-2A, trace I in black represents the initial scan of the sample without ion sputtering/etching, in which the aluminum shows two oxidation states, Al(III) at 73.6 eV and Al(0) at 70.4 eV. Trace II in red was collected after etching for 3 seconds. Both aluminum peaks had slight shifts towards higher binding energies, 74.3 eV and 71.0 eV, respectively. Trace III in blue was collected after etching for 45 seconds in total, in which the peak for Al(III) remained and the peak for Al(0) disappeared. The disappearance of the metallic aluminum peak indicates the protected aluminum has been etched away upon etching. In Figure 3-2B, the O 1s peaks at corresponding etching period remained at ~531.0 eV.

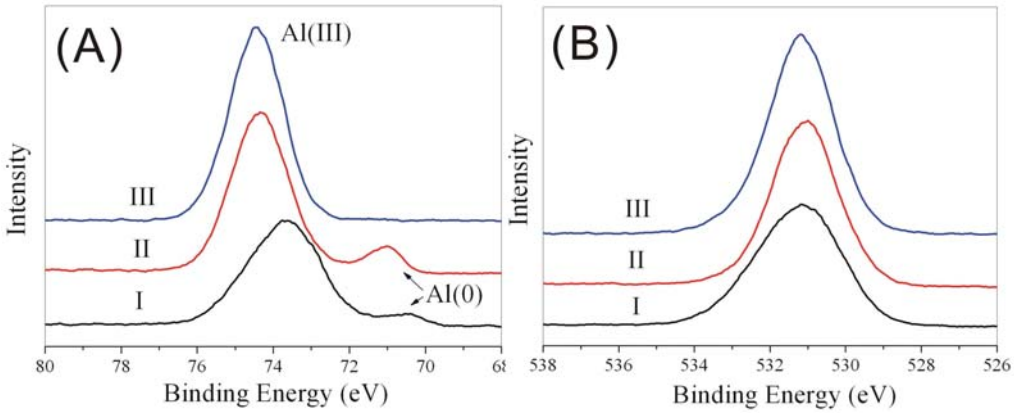

Figure 3-2. XPS depth profile spectra of 4 μm silica beads layers coated with 20 nm of aluminum after exposure to air for 48 hours. (A) Al 2p and (B) O 1s.

Initially, as shown in Figure 3-3A, the pair of titanium peaks at 464.0 eV for Ti $2p_{1/2}$ and 458.4 eV for Ti $2p_{3/2}$ corresponded to the formation of titanium(IV) dioxide layer after exposure to air (trace I). After etching for 3 seconds, both peaks shifted slightly towards lower binding energy, 463.8 eV and 458.2 eV, respectively (trace II). This red shift was also accompanied with a broadening of the Ti $2p_{1/2}$ peak and an appearance of a shoulder peak at approximately 456.8 eV. The emerging pair of the peaks indicated a decreased oxidation state of titanium, that is, titanium(III) oxide, Ti_2O_3. The argon ion bombardment preferentially removed the oxygen from the surface, leading to a non-stoichiometric local surface. The intensities for both Ti(IV) and Ti(III) peaks faded after 30 seconds of etching, and two new peaks, locating at 460.3 eV and 454.6 eV, respectively, appeared to dominate. The continuous shift to the lower binding energy indicated a even lower oxidation state of titanium, titanium(II) oxide, TiO, whose crystal structure was also verified by XRD. Similarly, in Figure 3-3B, the position of the O 1s peaks remained unshifted.

Other BJPs, composed of metals like cobalt, nickel and silver, formed a layer of native oxides with thickness less than 2 nm, protecting the underlying metals from further oxidation.[18] Figure 3-4 illustrates morphological change of cobalt, nickel, and silver half-coated silica beads after exposure to air. The corresponding XPS depth profiles are shown in Figure 3-5.

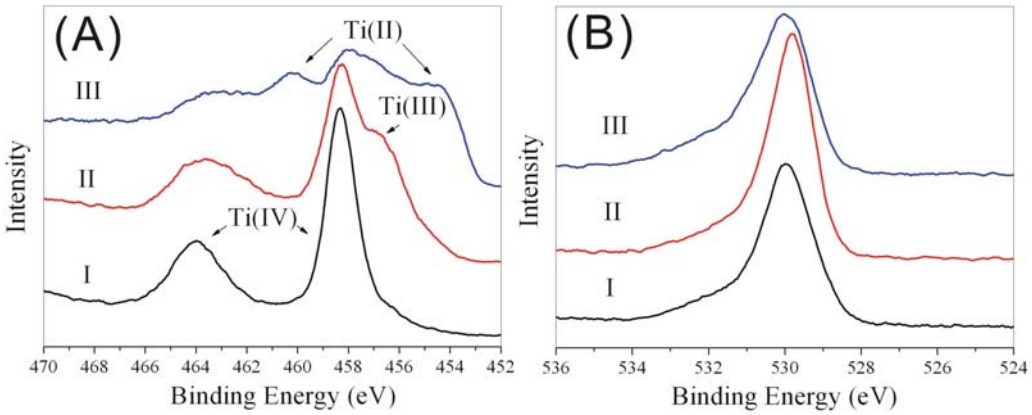

Figure 3-3. XPS depth profile spectra of 4 μm silica beads layers coated with 20 nm of titanium after exposure to air for 48 hours. (A) Ti 2p and (B) O 1s.

In Figure 3-5A, the presence of two major broad peaks centering at 795.7 eV and 779.5 eV indicates Co(II) (trace I); a layer of cobalt(II) oxide was suggested to form upon atmospheric exposure. After etching for 3 seconds, a pair of new peaks, centered at 792.2 eV and 777.3 eV, appeared, corresponding to $2p_{1/2}$ and $2p_{3/2}$ of Co(0) (trace II). The intensity of the Co(0) peaks increased with etching time while the pair of Co(II) peaks disappeared after etching for 6 seconds (trace III) and 12 seconds (trace IV).

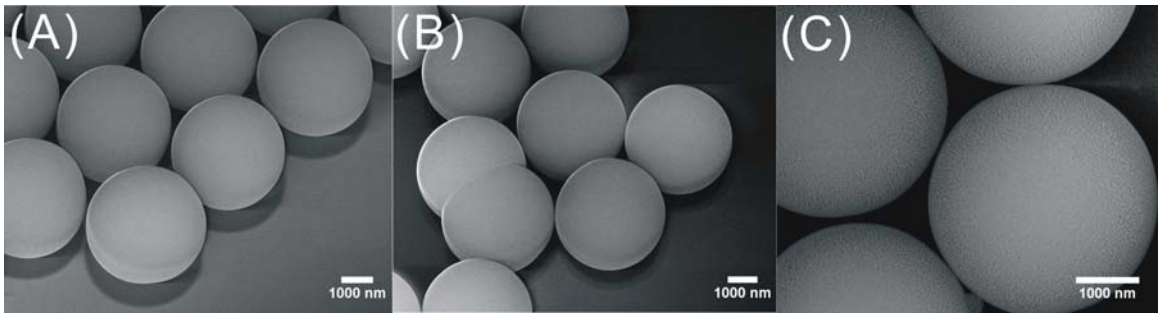

Figure 3-4. FE-SEM images of 4 μm silica beads coated with 20 nm of cobalt (A), nickel (B), and silver (C) after exposure to air for 48 hours.

In Figure 3-5B, two pairs of peaks assigned for Ni(II) and Ni(0) are shown in trace I. However, the peaks for Ni(II), 872.3 eV (Ni $2p_{1/2}$) and 855.2 eV (Ni $2p_{3/2}$), faded significantly after etching for 3 seconds (trace II) and 6 seconds (trace III), accompany with an increase in the Ni(0) peaks located at 869.0 eV and 851.7 eV (traces II and III).

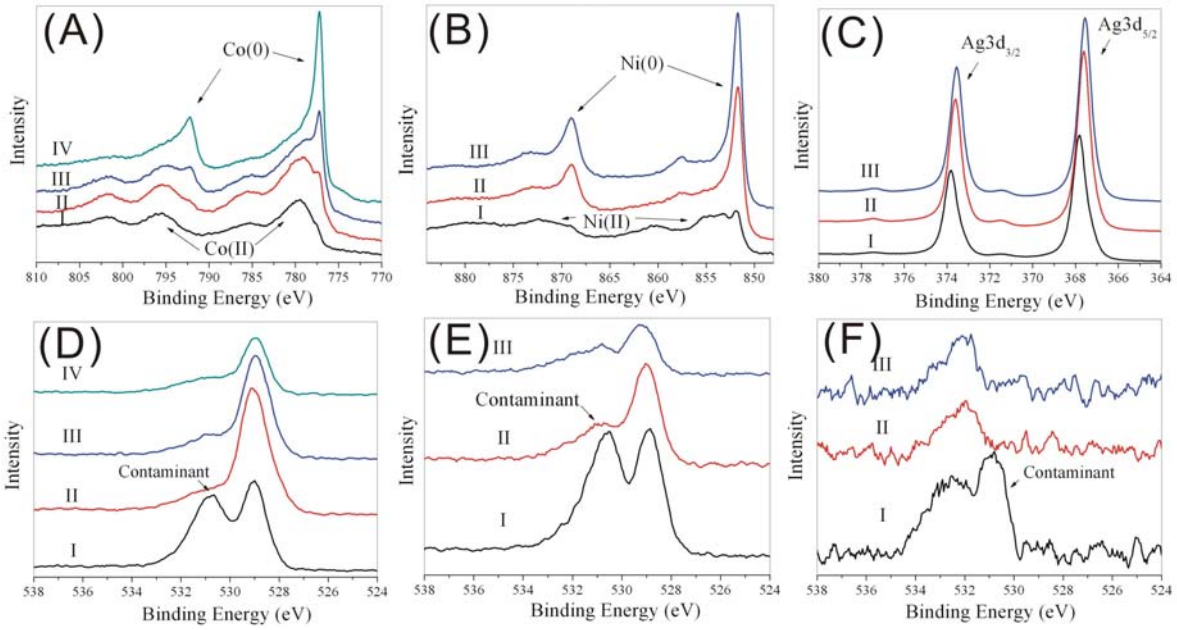

Figure 3-5. XPS depth profile spectra of 4 μm silica beads coated with 20 nm of cobalt (A: Co 2p; D: O 1s), nickel (B: Ni 2p, E: O 1s) and silver (C: Ag 3d, F: O 1s) after exposure to air for 48 hours.

In Figure 3-5C, only a slight shift of Ag (0) from 373.6 eV and 367.6 eV to 373.8 eV and 367.8 eV, respectively, was observed before (trace I) and after etching (II: 3 seconds; III: 6 seconds).The almost immediate disappearance of the metal ion peaks according to the XPS spectra in Figure 3-5A,B,C suggests an ultrathin layer of oxide formed on the surface of the metal coatings.

It can be seen from Figure 3-5D,E,F that the oxygen peaks at ~531.0 eV contributed from the contaminants were removed after etching. The remaining O 1s peaks were partially due to the oxidation of the metal coatings. Ion sputtering/etching led to dramatic decreases in the intensities of the O 1s peaks, which consistently indicates on the surface of the metal coating only forming a thin layer of metal oxide, protecting the underlying metal from further oxidation. In addition, the oxygen signal may be attributed to the silica beads; the non-uniform metal coating did not appear to fully cover the hemisphere (Fig. 3-4C). The small S/N ratio in Figure 3-5F suggested a very low concentration of oxygen in the surface of the material.

Air-oxygen plasma provides a more reactive environment than atmospheric oxidation. For metals with a thin layer of native oxide, the underlying metal coatings were anticipated to undergo further oxidation in the presence of air plasma thus increasing the depth of the oxide film. Air plasma treatment of the naturally oxidized aluminum on BJPs fully converted the protected aluminum to aluminum oxide while the depth of the titanium dioxide layer formed on the surface of the titanium coating increased after exposure to plasma for 30 min. As shown in Figure 3-6, the Al 2p and O 1s peaks are centered at 74.8 eV (A) and 531.9 eV (B), respectively. Compared to the air-exposed Al-JPs, no metallic aluminum peak Al(0) is observed after etching for 0 second (I), 3 seconds (II), and 72 seconds (III). The disappearance of Al(0) peak means the air-oxygen plasma induced a more complete oxidation, converting the remaining "sandwiched" metallic aluminum to oxides. In plasma-oxidized Ti-JPs, the transition of Ti 2p (C) and O 1s peaks (D) is similar to that observed in air-exposed Ti-JPs. The designation of the Ti2p peaks changed from Ti(IV), to Ti(III), and Ti(II) after 0 second (I), 3 seconds (II) and 30 seconds (III) etching. The relative low intensities of the Ti(III) peak in trace II and the Ti(II) peak in trace III suggests a deeper oxidation occurred during plasma oxidation.

Similarly, the air plasma did not fully convert either the cobalt or nickel to their oxides but increased the depth of the oxide films (Figure 3-7). As shown in Figure 3-7A, a transition from Co(II) to Co(0) is observed over the course of the etching time scale. Two peaks centered at 796.8 eV and 781.1 eV in trace I (before etching) and II (after etching for 3 seconds) represent cobalt with an oxidation state of two. The new pair for Co(0) shown as shoulder peaks of Co(II), centered at 793.4 eV and 778.5 eV, become visible in trace III after etching for 48 seconds. This transition happened similarly to the air-exposed Co-JPs after etching for 3 seconds, which strongly suggests a deeper oxidation by oxygen plasma. The sharp peak couple of Co(0) dominated after etching for 78 seconds, accompanying with the disappearance of the Co(II) peaks. In Figure 3-7C, the peaks centered at 873.6 eV and 856.2 eV in trace I are ascribed to Ni $2p_{1/2}$ and Ni $2p_{3/2}$ with an oxidation state of two before etching while the peaks corresponding to Ni(0) are almost invisible. This suggests a relatively thicker layer of oxide formed on the surface of nickel coating. In traces II (3-second etching) and III (6-second etching),

however, the sharpness of the Ni(0) peak couple after short time etching convinced that the oxide layer offered a very good protection for the underlying metal from deeper oxidation. Figures 3-7B and 3-7D depict the change of the oxygen content present in the cobalt and nickel coatings over etching time. Particularly, the previously formed nickel oxide protected the underlying metal such that the thickness of the oxide layer increased only slightly with prolonged plasma exposure time. Metal oxidation begins at the solid-gas interface, producing a thin layer of the metal oxide. The rate of further oxidative processes is mainly determined by the diffusion of the oxygen reactive species through the close-packed lattice structures of the forming metal oxides, and this layer limits the diffusion rate in a highly effective way.[19]

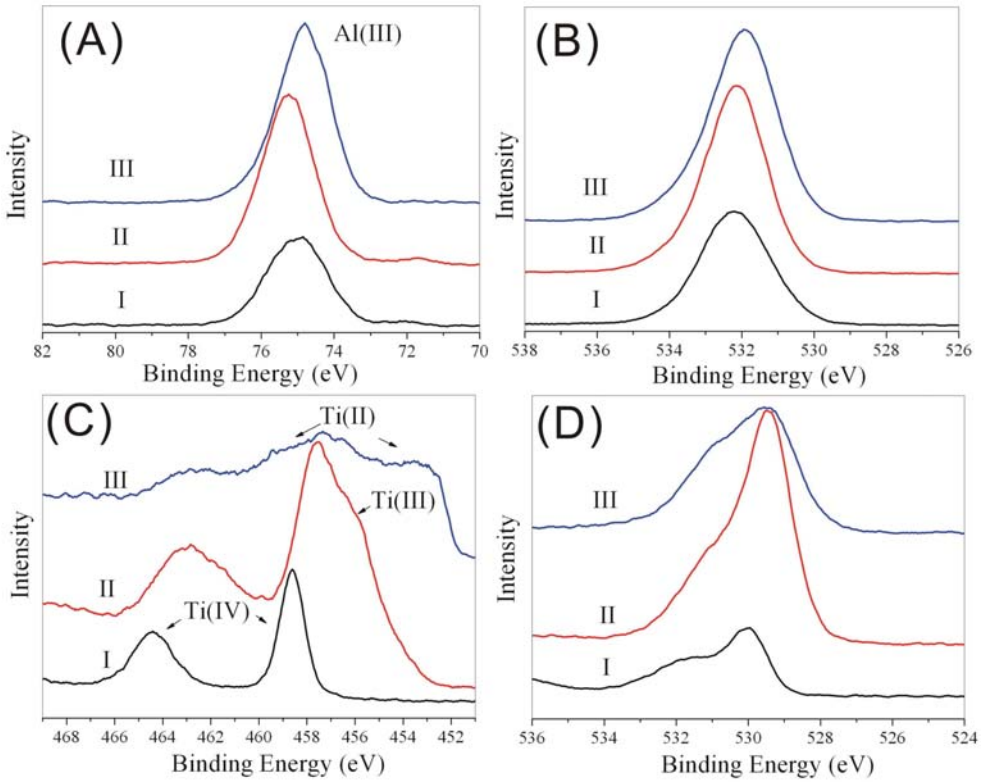

Figure 3-6. XPS depth profile spectra of 4 μm silica beads coated with 20 nm of aluminum and titanium after exposure to air plasma for 30 minutes. Aluminum: (A) Al 2p and (B) O 1s; titanium: (C) Ti 2p and (D) O 1s.

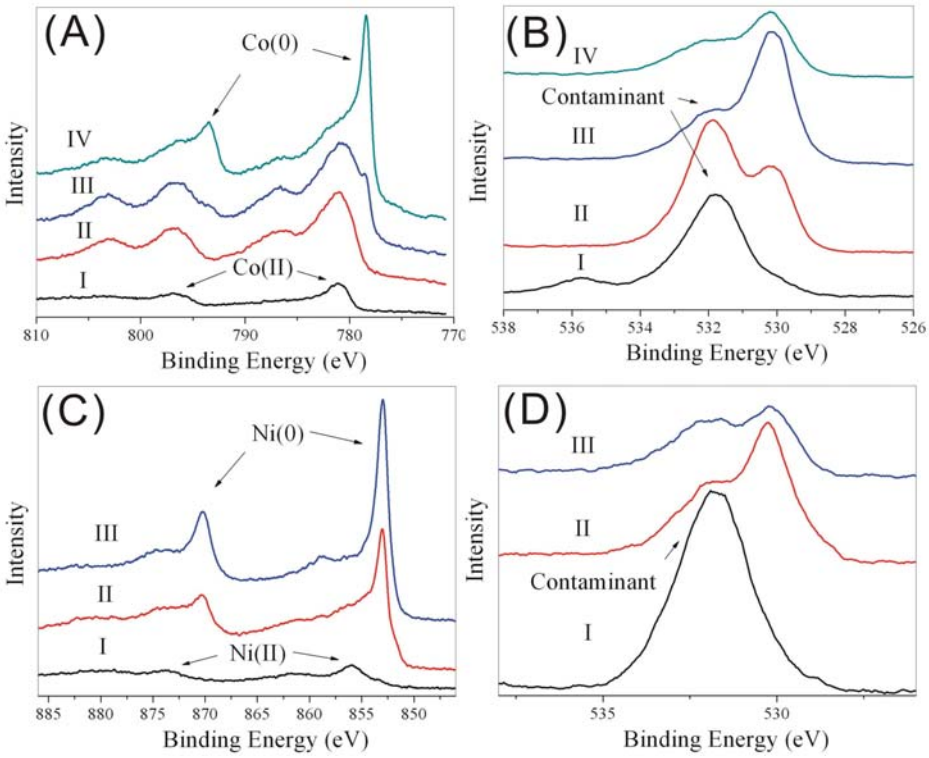

Figure 3-7. XPS depth profile spectra of 4 μm silica beads coated with 20 nm of cobalt and nickel after exposure to air plasma for 30 minutes. Cobalt: (A) Co 2p and (B) O 1s; nickel: (C) Ni 2p and (D) O 1s.

In cobalt and nickel there were no significant morphological changes (Figures 3-8A and 3-8B). However, silver on BJPs showed significant changes in morphology after exposure to air plasma (Figure 3-8C). The silver coating changed from a mostly continuous film to discrete island structures. These islands had lateral dimension of tens to hundreds of nanometers. The observed morphological change was also accompanied by a change in the chemical composition from Ag to Ag_2O (Figure 3-9), as verified by XRD.[18,20] In Figure 3-9A, the Ag $3d_{3/2}$ and Ag $3d_{5/2}$ peaks shifted from 374.1 eV to 373.5 eV and from 368.1 eV to 367.5 eV after etching (I: 0 second; II: 3 seconds; III: 18 seconds; IV: 48 seconds). In Figure 3-9B, compared to the air-exposed Ag-JPs, the intensity of the O 1s peaks appears much stronger even after etching. This is primarily due to the formation of the silver(I) oxide. As seen from the SEM image shown in Fig. 3-8C, the broad oxygen signal is also partially attributed by the silica beads and the oxidized substrate surface.

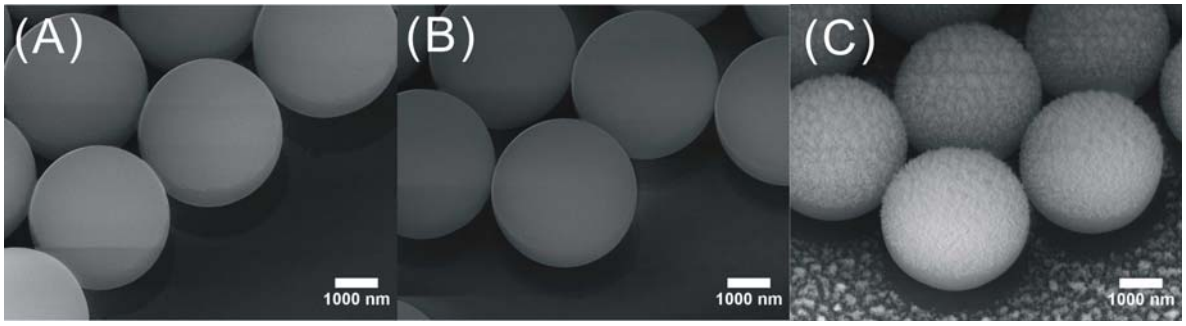

Figure 3-8. FE-SEM images of 4 μm silica beads coated with 20 nm of cobalt (A), nickel (B), and silver (C) after exposure to air plasma for 30 minutes.

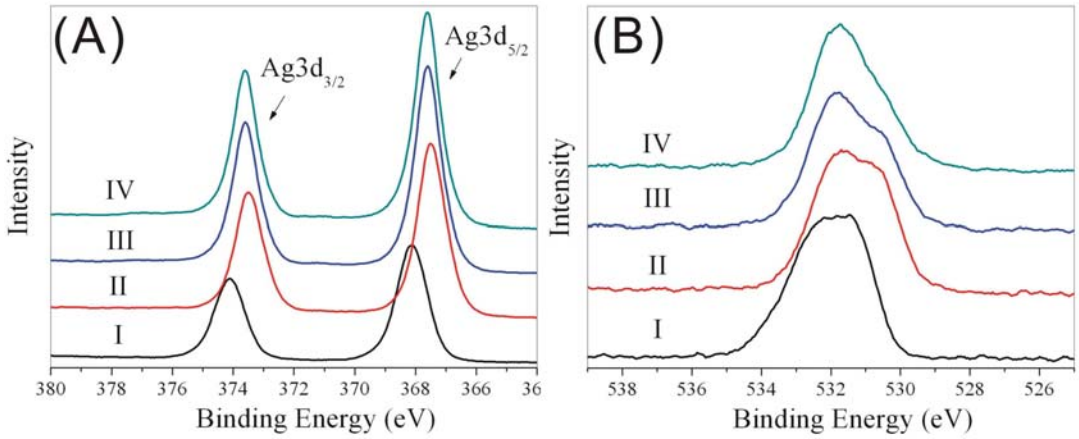

Figure 3-9. XPS depth profile spectra of 4 μm silica beads coated with 20 nm of silver after exposure to air plasma for 30 minutes. (A) Ag 3d and (B) O 1s.

Hydrogen sulfide exposure converted BJPs to their corresponding metal sulfides. The heterogeneous solid-gas sulfidation reaction between metals and hydrogen sulfide at ambient conditions is generally thermodynamically favorable (eq. 1). The thermodynamic stability of many metal sulfides requires that this process must precede deposition of metals that are desired in an unreacted state. Some metal sulfides are less stable than their metal oxides. For example, metals which tend to oxidize in air such as aluminum and titanium possess metal oxides which have lower free energies than that of the sulfides, making it unfavorable to convert them to the sulfides by way of the solid-gas reaction. Sulfide formation did not occur to air oxidized aluminum and titanium films. This was verified by the absence of the sulfur (S2p) peak in the XPS spectra (data not shown). In the case of BJPs containing cobalt, the native cobalt oxide film partially

reacted with hydrogen sulfide, forming a thin layer of cobalt sulfide at the solid-gas interface (Figures 3-10 and 3-11A). As shown in Figure 3-10A, two pairs of Co 2p peaks can be recognized from the traces, centered at 792.5 eV and 777.6 eV for Co(0), and 796.3 eV and 780.1 eV for Co(II), respectively. This suggests the co-existence of metallic and oxidized cobalt in the H_2S-exposed cobalt-containing BJPs. In Figure 3-10B, instead of two well-resolved S $2p_{1/2}$ and S $2p_{3/2}$ peaks, a broad peak was observed in the range of 159 eV and 165 eV, indicating the low concentration of sulfur at surface. The thin layer of the cobalt sulfide layer was also suggested by the decrease in the intensity of the peak after 3 second-etching. In Figure 3-10C, the non-contaminant O 1s peak centered at 529.1 eV increases in intensity after etching, as well as the presence of the S 2p peak, suggesting a possible double-layered structure composed of one layer of cobalt oxide and one layer of cobalt sulfide over the cobalt coating layer.

$$xM\ (s) + H_2S\ (g) \rightarrow M_xS\ (s) + H_2\ (g) \qquad (1)$$

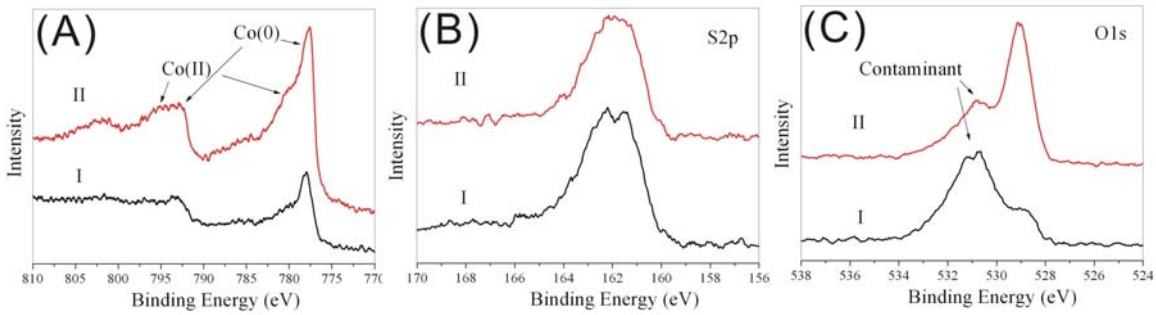

Figure 3-10. XPS depth profile spectra of 4 μm silica beads coated with 20 nm of cobalt after exposure to hydrogen sulfide for 24 hours. (A) Co 2p, (B) S 2p, and (C) O 1s.

Nickel and silver exposed to air formed protective oxides, both of which showed complete conversion to their respective sulfides (Figure 3-12).[21] As shown in Figure 3-12A, the Ni 2p peaks centered at 873.1 eV and 855.1 eV decreased rapidly in intensities while the Ni 2p peaks centered at 869.4 eV and 852.2 eV became dominant after 3 second-etching. This change in intensity for NiO (decrease) and NiS (increase) suggests NiS is the major compositional material, and NiO formed a thin layer on the top, which is verified by the increase in intensities of two resolved S 2p peaks (Figure 3-12B) and rapid decrease of the O 1s peak (Figure 3-12C). In Figure 3-12D, formation of Ag_2S led

to a shift in the binding energies of Ag $3d_{3/2}$ and Ag $3d_{5/2}$ peaks, compared to the metallic silver, from 373.6 eV to 373.8 eV and 367.6 eV to 367.8 eV, respectively. The resolved S $2p_{1/2}$ and S $2p_{3/2}$ peaks shifted to 162.1 eV and 161.0 eV with a slight increase in intensity after 3 second-etching (Figure 3-12E). The intensity of the O 1s peak was originally low and then decreased after etching but not fully disappeared, suggesting a very low concentration of oxygen at surface, possibly due to a contribution from the silica hemispheres covered with non-continuous silver coatings (Figure 3-12F).

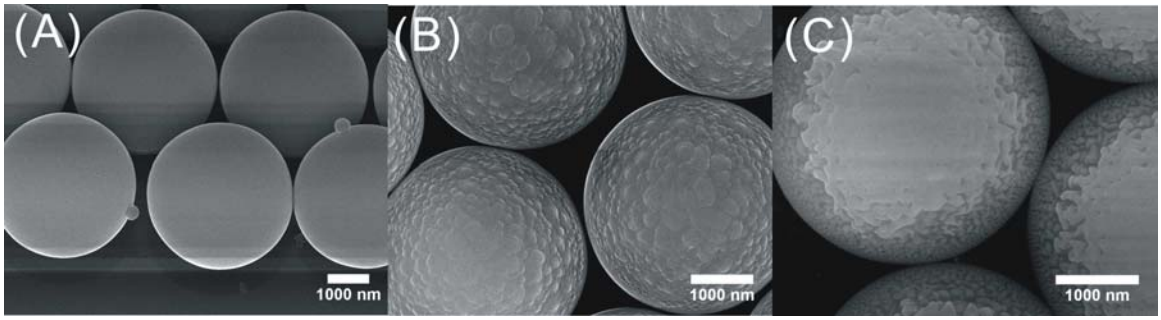

Figure 3-11. FE-SEM images of 4 μm silica beads coated with 20 nm of cobalt (A), nickel (B), and silver (C) after exposure to hydrogen sulfide for 24 hours.

Note from Figures 3-11B and 3-11C that these nickel and silver films also show significant changes in morphology, increasing in roughness and apparent grain size. The transformation from oxide to sulfide, accompanied by the formation of water as a product, possesses a more negative free energy of reaction, and thus a greater driving force (eq. 2). Moreover, significant changes in morphology between the oxide and the sulfide facilitate the diffusion of the hydrogen sulfide gas, making complete conversion from the oxide to the sulfide more likely. These varied results suggest that oxidation processes may be performed before sulfidation reactions in the cases of some metals to create MO//MS structures.

$$M_xO\ (s) + H_2S\ (g) \rightarrow M_xS\ (s) + H_2O\ (g) \qquad (2)$$

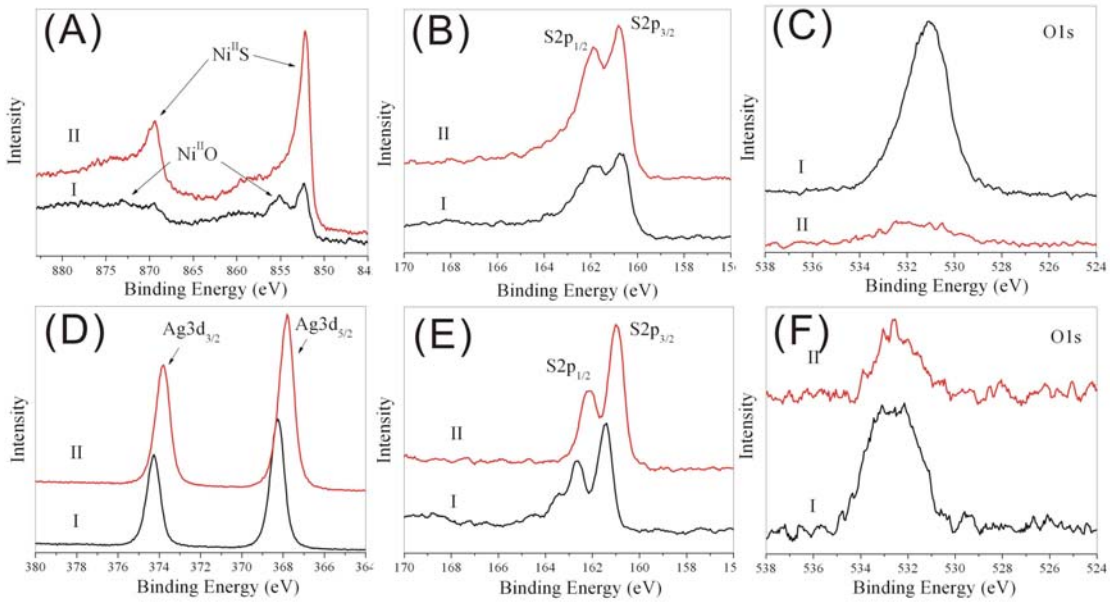

Figure 3-12. XPS depth profile spectra of 4 μm silica beads coated with 20 nm of nickel (A-C) and silver (D-F) after exposure to hydrogen sulfide for 24 hours. Nickel: (A) Ni 2p, (B) S 2p, and (C) O 1s; silver: (A) Ag 3d, (B) S 2p, and (C) O 1s.

Several typical examples of chemically transformed BJPs through post-fabrication transformation are illustrated in Fig. 3-13. After exposure to hydrogen sulfide or oxygen plasma, the parent Ag//Ni and Au//Ag BJPs were transformed into Ag_2S//NiS (both metals were sulfidized), Au//Ag_2S (only Ag was sulfidized), Ag_2O//NiO (both metals were oxidzied), and Au//Ag_2O (only Ag was oxidized). The assignment of the materials on each hemisphere is verified based on the EDS point measurement and the apparent morphology as well (Fig. 3-14). Figure 3-15 lists several examples of chemically transformed BJPs through intermediate transformation. For instance, the Ag_2O//Ag JPs were prepared starting from silica particles half-coated with Ag (Ag-SiO_2 JPs), followed by plasma oxidation of silver, inversion, and deposition with Ag on the other hemisphere (Figure 3-15A). Instead of oxidation, when sulfidation was first carried out to the Ag-SiO_2 JPs, the Ag_2S//Ag JPs were produced (Figure 3-15B). Starting from the Ag_2S//Ag JPs, the following oxidation reaction only occurred to the silver coating, resulting in Ag_2S//Ag_2O mixed type of JPs (Figure 3-15C,D). In this case, Ag_2S is thermodynamically more stable than Ag_2O.

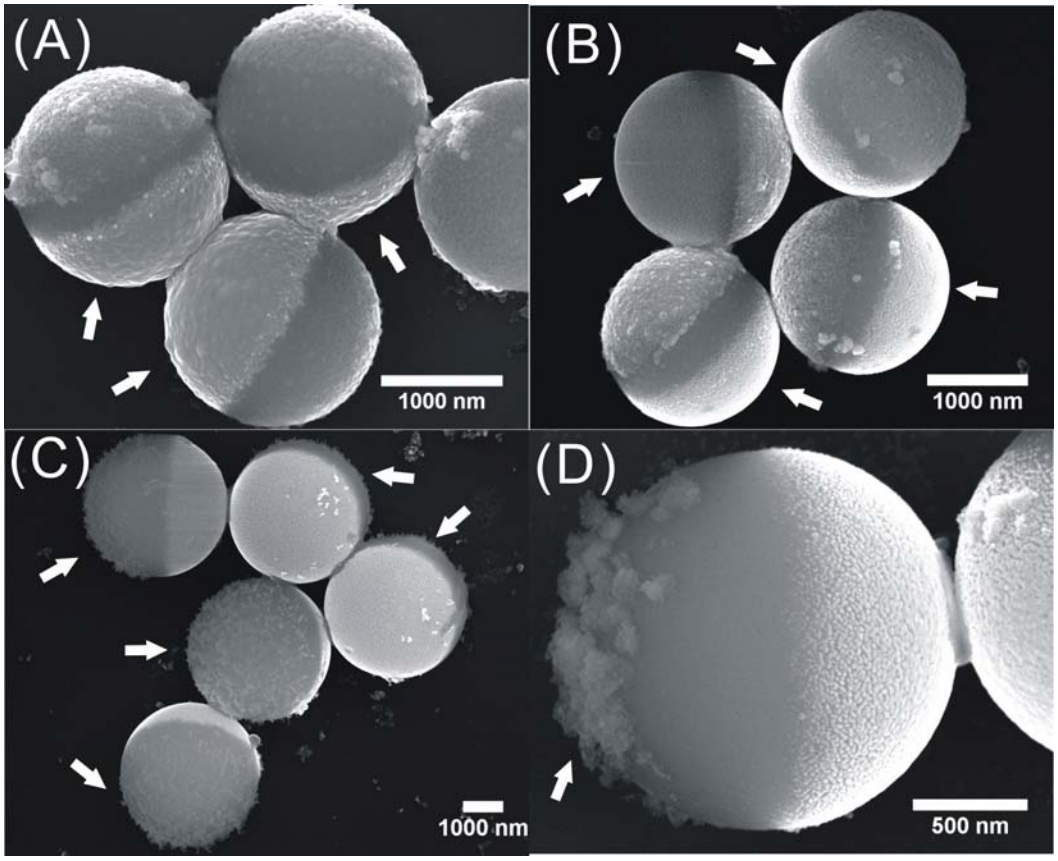

Figure 3-13. FE-SEM images of chemically transformed BJPs through post-fabrication transformation: (A) Ag_2S//NiS; (B) Au//Ag_2S; (C) Ag_2O//NiO; (D) Au//Ag_2O. The arrows depicted in the figure show (A) NiS, (B) Au, (C) Ag_2O, and (D) Ag_2O.

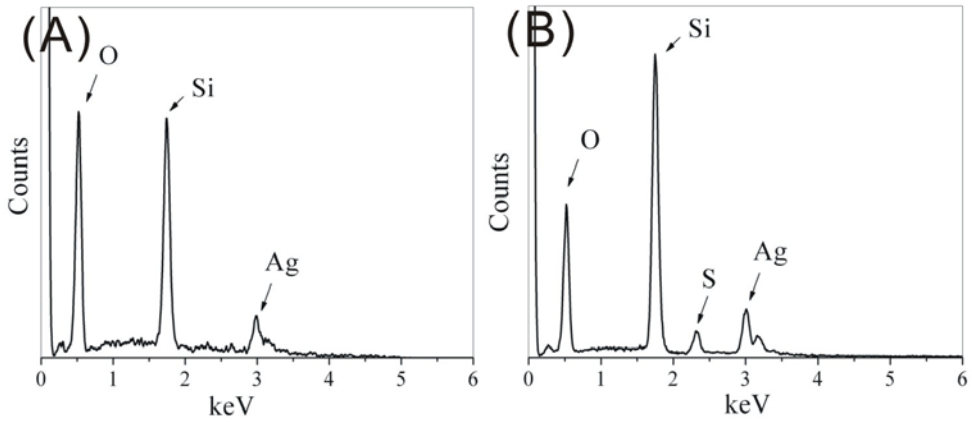

Figure 3-14. EDS point spectra of (A) Ag and (B) Ag_2S on 2μm of Ag_2S//Ag JPs.

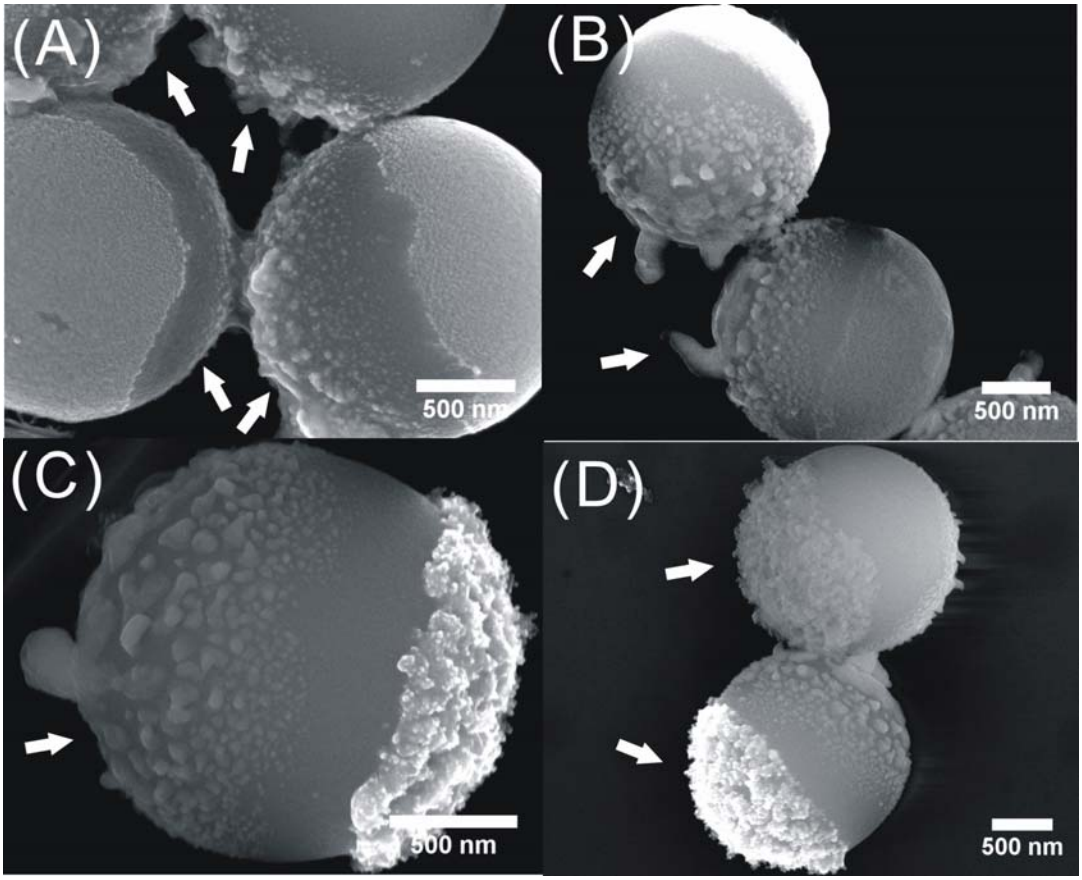

Figure 3-15. FE-SEM images of chemically transformed BJPs through intermediate transformation: (A) Ag_2O//Ag; (B) Ag_2S//Ag; (C,D) Ag_2S//Ag_2O. The arrows depicted in the figure show (A) Ag_2O, (B) Ag_2S, (C) Ag_2S, and (D) Ag_2O.

Due to the transformation from metal to metal oxide or sulfide, the new JPs possess additional versatility in surface chemistry compared to their parent BJPs. This versatility allows a broader library of functional groups, i.e. thiols, carboxylates, phosphates, phosphonates, silanes, isocyanates, sulfates, etc, to be used for selective or specific modification of the surface properties of the JPs such as hydrophobicity, electrical charge, protein resistance or adsorption for applications in biomedicine and biosensors. The combination of two distinctly different materials with different conductivities or band gaps has potential for unique photochemical and photocatalytic behaviors. Further investigation on the optical properties of the new JPs is being pursued.

In summary, bimetallic Janus particles can be successfully transformed into JPs with various combinations of metals, metal oxides and metal sulfides through solid-gas heterogeneous reactions. It is certain that other reaction systems could chemically transform BJPs. Most importantly, the vast library of materials that are possible suggests two significant outcomes. First, new properties lead to new applications – BJPs can be envisioned in applications in device design, self-assembly, sensing components, and optical materials, such as photonic crystals. Second, to design such systems requires a means to manipulate JPs, probably through externally accessible physical properties provided by the transformations. For instance, electric, optical or magnetic fields would play a significant role in control of the orientation of the JPs through polarization or magnetic interaction with the anisotropic structures leading to formation of extended arrays.[10,22,23] The use of more than one component to manipulate transformed BJPs in a design-specific manner could lead to use in applications such as targeted cargo transportation and the fabrication of photonic crystals.

3.4 Model Studies of Oxidation of Ultrathin Metal Films

The demand of manufacturing novel microelectronics such as integrated circuits, transistors and other device structures has stimulated a great deal of interest in methods of providing thin films of metals, dielectrics, as well as semiconductors.[24] Chemical transformation from material to material is a commonly used approach with high effectiveness and reliability. Most metals can be transformed through various chemical methods, including ion exchange,[25-27] thermal annealing,[28,29] surface functionalization,[30] to produce thin films of dielectrics and semiconductors with desired properties. For instance, some metals can be easily transformed into oxides, chalcogenides or other species, which endows the resulting materials with different electronic, optical and magnetic properties. Among those methods, oxidation and sulfidation are two simple and useful processes for metal transformation.[31,32]

In the presence of an oxidizing atmosphere, a metal's resistance to oxidation is one of the most important properties. Most pure metals react spontaneously with oxygen in air to form a very thin, passive layer of the oxide film. These thin film oxides protect

the underlying metal from further oxidation at room temperature. The so-called native oxides may not change the major properties of the bulk metals themselves, but will have significant influences on the surface. This metal oxide layer, therefore, may cause important practical consequences, especially when the metals are in the case of thin films. It is not surprising that researchers have been focusing on the oxidation resistance of these materials to corrosion and degradation for centuries, not only under room temperature conditions but also at high temperatures and other severe environments.[33]

Plasma oxidation processes have been extensively employed for surface modification, playing an important role in the fabrication of various microelectronic devices.[34-36] Although the detailed mechanisms remain unclear, surface oxidation and hydroxylation are strongly accelerated by the presence of highly reactive oxygen radicals and ions. It is necessary to study the oxidation behavior of metal thin films in air-oxygen plasma, understanding the change in the microstructure and some physical properties, such as hardness and electrical conductivity, compared to those naturally oxidized in air.

A major concern in many industrial installations is the corrosion of metals induced by sulfur containing species, which is usually much more severe than by oxygen, due to high defect concentration and thus, poor protective properties of the sulfide scales.[37] Hydrogen sulfide (H_2S) is a gaseous molecule and, among all the sulfur-containing species, has the lowest molecular weight (In nature, elemental sulfur usually exists in the formation of allotropes). Therefore, H_2S is regarded as one of the principle atmospheric corrosive agents for metals due to its high mobility in air and acidic nature.[38]

In this section, we will demonstrate the oxidation and sulfidation of metal thin films using XPS depth profiling, X-ray diffraction (XRD) and scanning electron microscopy (SEM). These metals, including aluminum (Al), titanium (Ti), cobalt (Co), nickel (Ni), and silver (Ag), are deposited on a silicon wafer substrate via electron-beam evaporation to form a thin layer approximately 20 nm thick. The information on compositions and valence states of the metals after exposure to air plasma and H_2S will be provided depending on a combinatorial method of characterization. The ultimate goal of this work is to be able to explore the reaction mechanisms of various metals in the

state of thin film, including aluminum, titanium, cobalt, nickel, and silver, upon plasma oxidation and sulfidation compared to their corresponding bulks.

3.4.1 Oxidation

(1) Aluminum thin film

Aluminum is known as a reactive metal but the native oxide formed at the surface protects the underlying metal from further oxidation. It is reported that the air-formed amorphous oxide scale is only 2-3 nanometers in thickness.[39] This thin oxide layer was verified by analyzing a 200 nm aluminum film deposited on a silicon substrate after exposure to air for 30 days. Surprisingly, the native oxide layer very well protected the underlying aluminum from oxidation by air plasma. This could be easily evidenced by the great similarity of the XPS depth profile spectra of this specimen before and after plasma exposure. Figure 3-16 illustrates the XPS spectra of the plasma exposed aluminum thin film, whose surface shows a couple of Al 2p peaks at the binding energies of 74.5 eV and 71.3 eV, respectively. The peak appearing at higher binding energy could be attributed to aluminum with a valence state of +3 while the peak at lower binding energy could be ascribed to metallic aluminum.[40,41] Subsequently, argon ion etching was introduced to remove the surface contaminants, particularly adventitious hydrocarbons, and possibly, part of the oxides from the very top surface as well. The relative area for both Al 2p peaks increases correspondingly with the disappearance of the C 1s peak after the initial etching (etch time = 0.05 min). As the etching proceeded, the Al 2p peak area at lower binding energy increased while the peak area at higher binding energy decreased. This indicates that the content of metallic aluminum on the bulk of the inner part was more abundant than that on the surface of the outer part. It should be noted, however, that the peak intensity of Al(0) decreased while the intensity of Al(III) increased upon approaching to the substrate; and the Al(0) completely disappeared, left with only the Al(III) peak at etch time = 44.55 min. Correspondingly, the O 1s peak decreased at the beginning (after t = 0.05 min), and then remained almost constant, and finally, increased again at the interfacial region of the thin film sample and the substrate, which will be discussed below.

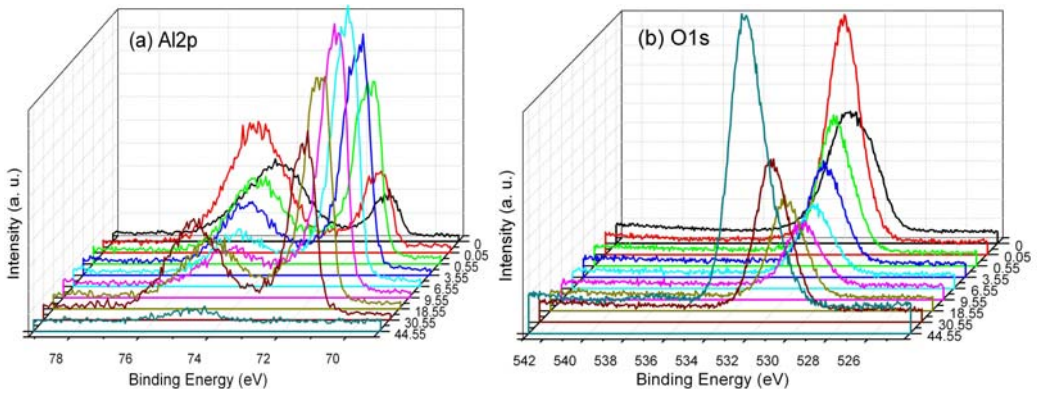

Figure 3-16. XPS depth profiles of 200 nm of aluminum thin film on a silicon substrate after exposure to air plasma: (a) Al2p and (b) O 1s. Including this and all the following XPS depth profile plots, the horizontal axes represent the binding energy (eV), the 45-degree tilted axes represent the etch time (minute), and the vertical axes represent the intensity (arbitrary unit).

Interestingly, however, the spontaneous oxidation diverges in the case of a thinner layer of 20 nm aluminum. Unlike the 200 nm aluminum specimen, it is surprising to see only a single Al 2p peak at the binding energy of 74.6 eV, accompanying with an O 1s peak at 531.4 eV. Even after etching through the film, no Al(0) peak was observed in the expected region; instead, the Al 2p peak shifted to 75.7 eV, ascribed to Al(III), and the O 1s peak shifted to 532.2 eV, and both were present throughout the entirety of the thin film (Figure 3-17). This indicates that the 20 nm thick Al layer had been quantitatively transformed into oxide after exposure to air. Therefore, it is easily anticipated that a treatment with air plasma would not have a further effect on the depth on the formed alumina.[40]

(2) Titanium thin film

After exposure to air, the titanium thin film formed an ultrathin layer of TiO_2 according to the XPS results. As shown in Figure 3-18, the respective binding energy for Ti $2p_{3/2}$ and $2p_{1/2}$ was 458.4 eV and 464.3 eV, which is typical for Ti (IV) from TiO_2. Beneath the layer of titanium dioxide, titanium has a mixed oxide layer denoted as TiO_{2-x}. This is identified as a shoulder centered at 456.6 eV on the low binding energy side of the Ti $2p_{3/2}$ after depth profiling.[42] It should be noted that both of Ti $2p_{3/2}$ peaks

corresponding to TiO_2 and TiO_{2-x} decayed very rapidly as sputter etching proceeded, whereas the presence of a new peak at 454.6 eV became dominative. This downhill-shifted binding energy for Ti $2p_{3/2}$ (Δ_{BE} = 3.8 eV) is an indicative of a gradual change in the valence state from +4 to +2, also in good agreement with the literature.[43]

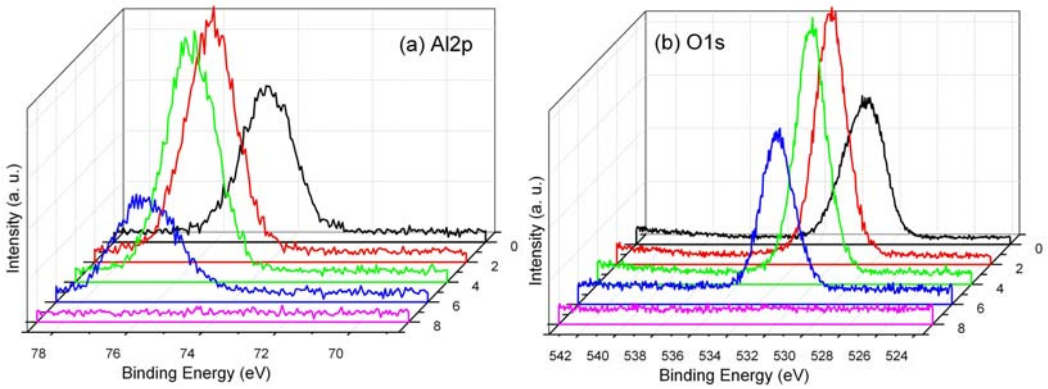

Figure 3-17. XPS depth profiles of 20 nm of aluminum thin film on a silicon substrate upon exposure to atmosphere: (a) Al 2p and (b) O 1s.

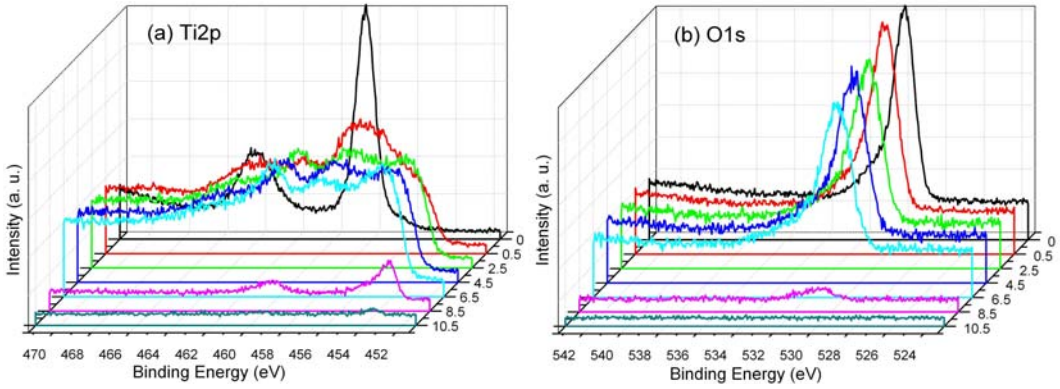

Figure 3-18. XPS depth profiles of 20 nm of titanium thin film on a silicon substrate upon exposure to atmosphere: (a) Ti 2p and (b) O 1s.

Upon treatment with air plasma, there was no significant difference in the depth of the three distinct oxide layers. The behavior of the successive decrease in the binding energy of the Ti $2p_{3/2}$ peaks over the etching period was the same as the atmosphere sample (Figure 3-19). The XRD provides complementary evidence to support that a wurtzite structure of TiO is the major phase while TiO_2 (and TiO_{2-x}) at surface were too thin to detect (Figure 3-20). One might expect exposure to air plasma to further oxidize

the TiO film to TiO_2. However, this did not occur, suggesting a dense oxide protected the underlying film.

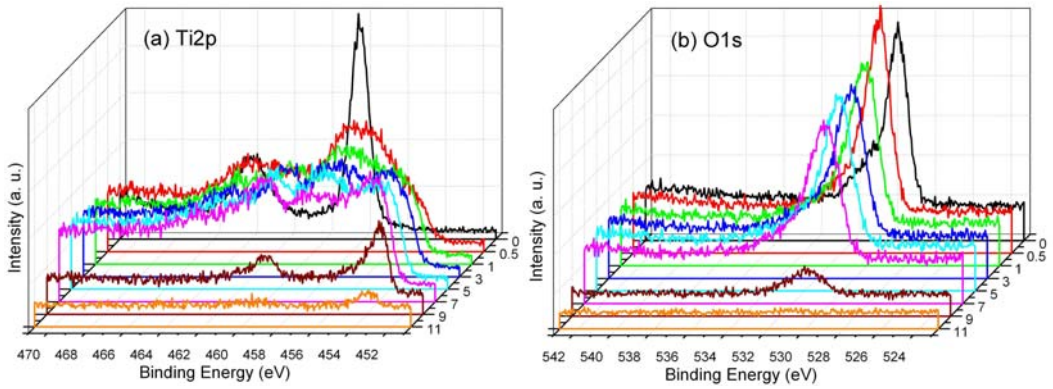

Figure 3-19. XPS depth profiles of 20 nm of titanium thin film on a silicon substrate after exposure to air plasma: (a) Ti 2p and (b) O 1s.

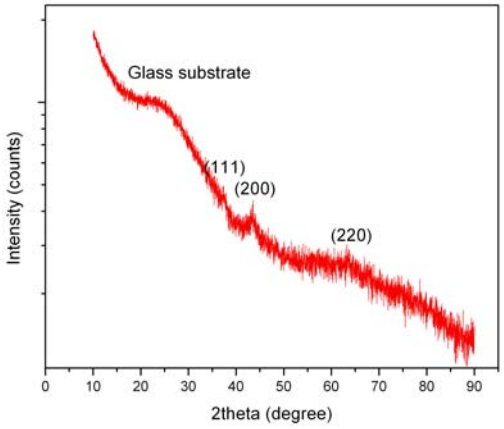

Figure 3-20. XRD pattern of 200 nm of titanium thin film on a glass slide after exposure to plasma, which indicates a wurtzite structure of TiO (PDF#00-008-0117) similar to NaCl.

(3) Cobalt thin film

Cobalt is an example of a highly efficient protective oxide coating that prevents complete oxidation of the thin film. This protective oxide layer formed spontaneously upon exposure to air. The location of a pair of Co 2p peaks at 780.4 eV ($2p_{3/2}$) and 795.9 eV ($2p_{1/2}$) suggested a valence state of +2 for cobalt (Figure 3-21). Note, however, that a

small shoulder peak at 778.0 eV on the lower binding energy side of the Co $2p_{3/2}$ peak, was indicative of metallic cobalt. The Co $2p_{3/2}$ shoulder peak along with the arising of a shoulder peak corresponding to Co $2p_{1/2}$ at 793.4 eV turned into the dominant species during etching. The total disappearance of the Co^{2+} peak occurred after etching for 60 seconds, along with the simultaneous disappearance for the O 1s peak at 529.8 eV indicates the CoO layer was approximately 2 nm thick.[44]

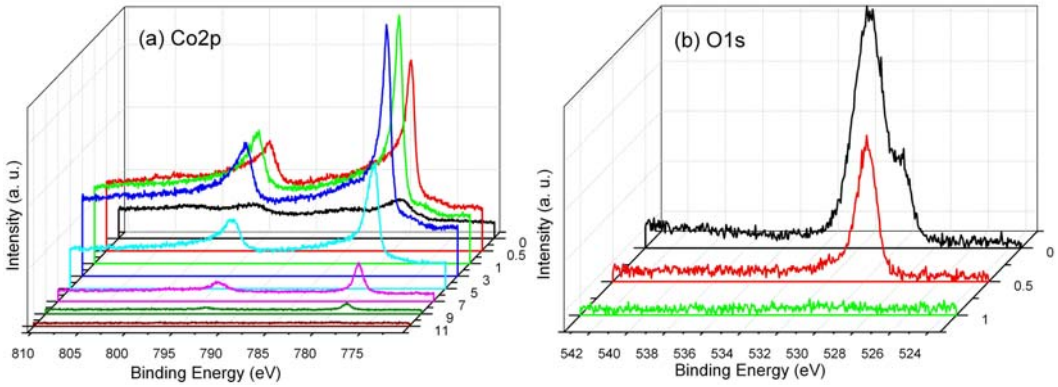

Figure 3-21. XPS depth profiles of 20 nm of cobalt thin film on a silicon substrate upon exposure to atmosphere: (a) Co 2p and (b) O 1s.

After exposure to oxygen plasma for 30 minutes, no shoulder peak around 778.0 eV for Co (0) was visible until the specimen had been etched for 60 seconds (Figure 3-22). According to the O 1s traces in XPS depth profiling, the CoO was completely etched away after 3 minutes of etching, which suggested an increased thickness of the oxide layer. The oxide layer was measured to be approximately 4 nm thick. A prolonged oxygen plasma exposure (5.5 hours) induced a slight increase in the thickness of the oxide layer.

(4) Nickel thin film

There was only a very thin layer of oxide detected on the surface of nickel in comparison to that of cobalt. Two pairs of peaks with different assignable species of nickel and comparable intensities were observed initially before etching; one pair was attributed to NiO, locating at 856.4 eV (Ni $2p_{3/2}$) and 874.2 eV (Ni $2p_{1/2}$), the other pair was from the metallic nickel, locating at 852.3 eV ($2p_{3/2}$) and 869.6 eV ($2p_{1/2}$) (Figure 3-

23).[45] The intensity of O 1s peak dramatically dropped down to zero after a very short period of etching (0.15 min). The thickness of the oxide scale was estimated as 0.3 nm according to the etch time.[46]

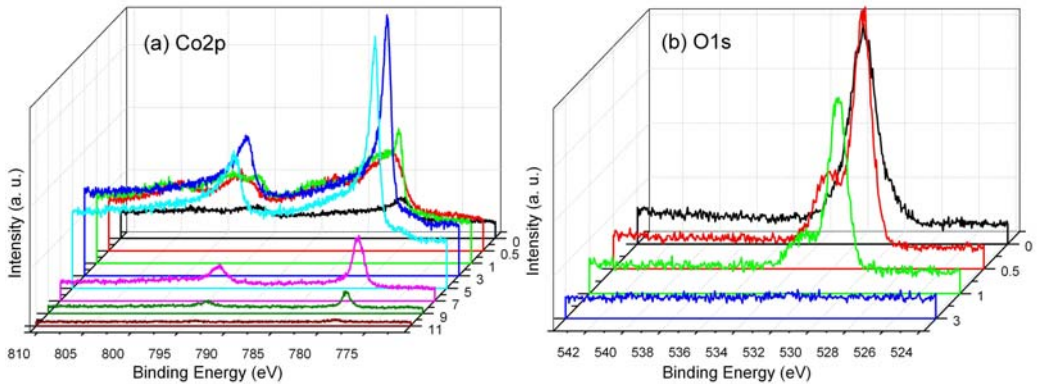

Figure 3-22. XPS depth profiles of 20 nm of cobalt thin film on a silicon substrate after exposure to air plasma for 30 minutes: (a) Co 2p and (b) O 1s.

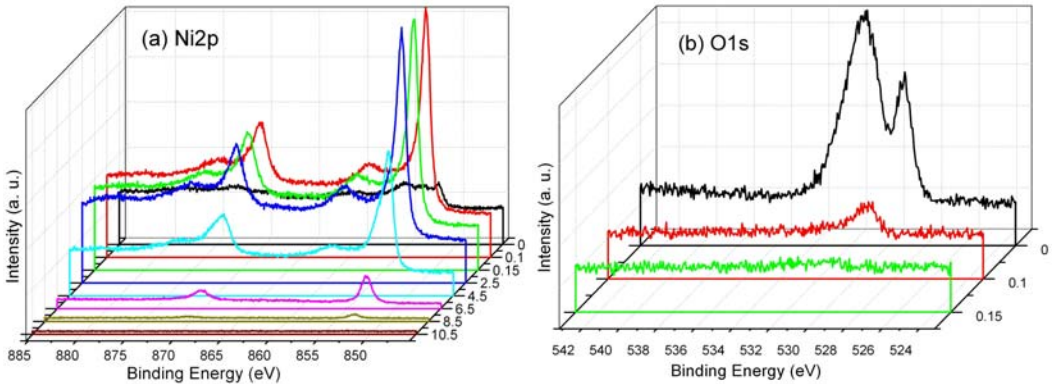

Figure 3-23. XPS depth profiles of 20 nm of nickel thin film on a silicon substrate upon exposure to atmosphere: (a) Ni 2p and (b) O 1s.

Similar to cobalt, the thickness of NiO on the top surface increased to 1.2 nm after exposure to air plasma for 30 min (Figure 3-24). The Ni 2p peaks attributed to the metallic nickel were almost invisible, but they did appear immediately after an initial sputter etching (t = 0.05 min). A longer time exposure experiment (5.5 hours) was also performed in this case; however, it only led to little influence as to cobalt.

(5) Silver thin film

The formed passive oxide was possibly thin enough to be removed together with the surface adventitious hydrocarbons during initial etching. As shown in Figure 3-25, the intensity of the couple of Ag 3d peaks, lying at the binding energies of 368.4 eV and 374.4 eV, decreased gradually while the O 1s peak at 531.2 eV disappeared immediately upon etching.

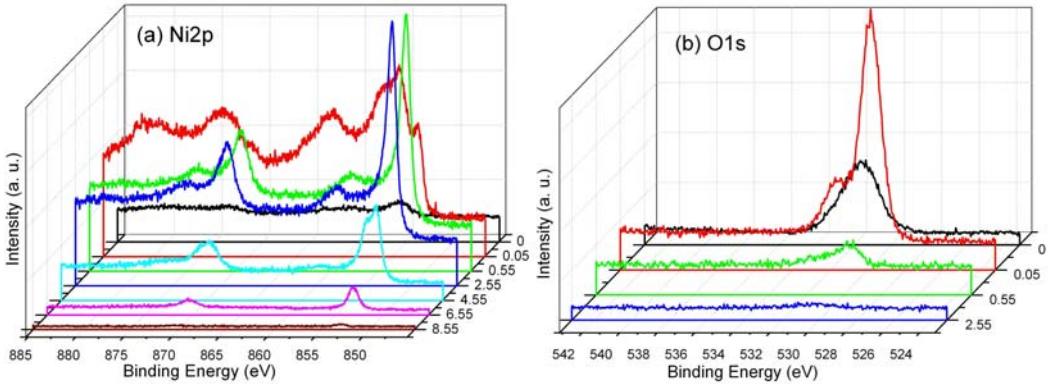

Figure 3-24. XPS depth profiles of 20 nm of nickel thin film on a silicon substrate after exposure to air plasma for 30 minutes: (a) Ni 2p and (b) O 1s.

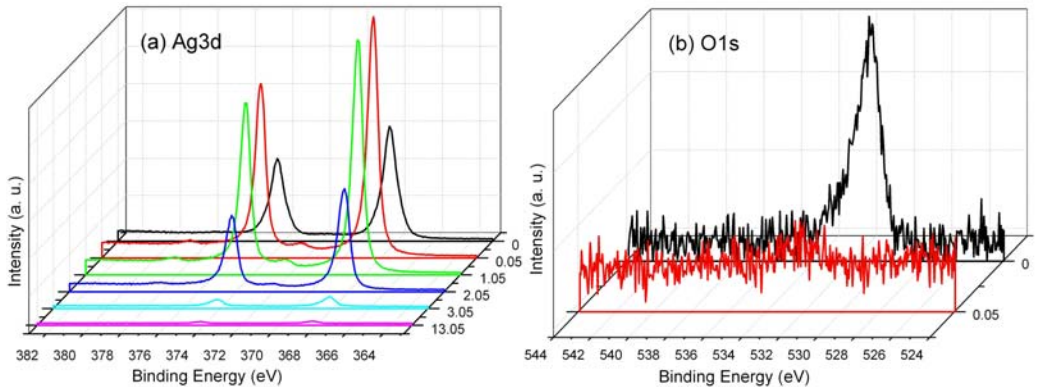

Figure 3-25. XPS depth profiles of 20 nm of silver thin film on a silicon substrate upon exposure to atmosphere: (a) Ag 3d and (b) O 1s.

A morphological change in silver was caused by exposure to air plasma. The SEM imaging showed that the silver changed from a continuous thin film to discrete particulate structures (Figure 3-26). The dimension of those islands ranged from tens to

hundreds of nanometers, which is smaller than the spot size of the X-ray source used in XPS. Therefore, it would be hard to tell whether the silver underwent complete or partial oxidation due to the interference of O 1s from the substrate. However, these discrete structures were identified as a mixture of silver and silver oxide by depositing 20 nm of silver on a silicon substrate pre-coated with 20 nm of gold. As shown in Figure 3-27, the Ag $3d_{5/2}$ and $3d_{3/2}$ peaks located at lower binding energies of 368.1 eV and 374.1 eV, respectively, but both gradually shifted to higher binding energies with a value of 0.7 eV upon etching; the O 1s peak were observed with a decrease in intensity and almost disappeared completely after etching for over 10 min. Meanwhile, the XRD provided information of the plasma exposed silver thin film with a composite structure of Ag and Ag_2O (Figure 3-28).[47,48] In the case of 20 nm of silver thin film after plasma exposure, only the crystalline silver can be resolved, while in the case of 200 nm of silver thin film, both metal and metal oxide structures can be easily differentiated. We believe that the morphological change must have been accompanied with a structural change in our case, however, the silver thin film underneath the islands were protected from plasma oxidation.

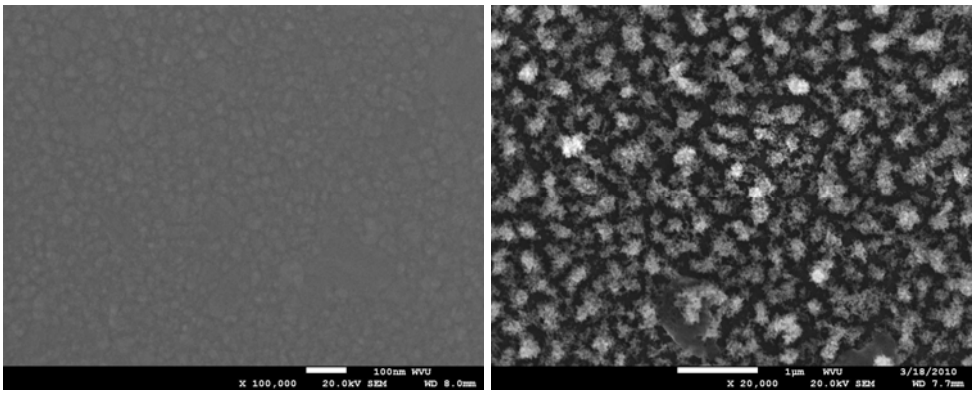

Figure 3-26. FE-SEM images of 20 nm of silver on a silicon substrate (a) before and (b) after exposure to air plasma. Scale bar: (a) 100 nm; (b) 1 µm.

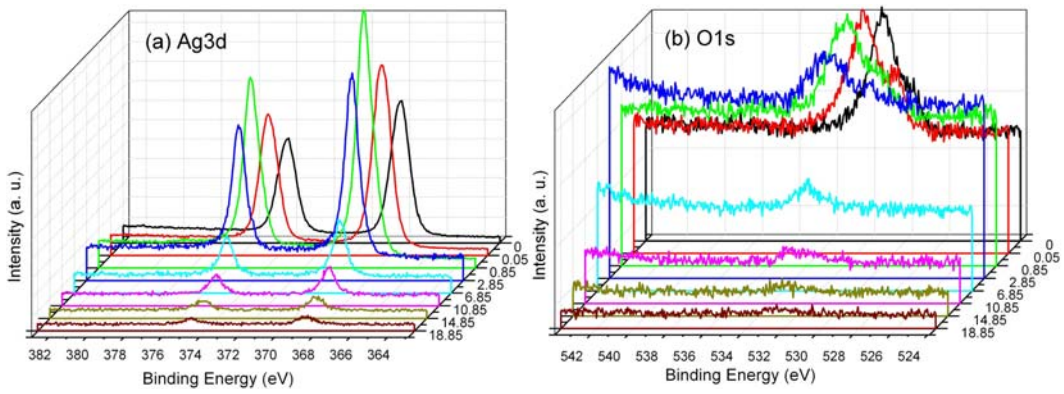

Figure 3-27. XPS depth profile of 20 nm of silver thin film on a 20 nm gold-coated silicon substrate after exposure to air plasma for 30 minutes: (a) Ag 3d and (b) O 1s.

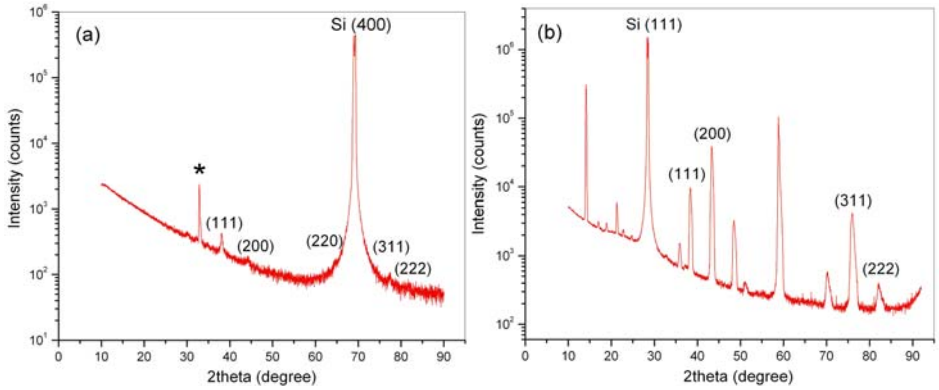

Figure 3-28. XRD patterns of (a) 20 nm and (b) 200 nm of Ag silver thin film on silicon substrates after exposure to air plasma. Note that the indexed peaks are assigned to the metal silver and the symbol * in panel (a) represents the impurity from the Si (100) substrate.

3.4.2 Sulfidation

(1) Aluminum and titanium thin films

In the case of air-exposed aluminum and titanium thin films, their compositions remained unchanged in the presence of H_2S at room temperature. No S 2p peak was detected in the expected binding energy range, indicating no sulfur present in the samples. Neither the shape nor the relative area of the metal peaks had apparent changes.

Furthermore, the sole presence of O 1s peaks suggested that both the surfaces of Al and Ti thin films were occupied with oxides.

(2) Cobalt thin film

As shown in Figure 3-29, the peaks for metallic Co $2p_{3/2}$ and $2p_{1/2}$ were distinctively observed, locating at 777.8 eV and 792.8 eV, respectively. However, it can be clearly seen from the initial XPS curve that a pair of peaks located at 780.6 eV and 796.6 eV, which indicated for the Co 2p peaks for higher valence states. The fact that the air-exposed cobalt thin film was immersed into an environment filled with H_2S for 24 hours might lead to sulfidation of the specimen. Unfortunately, there is a potential difficulty in differentiating the high valence Co peaks from the oxide to the sulfide due to the only 1 eV difference in binding energy.[45] The intensity for the Co (II) peak began to decay very rapidly after etching for 0.15 min and the Co (0) peak first went up and then remained constant at binding energy of 777.8 eV till the X-ray approached the interface of cobalt and the silicon substrate. This is consistent with the disappearance of the S 2p line after 0.25 min and then the O 1s line soon followed between 0.45 and 0.75 min. This suggested a minimal three-layered profile of Co thin film after exposure to air and subsequent transfer to the H_2S environment, which comprised with a top layer of CoS with an estimated thickness of 1.7 nm, a middle layer of 2.3 nm CoO and a bottom layer of Co intact from oxidation and sulfidation. The thickness of each layer was estimated based on the etching time and the assumption of the same etching rate for each material thin layer. However, we could not rule out the possibility that the top layer of CoS was transformed back to oxide upon exposure to air. The lack-of-evidence layer of the oxide was verified by using the small angle X-ray diffraction. As shown in Figure 3-30, the experimental X-ray reflectivity pattern was fitted remarkably well with a five-layered model using the GenX program,[49] which indicated that the thicknesses for each layered structure from top to bottom including CoO, CoS, CoO, Co and SiO_2 were 1.5, 3.1, 2.7, 22.1 and 1.2 nm, respectively. Note that the pre-treatment by air plasma produced an oxide layer on the top of the silicon substrate.

(3) Nickel thin film

Although nickel is next to cobalt in the VIII group of the periodic table, it has a completely different behavior with regard to sulfidation. Two major peaks at the binding energies of 852.5 eV and 869.7 eV are attributed to Ni $2p_{3/2}$ and $2p_{½}$, respectively, which matches well with NiS (Figure 3-31). Again, a layer of NiO could possibly form at the top surface of NiS, which is due to the co-existence of another Ni (II) $2p_{3/2}$ peak line at 855.6 eV. The Ni $2p_{3/2}$ signal from the NiO ultrathin layer was removed along with the O 1s peak after the initial etching. Unlike the case of the cobalt thin film, the O 1s peak was not detected afterwards while the S 2p peak was observed almost throughout the entirety of the nickel thin film, indicating that the nickel was fully sulfidized. Apparently, FE-SEM showed the morphological change of the nickel sulfide thin film, but the XRD could not resolve the crystal structure of the nickel sulfide possibly due to the poor crystallinity.

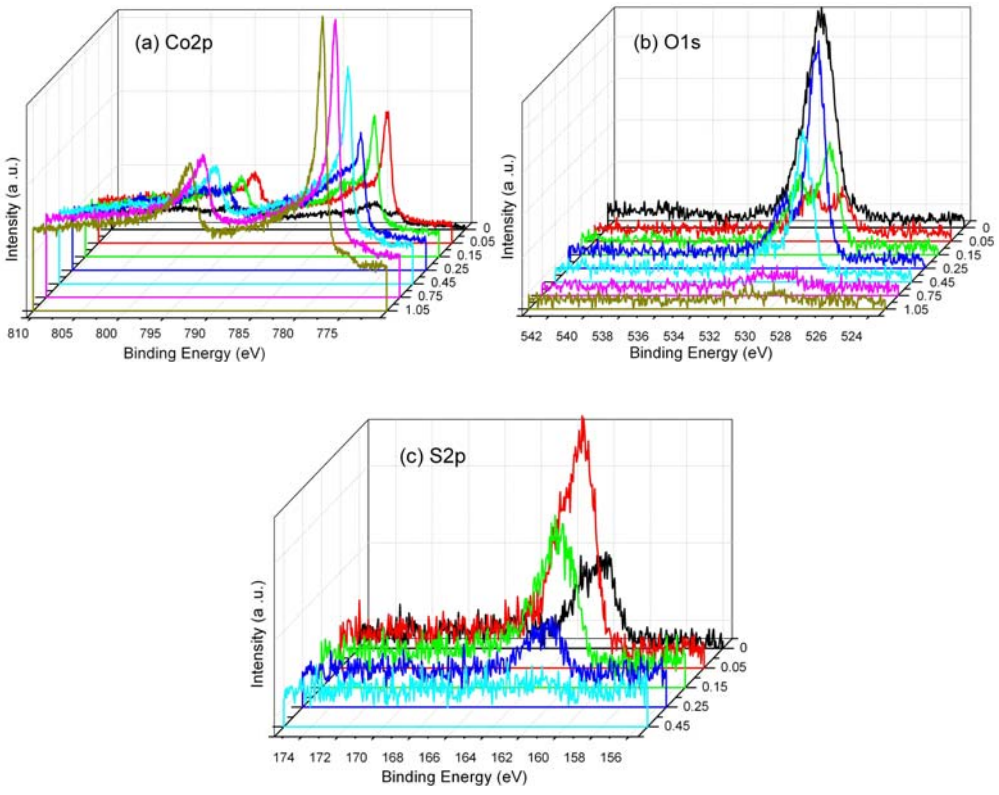

Figure 3-29. XPS depth profiles of 20 nm of cobalt thin film on a silicon substrate after exposure to H_2S for 24 hours: (a) Co 2p, (b) O 1s, and (c) S 2p.

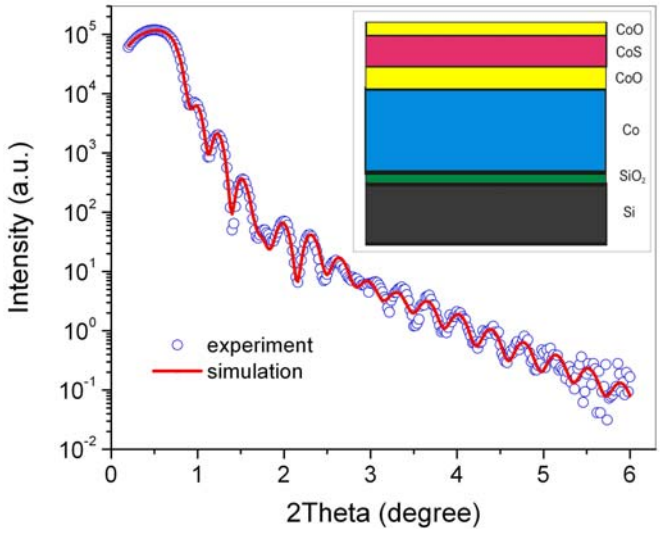

Figure 3-30. An X-ray reflectivity pattern (blue circle) of cobalt thin film after interaction with air and hydrogen sulfide. The red solid line is a simulation of the multilayer using GenX. Inset: a resolved five-layer geometry including the SiO_2 phase on the Si substrate.

(4) Silver thin film

Similar to nickel, silver reacted with hydrogen sulfide to effectively form silver sulfide. In metallic silver, it is observed the Ag $3d_{5/2}$ and $3d_{3/2}$ peaks are at 368.4 eV and 374.4 eV; after exposure to H_2S, as shown in Figure 3-32, we observed a slight downhill shift of binding energies to 368.2 eV and 374.2 eV, respectively. The possible oxide species on the surface was cleaned together with the native hydrocarbons by initial etching. A series of S 2s and 2p peak doublets penetrated down into the silver sulfide film and gradually decayed upon etching. Surprisingly, however, silicon signals were observed at the apparent etching time of 1 min and after. At that moment, our estimate was that the ion etching had not yet removed the specimen all the way down to the substrate due to a slow etching rate. Meanwhile, both the intensities of the Ag 3d and the S 2p lines were reasonably strong. However, only the substrate could account for the source of the silicon peak. Indeed, the FE-SEM image provided useful information - holes and cracks formed on the Ag thin film after sulfidation, which implied that the silicon substrate underneath those regions could be exposed to the X-ray during scanning

(Figure 3-33a). The XRD indicated that the final structure of the silver sulfide film was Ag_2S with a monoclinic symmetry of acanthite (Figure 3-33b).

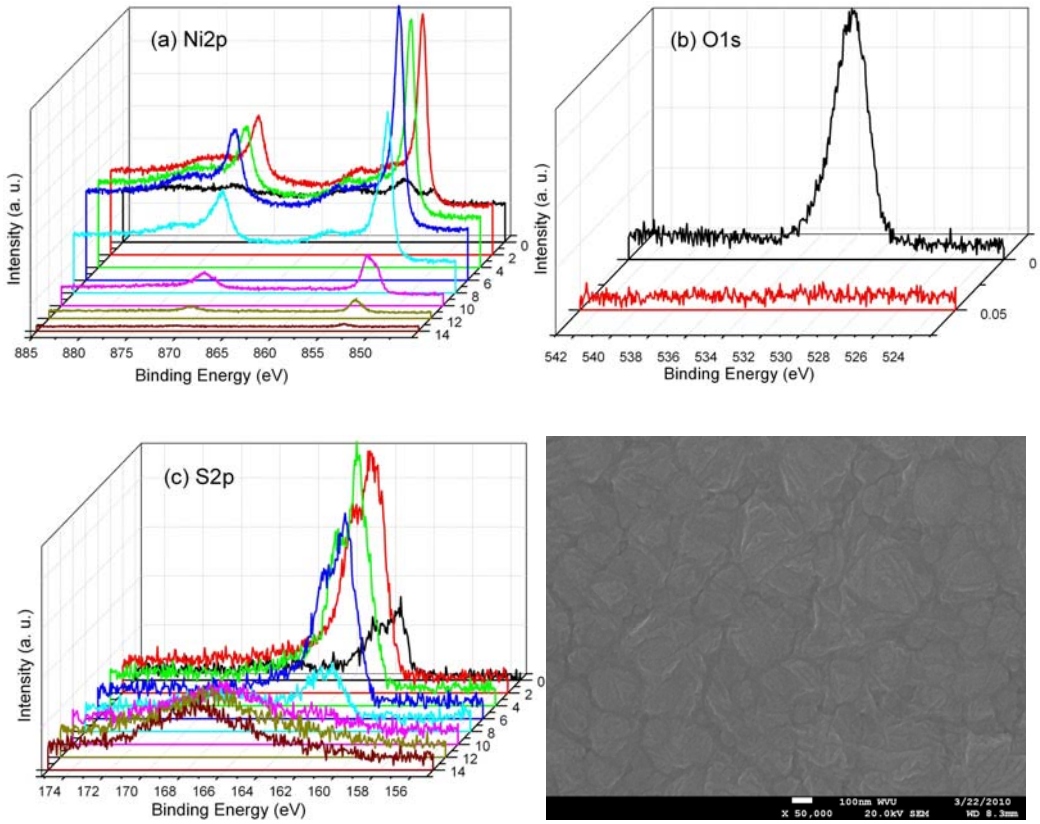

Figure 3-31. XPS depth profiles and FE-SEM image of 20 nm of nickel thin film on a silicon substrate after exposure to H_2S for 24 hours: (a) Ni 2p, (b) O 1s, (c) S 2p, and (d) FE-SEM image. The broad peaks around 167.6 eV, which appeared after etching for 10 min, were not designated. Scale bar: 100 nm.

The depth profile of the samples was obtained by combining a sequence of ion gun etch cycles with regular XPS measurements on each newly exposed surface. An argon ion gun was used to etch the surface with a certain period of time at a fixed etch power. The ion gun was programmed to turn off before acquiring the XPS spectra. The etch depth was then determined according to the overall thickness of the thin film and the etch time. In practice, the etch rate was material dependent and it would be ideal if standard samples were used for calibration. Our assumption was that the etch rates should

be comparable to each other when the samples were very thin. A complete disappearance of metal or metal ion peaks was considered as a sign of interface between two phases.

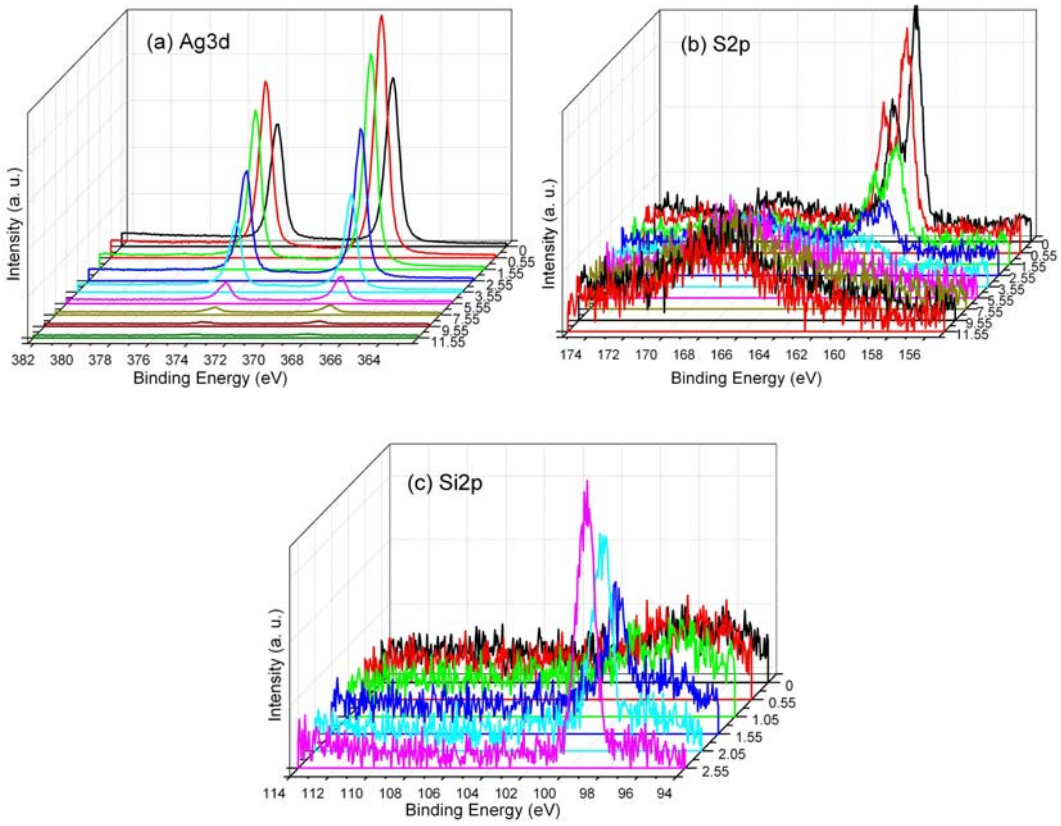

Figure 3-32. XPS depth profiles of 20 nm of silver thin film on a silicon substrate after exposure to H_2S for 24 hours: (a) Ag 3d, (b) S 2p and (c) Si 2p. Similar to the case of NiS, the peaks occurred at 167.6 eV were not designated.

Oxidation of metals is a thermodynamically favorable process. Full oxidation is expected without taking into consideration the possible formation of the passive oxide layer. Both the 20 nm of aluminum and titanium thin films are two good examples for this type of behavior. However, the aluminum formed a stratified composite consisting of a thin layer of alumina and the underlying metallic aluminum as the thickness of the film went up to 200 nm. The initial emergence of the metallic aluminum peak indicates that the oxide layer formed on the aluminum film must be thinner than 10 nm, which is typically the maximal detection depth of XPS technique. The full oxidation of 20 nm of aluminum can then be accounted for by the internal migration of oxygen;[50] the oxidation

not only occurred from the outside by air, but also at the interface where the native silicon oxide exchanged oxygen to the deposited metal. This was verified by the increase of the Al(III) 2p peak intensity at 74.5 eV when the X-ray was probing at the interfacial region in the case of the 200 nm film (Figure 3-16a).

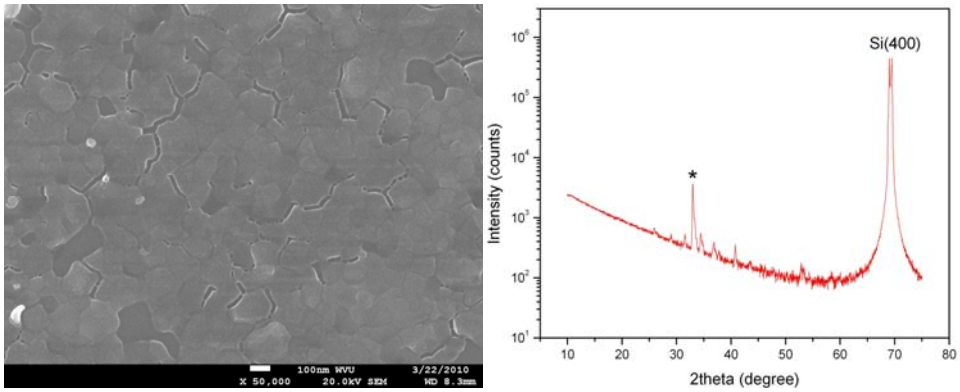

Figure 3-33. FE-SEM image (a) and XRD pattern (b) of silver sulfide film on a silicon substrate. Scale bar: 100 nm. The symbol * in panel (b) represents the impurity from the silicon substrate.

In addition, the O 1s peak never disappeared during the entire process of etching, indicating some oxidation throughout the film. The oxidation is likely due to the oxygen diffusion along grain boundaries in the metal film. Majority of the Co, Ni and Ag remained intact due to the protective thin layer of the oxides. The air-oxygen plasma provided a reactive media, and thus reduced the energy barrier of the oxidation. In the plasma's presence, Co and Ni underwent deeper oxidation to form thicker layers of the oxides whereas Ag went through changes in chemical composition (Ag_2O) and morphology (discrete particulate structure).

After exposure to atmosphere, aluminum or titanium was not observed to react with H_2S. This is due to the fact that H_2S was interacting with the oxides of Al and Ti, instead of the metallic surfaces. From the perspective of the reaction thermodynamics, most of the metal oxides have much lower Gibbs free energies of formation than their corresponding sulfides. It is favorable to transform the pure metals into sulfides through this solid-gas heterogeneous reaction. However, it would be thermodynamically unfavorable to convert the metal oxides into sulfides. The reactions that could have most

possibly occurred are illustrated below (Scheme 1); these positive values of Gibbs free energies of formation (ΔG^o)[51] at least imply that the sulfidation reactions of the oxide of Al or Ti would not occur spontaneously under our current experimental conditions.

Al_2O_3 (s) + 3 H_2S (g) = Al_2S_3 (s) + 3 H_2O (l) ΔG^o = 239.107 kJ/mol (1)

TiO (s) + H_2S (g) = TiS (s) + H_2O (l) ΔG^o = +39.393 kJ/mol (2)

TiO_2 (s) + 2 H_2S (g) = TiS_2 (s) + 2 H_2O (l) ΔG^o = +46.27 kJ/mol (3)

Scheme 1

In contrast to Al and Ti, conversion of oxides of Co, Ni and Ag to sulfides tended to be favorable, no matter whether they were pure metals or in the state of oxide thin films, which was the actual case that the surfaces of the metals were covered with a very thin layer of oxides. The possibly occurred reactions are listed in Scheme 2, indicating that the reactions between the oxides and hydrogen sulfide (eq. 5, 7, and 9) have more negative free energies of formation in comparison to the metal sulfidation (eq. 4, 6, and 8).

2 Ag (s) + H_2S (g) = Ag_2S (s) + H_2 (g) ΔG^o = -7.196 kJ/mol (4)

Ag_2O (s) + H_2S (g) = Ag_2S (s) + H_2O (l) ΔG^o = -233.153 kJ/mol (5)

Ni (s) + H_2S (g) = NiS (s) + H_2 (g) ΔG^o = -51.877 kJ/mol (6)

NiO (s) + H_2S (g) = NiS (s) + H_2O (l) ΔG^o = -77.479 kJ/mol (7)

Co (s) + H_2S (g) = CoS (s) + H_2 (g) ΔG^o = -59.36 kJ/mol (8)

CoO (s) + H_2S (g) = CoS (s) + H_2O (l) ΔG^o = -82.303 kJ/mol (9)

Scheme 2

As was previously discussed, both nickel and its native oxide reacted with hydrogen sulfide to favorably form nickel sulfide; this sulfidation reaction was also preferred for silver and its native oxide. It was anticipated that cobalt and its native oxide

would react the same way as nickel and silver, however, only the cobalt oxide on the top surface was able to react with H_2S. It is worthy to note that the thickness of the native cobalt oxide was much greater than that of nickel oxide and silver oxide. This layer of cobalt oxide significantly slowed down the reaction rate of plasma oxidation and could also play the same role to prevent hydrogen sulfide from penetration.

In Summary, thin metal film deposited on a flat substrate is an ideal platform not only for study of corrosion and resistance, but also for other purposes. For instance, chemical transformations on a flat surface would provide correlated important information into those substrates that do not have smooth surfaces but rough or curved features,[52] such as microspheres and carbon nanotubes. In this work, oxidative processes including (1) oxidation enhanced by oxygen-air plasma and (2) sulfidation with hydrogen sulfide have been investigated for metal thin films deposited on silicon wafer substrates. Upon exposure to atmosphere, most metal thin films tended to form a passive oxide layer at surface, which well protected the underlying material from complete oxidation by air plasma. In some cases, however, the impact of plasma oxidation did bring tremendous changes both in structure and morphology. Moreover, it is worthy to point out that the metal could be likely oxidized at the internal side in the presence of an oxygen-rich substrate. The native oxidation is a potential competition with the sulfidation that was carried out under our experimental conditions. The unfavorable thermodynamics provided a theoretical support to the failed sulfidation reactions between aluminum oxide (and titanium oxide) and hydrogen sulfide. There was no straightforward explanation for the partial sulfidation of the air-exposed cobalt thin film but we tended to agree that this reaction was slow compared to nickel and silver. We also believed that titanium could be fully sulfidized without exposure to atmosphere.[53]

References

(1) A. Perro, S. Reculusa, S. Ravaine, E. Bourgeat-Lami, E. Duguet, *J. Mater. Chem.* **2005**, *15*, 3745-3760.

(2) A. B. Pawar, I. Kretzschmar, *Macromol. Rapid Commun.* **2010**, *31*, 150-168.

(3) S. Jiang, Q. Chen, M. Tripathy, E. Luijten, K. S. Schweizer, S. Granick, *Adv. Mater.* **2010**, *22*, 1060-1071.

(4) S. C. Glotzer, M. J. Solomon, *Nat. Mater*. **2007**, *6*, 557-562.

(5) K. J. Lee, J. Yoon, J. Lahann, *Curr. Opin. Colloid Interface Sci.* **2011**, *16*, 195-202.

(6) J. Du, R. K. O'Reilly, *Chem. Soc. Rev.* **2011**, *40*, 2402-2416.

(7) J. Burdick, R. Laocharoensuk, P. M. Wheat, J. D. Posner, J. Wang, *J. Am. Chem. Soc.* **2008**, *130*, 8164-8165.

(8) S. Sundararajan, P. E. Lammert, A. W. Zudans, V. H. Crespi, A. Sen, *Nano Lett.* **2008**, *8*, 1271-1276.

(9) L. Hong, A. Cacciuto, E. Luijten, S. Granick, *Nano Lett.* **2006**, *6*, 2510-2514.

(10) S. Gangwal, O. J. Cayre, O. D. Velev, *Langmuir* **2008**, *24*, 13312-13320.

(11) L. Hong, A. Cacciuto, E. Luijten, S. Granick, *Langmuir* **2008**, *24*, 621-625.

(12) S. H. Kim, S. J. Jeon, W. C. Jeong, H. S. Park, S. M. Yang, *Adv. Mater.* **2008**, *20*, 4129-4134.

(13) K.-H. Roh, D. C. Martin, J. Lahann, *Nat. Mater.* **2005**, *4*, 759-763.

(14) S. M. Anthony, L. Hong, M. Kim, S. Granick, *Langmuir* **2006**, *22*, 9812-9815.

(15) T. Nisisako, T. Torii, T. Takahashi, Y. Takizawa, *Adv. Mater.* **2006**, *18*, 1152-1156.

(16) S. Jiang, M. J. Schultz, Q. Chen, J. S. Moore, S. Granick, *Langmuir* **2008**, *24*, 10073-10077.

(17) S. Ye, R. L. Carroll, *ACS Appl. Mater. Interfaces* **2010**, *2*, 616-620.

(18) S. Ye, R. L. Carroll, in preparation.

(19) L. Smardz, U. Kobler, W. Zinn, *J. Appl. Phys.* **1992**, *71*, 5199-5204.

(20) R. C. Ross, R. Sherman, R. A. Bunger, S. J. Nadel, *Sol. Energy Mater.* **1989**, *19*, 55-65.

(21) R. Chen, N. T. Nuhfer, L. Moussa, H. R. Morris, P. M. Whitmore, *Nanotechnology* **2008**, *19*, 455604.

(22) S. K. Smoukov, S. Gangwal, M. Marquez, O. D. Velev, *Soft Matter* **2009**, *5*, 1285-1292.

(23) S. Gangwal, A. Pawar, I. Kretzschmar, O. D. Velev, *Soft Matter* **2010**, *6*, 1413-1418.

(24) Grovenor, C. R. M. *Microelectronic Materials: Graduate Student Series in Material Science and Engineering*; Taylor & Francis Group: New York, 1998.

(25) Moon, G. D.; Ko, S.; Xia, Y.; Jeong, U. *ACS Nano* **2010**, *4*, 2307-2319.

(26) Yin, Y.; Rioux, R. M.; Erdonmez, C. K.; Hughes, S.; Somorjai, G. A.; Alivisatos, A. P. *Science* **2004**, *304*, 711-714.

(27) Robinson, R. D.; Sadtler, B.; Demchenko, D. O.; Erdonmez, C. K.; Wang, L.-W.; Alivisatos, A. P. *Science* **2007**, *317*, 355-358.

(28) Eze, F. C. *Semiconductor Science and Technology* **2001**, *16*, 362-366.

(29) Schaak, R. E.; Sra, A. K.; Leonard, B. M.; Cable, R. E.; Bauer, J. C.; Han, Y.-F.; Means, J.; Teizer, W.; Vasquez, Y.; Funck, E. S. *Journal of the American Chemical Society* **2005**, *127*, 3506-3515.

(30) Sperling, R. A.; Parak, W. J. *Philosophical Transactions of the Royal Society A: Mathematical, Physical and Engineering Sciences* **2010**, *368*, 1333-1383.

(31) Seybolt, A. U. *Advances in Physics* **1963**, *12*, 1-43.

(32) Lai, G. Y. *High-Temperature Corrosion And Materials Applications*; ASM International: USA, 2007.

(33) Roberge, P. R. *Corrosion Basics: An Introduction*; 2 ed.; NACE International: Houston, 2006.

(34) Taylor, S.; et al. *Semiconductor Science and Technology* **1993**, *8*, 1426-1433.

(35) Liston, E. M.; Martinu, L.; Wertheimer, M. R. *Journal of Adhesion Science and Technology* **1993**, *7*, 1091-1127.

(36) Gourrier, S.; Bacal, M. *Plasma Chemistry and Plasma Processing* **1981**, *1*, 217-232.

(37) Mrowec, S. *Oxidation of Metals* **1995**, *44*, 177-209.

(38) ‡Hydrogen Sulfide Corrosion: Its Consequences, Detection and Control,† United States Environmental Protection Agency, Office of Water, 1991.

(39) Shimizu, K.; Kobayashi, K.; Thompson, G. E.; Wood, G. C. *Oxidation of Metals* **1991**, *36*, 1-13.

(40) Lu, F.-H.; Tsai, H.-D.; Chieh, Y.-C. *Thin Solid Films* **2008**, *516*, 1871-1876.

(41) Jeurgens, L. P. H.; Sloof, W. G.; Tichelaar, F. D.; Mittemeijer, E. J. *Thin Solid Films* **2002**, *418*, 89-101.

(42) Babelon, P.; Dequiedt, A. S.; Mostéfa-Sba, H.; Bourgeois, S.; Sibillot, P.; Sacilotti, M. *Thin Solid Films* **1998**, *322*, 63-67.

(43) Trofimov, V. I.; Sushkova, N. M.; Kim, J.-I. *Thin Solid Films* **2007**, *515*, 6586-6589.

(44) Smardz, L.; Kobler, U.; Zinn, W. *Journal of Applied Physics* **1992**, *71*, 5199-5204.

(45) Moudler, J. F.; Stickle, W. F.; Sobol, P. E.; Bomben, K. D. *Handbook of X-ray Photoelectron Spectroscopy*; Eden Prairie: Physical Electronics, 1995.

(46) Mathieu, H. J.; Datta, M.; Landolt, D. *Journal of Vacuum Science & Technology A: Vacuum, Surfaces, and Films* **1985**, *3*, 331-335.

(47) Ross, R. C.; Sherman, R.; Bunger, R. A.; Nadel, S. J. *Solar Energy Materials* **1989**, *19*, 55-65.

(48) Sahm, H.; Charton, C.; Thielsch, R. *Thin Solid Films* **2004**, *455-456*, 819-823.

(49) Bjorck, M.; Andersson, G. *Journal of Applied Crystallography* **2007**, *40*, 1174-1178.

(50) Campbell, C. T. *Surface Science Reports* **1997**, *27*, 1-111.

(51) Barin, I. *Thermochemical Data of Pure Substances*; VCH: Germany, 1995.

(52) Ye, S.; Carroll, R. L. *ACS Applied Materials & Interfaces* **2010**, *2*, 616-620.

(53) Dubrovskaya, G. N. *Powder Metallurgy and Metal Ceramics* **1965**, *4*, 701-704.

Chapter 4

Autonomous Motion and Directed Motion

4.1 Background

Self-propelled particles have been widely studied in biological systems, such as the actin polymerizing bacteria *Listeria monocytogenes* in cells and cell extracts and similarly behaving biomimetic polystyrene particles coated with the bacterial protein ActA.[1-3] Recently, nonbiological micro- to nanoscale particles have been investigated that convert chemical energy into translational motion.[4] These systems provide an opportunity to explore mechanisms of chemomechanical energy transduction and offer a link to self-propelled particles in living systems.

In early studies, Whitesides and co-workers[5] investigated the propulsion of millimeter-scale objects by the catalytic decomposition of hydrogen peroxide on a platinum surface. More recently, Mallouk and co-workers[4,6-8] developed and characterized self-propelled asymmetric nanorods, prepared by the electrodeposition of Au and Pt. When the rods were suspended in dilute solutions of H_2O_2, video microscopy revealed that they were propelled generally in the direction of the Pt end of the rod. This propulsion direction was surprising in view of the study by Whitesides and co-workers,[5] in which the motion generally occurred in a direction away from the Pt-coated region, with the propulsion depending on the production of O_2 bubbles from the decomposition of H_2O_2. Mallouk and co-workers,[4,6-8] proposed that the nanorods, composed of disparate metals in contact with one another, electrochemically generate a localized electrophoretic and proton field that induces motion of the rod through the surrounding fluid. Extensive studies by Mallouk, Sen, and co-workers,[8-15] Ozin and co-workers,[16-18] and Velegol and co-workers[19,20] have identified a number of metallic nanorod systems that convert the fuel molecules hydrogen peroxide and hydrazine into translational and rotational motion.

A study of self-propelled, Pt-coated polystyrene particles was recently reported by Howse et al.,[21] which showed that coating one hemisphere of the particle with Pt is sufficient for self-propulsion in dilute H_2O_2 solutions. The propulsion velocity obtained from the mean-squared displacement of the asymmetrically coated microspheres, also known as “Janus particles”, was found to increase with increasing hydrogen peroxide concentration. They proposed a mechanism involving diffusiophoresis, in which spatially asymmetric production of product molecules leads to propulsion of the particles.[21-23]

Theoretical studies of nanodimers by Ruckner and Kapral[24] showed that the propulsion can be understood in terms of a concentration gradient established by the catalytic production of product and a difference in the forces of molecular collisions with the catalytic and noncatalytic surfaces. In all of the studies of self-propelled particles, a common feature is a structural asymmetry that gives rise to a gradient of the product species.

Studies of self-propelled particles have focused primarily on particle velocity as a function of the concentration of reactant, usually H_2O_2, which fuels the propulsion. Tracking and motion analysis typically has been carried out at 36 frames per second (fps) or less. Optical microscopy of Pt-Au nanorods has allowed directionality coefficient analysis, which suggests that directionality is lost at low (<5.0%) hydrogen peroxide concentrations.[4] The direction of motion relative to the orientation of the particle was not determined in the studies of asymmetrically Pt-coated polystyrene particles by Howse et al.[21]

In section 4.3, experiments are carried out with silica particles that are asymmetrically coated with Pt and immersed in H_2O_2 solutions, similar to the system studied by Howse et al.[21] The focus of this study is on the particle orientation with respect to the direction of motion, which is investigated with velocity autocorrelation and propulsion direction analyses. Typically, about 20 particles are tracked with images collected at 45-55 fps. An increase in average particle speed with increasing H_2O_2 concentration is found, in agreement with Howse et al.,[21] where speed reflects the average distance traveled between video image frames. The velocity is found to be highly correlated on short time scales and the particle orientation to be highly correlated with the direction of motion.

This self-propelled particle system differs from previously studied systems in that the particle motion occurs effectively in two dimensions. The 1 μm Pt-silica particles in our experiments have a higher density than the aqueous H_2O_2 solutions and settle to the bottom of the thin layer of solution. These 1 μm particles are found to move freely, both as self-propelled Pt-silica particles in H_2O_2 solutions and as Pt-silica particles or silica particles undergoing Brownian motion in water in our control experiments. The particle

speeds are likely affected by particle-surface interactions, as the 1 μm particles move in the boundary layer at the glass microscope slide surface. However, such interactions do not affect the correlation of particle motion with particle orientation, and the effectively two-dimensional motion allows accurate characterization of the particle movement and orientation. Larger 4 μm particles exhibited restricted movement or were stationary in our experiments.

The chemically powered motion of Janus particle system exhibits directed motion at short time scales but with an overall random behavior at long time scales. Huge benefit will be garnered if the particles can be steered from one position to another by taking advantage of the propulsion force. The precise control of the motion is required to achieve practical applications.[25] The velocity of the particle may be accelerated, for example, by changing the catalyst,[26,27] fuel composition,[15,27,28] fuel concentration,[21,29] ionic strength,[13] to extend the non-Brownian motion to a longer time scale. However, these "internal" forces would not allow us to control the motion. In order to remotely control the direction of motion, several types of interactive external forces such as electric field,[30,31] magnetic force,[27,32-34] light,[35,36] heat,[37,38] have been implemented. Incorporation of magnetic materials into the bimetallic nanorod motor system has been demonstrated as an elegant way to achieve remote control, which possesses great potential from the perspective of practical application, such as cargo transport in solution and microfluidic channel networks, and possibly, drug delivery.[33, 39]

The controlled motion based on the colloidal JPs is expected to be different from the bimetallic nanorod system due to the difference in particle shape and metal configuration. In section 4.4, magnetic materials (i.e. nickel) were introduced as the steering source through supplementary deposition between silica surface and platinum in a JP system. Platinum not only played a substantial role as the catalytic source of autonomous motion of the JPs, but also in the protection of nickel from oxidation. The magnetization of the new Janus particles has been extensively characterized, both theoretically and experimentally, and these results are presented. The presence of magnetic materials on the JPs allows the orientation of the individual particle, and thus, the direction of motion to be influenced. In an applied field, the directed motion is found to be dominated by linear translational diffusion whereas the non-linear translational and

rotational diffusions were not completely suppressed, which is due to the nature of Brownian motion.

4.2 Experimental Section

4.2.1 Preparation of Silica Particles Half-Coated with Platinum or Nickel/Platinum.

A dilute aqueous suspension of washed 1 μm silica particles (Bangs Laboratories, 0.96 μm, 15% coefficient of variation) was deposited on a coverslip (1.8 × 1.8 cm^2) that had been cleaned in Piranha solution (1:3 mixture of 30% H_2O_2 and 18 M H_2SO_4). After evaporation of the bead solution, a predominantly close-packed, single layer of particles was formed on the substrate. A layer of Pt ~5 nm thick was subsequently deposited onto the particles using e-beam evaporation (Temescal BJD-2000) at ~10^{-6} Torr, producing particles that are approximately half-coated with platinum metal. The half-coated particles were released from the coverslip by sonication in water. In the case of magnetic Janus particle (Pt/Ni-SiO_2) preparation, 4 μm silica particles were used and the thickness of metal is 50 nm for nickel and 10 nm for platinum.

4.2.2 Reaction Mixture Preparation, Particle Tracking, and Data Analysis.

Small ~2 μL aliquots of the suspended particle solution were mixed with hydrogen peroxide solution to form particle suspensions with desired H_2O_2 concentrations. Particle motion was captured using an Olympus IX-81 optical microscope with a 100× oil objective, which was fitted with a Photronics Cascade 512B camera (Figure 4-1). In order to maximize frame capture rate, small regions were selected from the field of view that contained one or more particles. The particle motion was then captured at the highest possible frame rate. Images were background corrected and segmented using the software ImageJ.[40] The particle motion was tracked using Video Spot Tracker software (v05.20),[41] which provided the 2D position of the particle and the corresponding frame time.

Because the magnetic Janus particles are denser than water, they started settling to the bottom of the meniscus within a short period of time (a few tens of seconds). The particles could be easily focused at the solid-liquid interface and exhibited clear half-dark

(the metal hemisphere) and half bright (the silica hemisphere) features under the transmission mode. A pair of permanent magnets was evenly lined up at either side of the sample meniscus with a constant distance of 3 cm. The strength of the magnetic field where the meniscus located was measured to be ~600G using 5180 Gauss/Tesla meter. Images of particle motion were captured at a frame rate of 15.8 frames per second (fps).

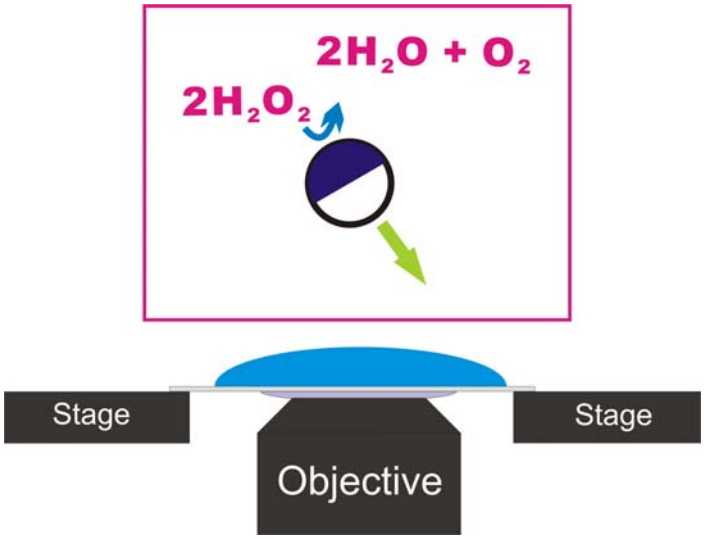

Figure 4-1. Experimental setup of the particle motion.

4.2.3 Decomposition of H_2O_2 in the presence of nickel and platinum pellet.

The catalytic decomposition of hydrogen peroxide (10.0% w/w) by the metal pellets was carried out in a glass vial at room temperature. The nickel/platinum pellet with dimension of 3.1 mm × 3.3 mm (diameter × height) was placed at the bottom of the vial, immersed with 3 mL of 10% H_2O_2. Top face of the pellet was adjusted to focal plane under a 5× objective (Olympus BX51). The reaction was recorded through imaging every 2 seconds (at a rate of 0.5 frames per second, fps) in order to compare the reaction rate with platinum pellet according to the generation of oxygen bubbles.

4.3 Autonomous Motion of Pt-Silica Janus Particles in H_2O_2 Solutions*

The dynamical behavior of the self-propelled particles is controlled by the rotational and translational contributions to the motion of the particles. We have monitored the autonomous motion of Pt-silica particles in hydrogen peroxide solutions

* Part of this work is published on Journal of Physical Chemistry A (2010).

using high-speed, high-resolution imaging (up to 150 fps) and frame-by-frame particle tracking in order to determine the particle orientation relative to the direction of motion. Image segmentation allows the Pt-silica particle symmetry axis to be identified in each frame. Figure 4-2 illustrates three typical 2D movement trajectories of 1 μm Pt-silica particles in water and 15.0% and 27.3% H_2O_2. According to the trajectories in the same length scale, the autonomous motion appeared to be more spread out than the Brownian motion.

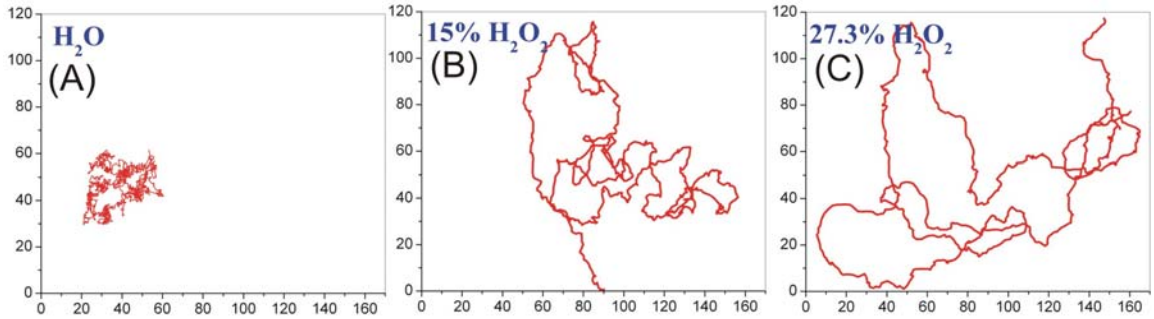

Figure 4-2. 2D movement trajectories of 1 μm Pt-silica particles in (A) water and (B) 15.0% and (C) 27.3% H_2O_2

An example of the particle motion analysis is shown in Figure 4-3A, in which three sequential bright-field optical micrographs of a 1 μm Pt-silica particle are superimposed. Sequences of micrographs were flat-field corrected to remove background intensities. The particle is shown at time intervals of ~650 ms in three successive positions during its autonomous motion in a solution of 27.3% H_2O_2. The three images were chosen from a series of images taken at ~55 fps, with every 36th frame selected. The bright region of the particle is the result of a lensing effect of the Kohler illumination of the uncoated half of the silica microbead. The dark region stems from the high extinction coefficient of the Pt-coated half of the particle.

The surface plot in Figure 4-3B shows the intensity of light transmitted by the particle, with the Pt-coated and silica regions appearing as a valley and a peak, respectively. The orientation of the particle in a particular frame can be determined by considering the extrema of the valley and peak components to be the centers of the Pt-coated and silica regions. Using the background intensity as the reference intensity, each raw image is segmented into two images: one for the Pt-coated region, with intensities

less than the reference intensity, and one for the uncoated silica region, with intensities greater than the reference intensity. The two sets of images are then independently tracked to generate an array of *x*-*y* location information at subpixel resolutions by kernel matching with interpolation.

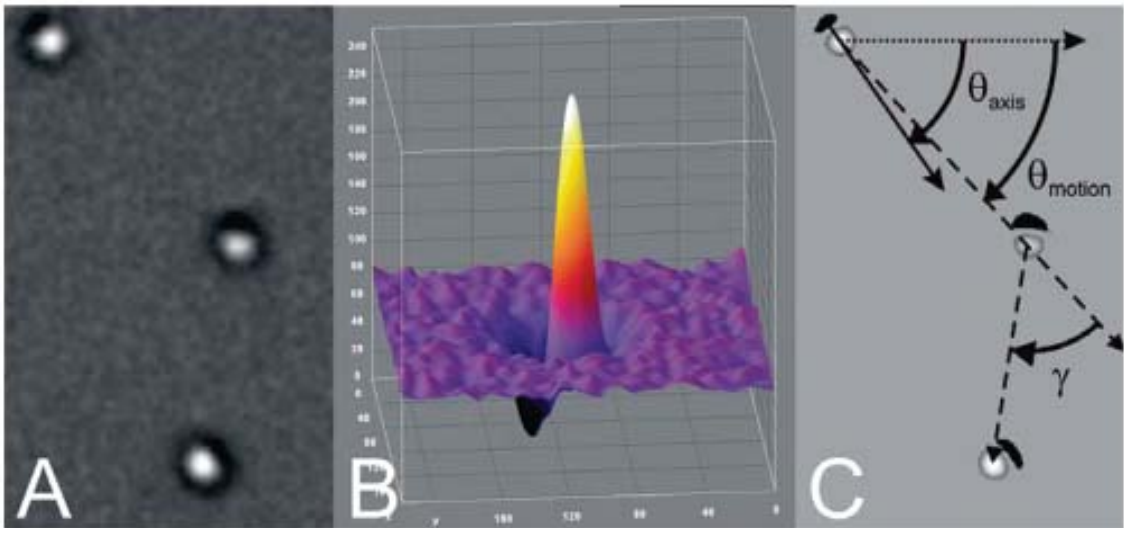

Figure 4-3. (A) Overlay of three sequential optical micrographs of a half-coated Pt−silica particle undergoing autonomous motion. (B) Surface plot of transmitted light intensity for a single Janus particle. (C) Segmented and background subtracted images of particles from (A) highlighting the silica region (bright) and the Pt-coated region (dark), along with the angles and trajectories that are used in the motion analysis (see Appendix).

Figure 4-3C shows segmented images from the raw image data in Figure 4-3A, with superimposed particle orientation and translation vectors for the motion analysis described below. The combined segmented images clearly show the Pt-coated (black) and the uncoated silica (light gray) regions of the particle. The Pt-coated region of the particle may be smaller due to the vapor deposition procedure; however, the apparent size may also be distorted by the lensing effect of the uncoated silica region. From the *x*-*y* position of the uncoated silica region of the particle and the time interval between sequential images, the frame-to-frame trajectory and angle of motion θ_{motion} can be determined. In addition, the particle orientation angle θ_{axis} is defined by a vector from the intensity minimum corresponding to the Pt-coated side of the particle to the intensity maximum corresponding to the uncoated silica side. The trajectory vectors provide the particle

velocity, and the directional changes of the particle defined by the angle γ can be evaluated from sequential images. These quantities allow an analysis of the particle orientation with respect to its translational motion as a function of time.

A comparison can be made between the particle orientation and the direction of motion from the angle information given by θ_{axis} and θ_{motion} in Figure 4-3C. Figure 4-4 shows a plot of the normalized distribution of the minimum absolute difference between the two angles, $\delta\theta = |\theta_{axis} - \theta_{motion}|$. The value of $\delta\theta$ gives the deviation of the translation direction from the orientation direction of the Pt-silica particle. In the case where the particle travels in a direction exactly in line with its orientation, with the Pt-coated region to the rear, $\delta\theta = 0$. The occurrence plot in Figure 4-4 shows that θ_{axis} and θ_{motion} coincide to a remarkable degree, consistent with our video observations and the velocity autocorrelation analysis described below. We note that there is little difference in this analysis between the occurrence distribution for particles in 15.0% and 27.3% H_2O_2 solutions.

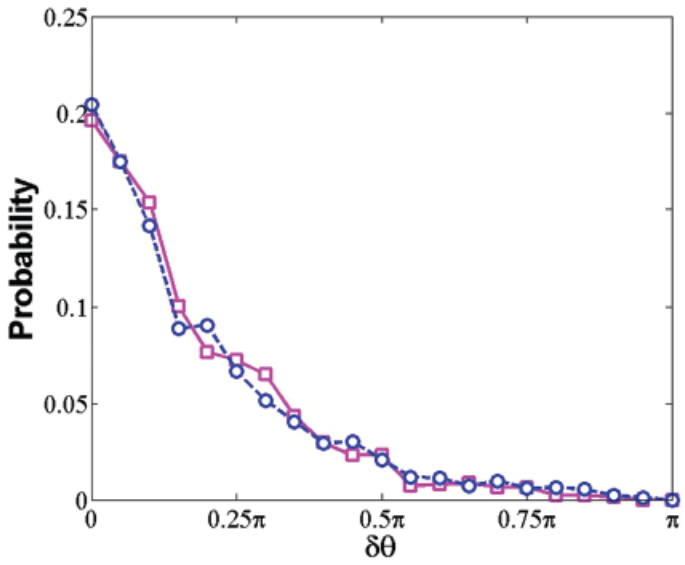

Figure 4-4. Plot of normalized occurrence distribution of $\delta\theta = |\theta_{axis} - \theta_{motion}|$ for half-coated Pt-silica particle motion in 15.0% (□) and 27.3% w/w H_2O_2 (○) solutions. Plot constructed from over 2000 and 1300 frames of tracked motion, respectively.

Mean squared displacement as a function of lapsed time is a typical approach to differentiate the autonomous motion from Brownian motion.[21] Figure 4-5 illustrates the

mean squared displacement for 1 μm silica particle in water, 1 μm Pt-silica particle in water, 15.0% H_2O_2 and 27.3% H_2O_2. In the absence of hydrogen peroxide, the curves for both silica particle and Pt-silica particle are linear with small slopes, indicating a simple diffusive behavior. With addition of hydrogen peroxide, the slope of the curves for 15.0% H_2O_2 goes up, and for 27.3% H_2O_2, even higher. Note that the parabolic component of the curves for 15.0% H_2O_2 and 27.3% H_2O_2 at short time scales suggests the presence of propulsion force.

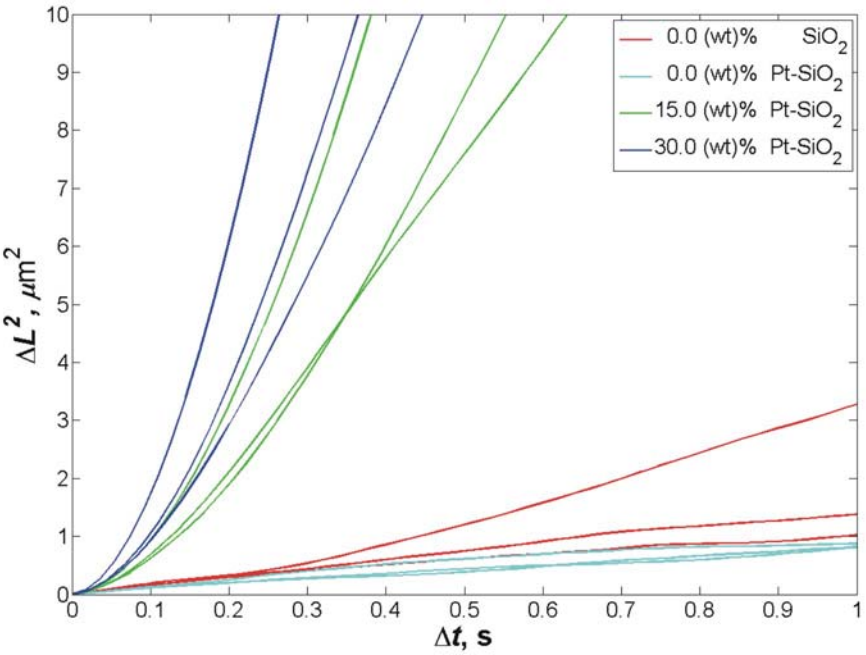

Figure 4-5. Mean squared displacement (ΔL^2, μm^2) as a function of lapsed time (Δt, s)

However, the mean squared displacement is a convolution of all types of motion. In order to understand the instantaneous behavior of the particle motion, a directional angle analysis is developed. The distribution of the directional angle γ for uncoated silica particles and Pt-silica particles in water and Pt-silica particles in H_2O_2 solutions is shown in Figure 4-6. For each solution, 3000 frames were analyzed for the particle motion. Here γ is defined as positive for clockwise changes in direction, $\gamma \in (0, \pi]$, and negative for counterclockwise changes in direction, $\gamma \in (-\pi, 0]$, with $\gamma = 0$ corresponding to no directional change. We see that there is virtually no directional preference for silica particles or Pt-silica particles in water at the observation time intervals $\Delta t = 0.021$ (Figure 4-6a) and 0.022 (Figure 4-6b), reflecting the random selection of directional changes that

accompanies Brownian motion. In contrast, there is a distinct directional preference for half-coated Pt-silica particles in 15.0% and 27.3% solutions of H_2O_2 at the observation time intervals Δt = 0.019 (Figure 4-6c) and 0.018 s (Figure 4-6d), with a narrowing distribution for the solution with the higher concentration. These distributions show that the self-propelled particle travels in the same or nearly the same direction in the subsequent image frame, and the probability of the directional motion increases with increasing H_2O_2 concentration. For Pt-silica particles in 27.3% solutions of H_2O_2, the probability of continuing to travel in nearly the same direction is about 3 times as likely as for these particles in water. The probability of moving at right angles ($\pi/2$ or $-\pi/2$) is about half as likely, and the probability of moving in the opposite direction (π) is very unlikely. Figure 4-6d,e,f shows the distribution of the directional angle γ for Pt-silica particles in 27.3% solutions of H_2O_2 with increasing effective observation time interval Δt = 0.018 s (d), 0.36 s (e) and 0.73 s (f), respectively. The distribution of γ broadens as Δt is increased, indicating that the apparent motion becomes more Brownian-like as the observation time interval becomes comparable to or larger than the rotational diffusion time τ_R,[21] as discussed below.

An analysis of the velocity autocorrelation function is consistent with the directional angle distributions. The normalized velocity autocorrelation function for three silica particles and three Pt-silica particles in water are shown in parts a and b of Figure 4-7, respectively. The velocities of these particles exhibit little if any correlation, with the autocorrelation function quickly falling to zero. The velocity autocorrelation function for half-coated Pt-silica particles in 15.0% and 27.3% solutions of H_2O_2 is shown in parts c and d of Figure 4-7, respectively. The analysis is again carried out for three particles in each case. In contrast to the behavior of particles in water, we now see very strong correlations in the particle velocities, with a general trend of the autocorrelation function decreasing to zero at ~0.5 s. In both cases, the autocorrelation function decreases to slightly negative values after a falloff from large positive values, consistent with our observations of looping behavior at long times described below. In each experiment, a particle was observed for ~5 s, with a camera frame rate of ~50 fps.

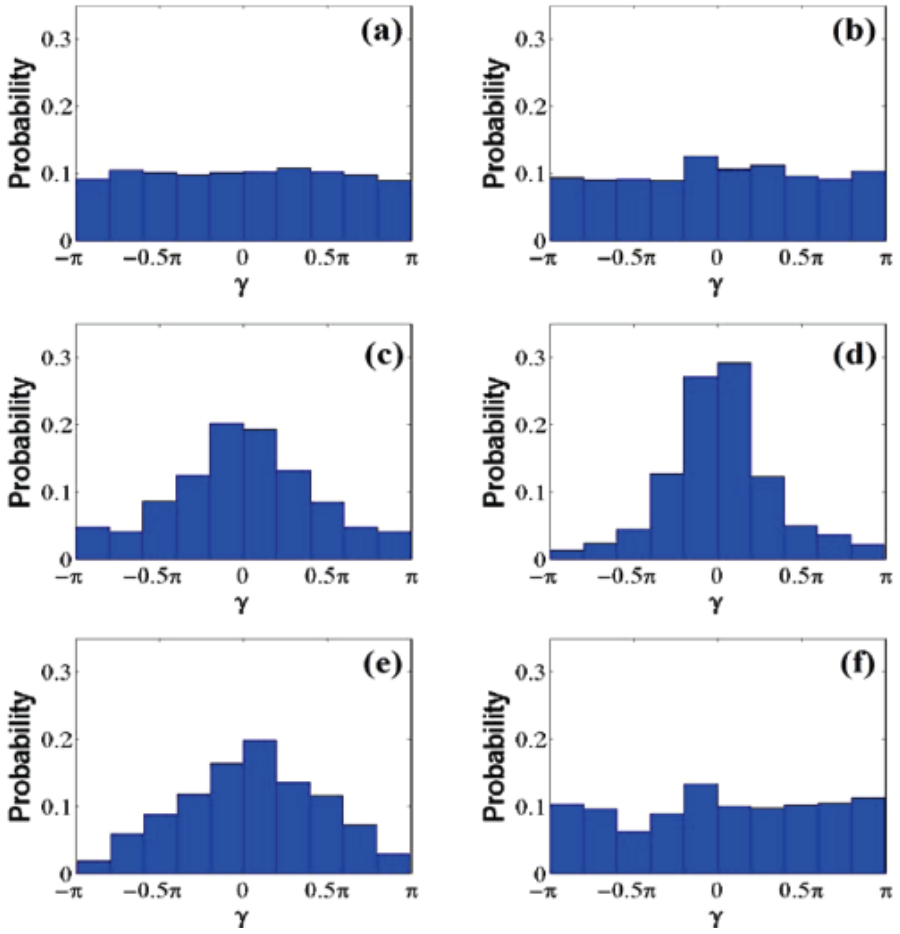

Figure 4-6. Distribution of directional angle γ for uncoated silica and half-coated Pt-silica particles in water and H_2O_2 solutions. (a) Silica particles in water; (b) half-coated Pt-silica particles in water; (c) half-coated Pt-silica particles in 15.0% w/w H_2O_2 solution; (d-f) half-coated Pt-silica particles in 27.3% w/w H_2O_2 solution.

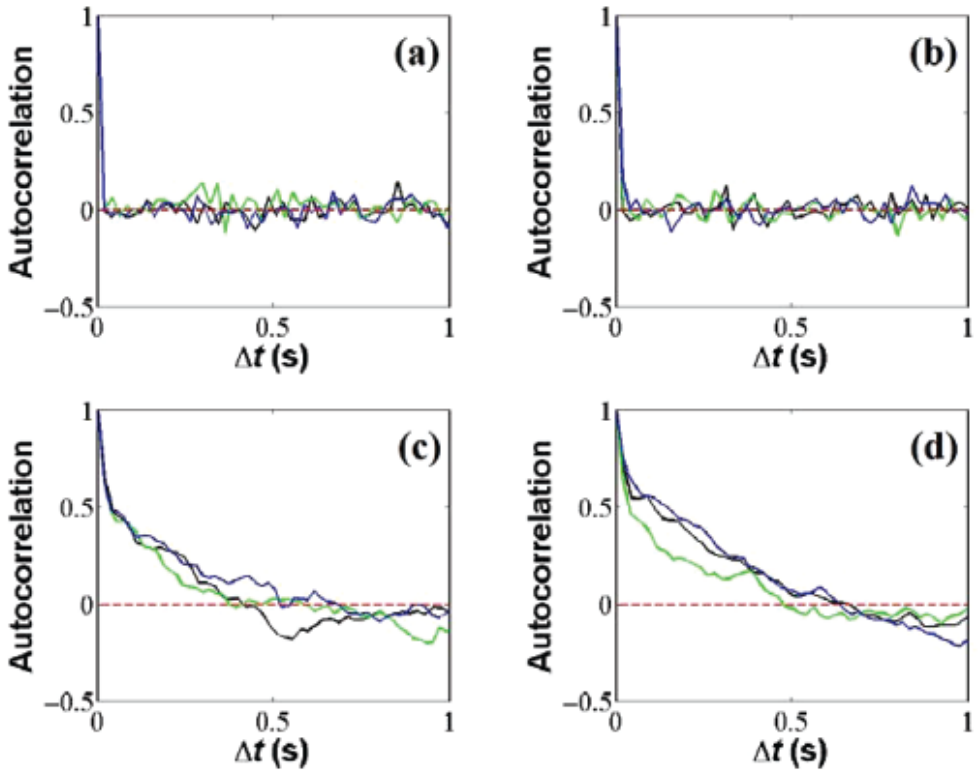

Figure 4-7. Normalized velocity autocorrelation function for uncoated silica and half-coated Pt-silica particles in water and H_2O_2 solutions. (a) Silica particles in water; (b) Pt-silica particles in water; (c) Pt-silica particles in 15.0% w/w H_2O_2 solution; (d) Pt-silica particles in 27.3% w/w H_2O_2 solution. In each case, the motion of three different particles is analyzed, as shown by the black, blue, and green curves.

The average speed of the three half-coated Pt-silica particles in water and in 15.0% and 27.3% H_2O_2 solutions is shown in Figure 4-8. The speed is determined by the distance traveled between image frames, which, in agreement with the studies of Howse et al.,[21] increases with increasing H_2O_2 concentration. The average speed of the uncoated silica particles in water is also shown for comparison, which is very close to the speed of the Pt-silica particles in water. Also plotted is the average time at which the velocity autocorrelation function falls to zero in each case. These values represent the approximate times when the particle velocities become uncorrelated, with the Pt-silica particles in H_2O_2 solutions showing significantly longer correlation times. The corresponding time for the uncoated silica particles in water is also shown, which is

essentially the same as the time for the Pt-silica particles in water. These correlation times are very close to zero.

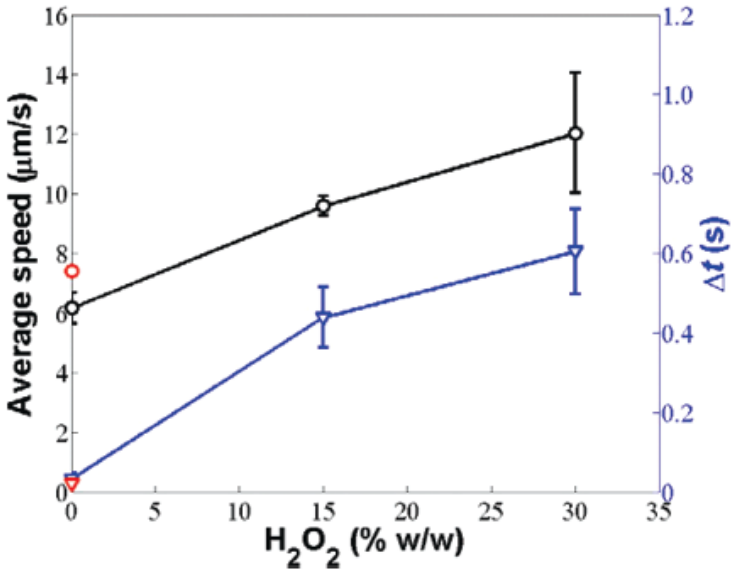

Figure 4-8. Average speed (○) of the three half-coated Pt-silica particles analyzed in Figure 4-7 and the average times in which the velocity autocorrelation function falls to zero (▽) in water, 15.0% w/w H_2O_2, and 27.3% w/w H_2O_2 solutions. The average speed of uncoated silica particles in water (○, red) and the average time that the corresponding autocorrelation function falls to zero (▽, red).

The interpretation of the directional angle and velocity autocorrelation analyses described above becomes more intuitive in terms of the high-speed video images. Figure 4-9 shows an overlay of images of a self-propelled Pt-silica particle in 10.0% H_2O_2 taken at a rate of ~56 fps. A lower H_2O_2 concentration was utilized in this experiment in order to capture Brownian-like motion in one frame area. The composite image shows that the particle typically travels in the same direction in the subsequent frame and continues in the same general direction for several more and sometimes many more frames. Large directional changes occur infrequently but give rise to major changes in the overall particle trajectory. This behavior is in agreement with the directional angle analysis shown in Figure 4-6. We also see that the particle velocity is correlated on short time scales, as shown in the analysis of the velocity autocorrelation function in Figure 4-7; however, on long time scales, the particle turns in wide angles and may travel in the

opposite direction. The loss of correlation at ~0.5 s described in Figures 4-7 and 4-8 can be seen in the composite image in Figure 4-9 over sequences of approximately 25-30 frames. In Figure 4-9, the image sequence was background corrected and enlarged before maximum projection. The light gray particle images represent the focal point of the transmitted light through the silica particle, excluding the Pt-coated region and dark edges as seen in Figure 4-3A, and thus appear slightly smaller than the 1 μm nominal bead size.

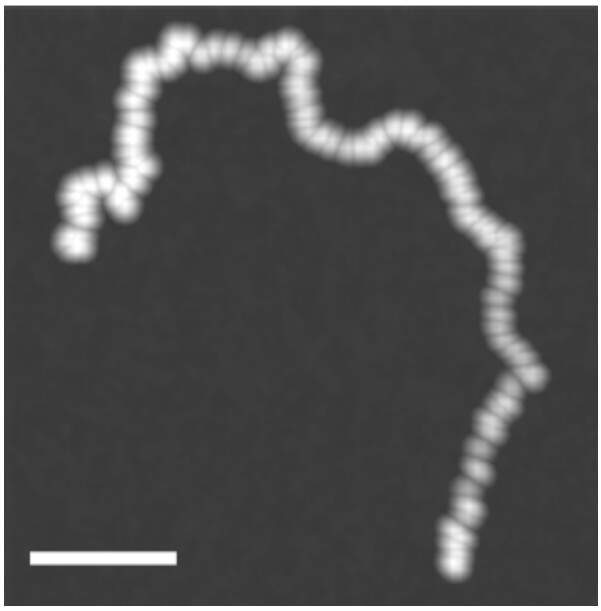

Figure 4-9. Maximum projection of 120 frames of a half-coated Pt-silica particle traveling in a 10.0% w/w H_2O_2 solution. The scale bar is 3 μm.

Suspensions of half-coated Pt-silica particles in H_2O_2 solutions are easily prepared and offer a convenient experimental system for studies of particle self-propulsion. Our study has utilized particles in which effectively two-dimensional motion is exhibited along the surface of a glass slide. While the overall particle speeds are no doubt affected by the frictional forces, this configuration allows an accurate characterization of correlations between the orientation axis of the particle and the direction of translational motion. The high extinction coefficient of the thin metal coating together with the illumination focusing by the uncoated silica allows the particle orientation to be continuously monitored during its self-propelled motion. With the location of the particle

determined frame to frame, the measurements permit a detailed analysis of the particle orientation and direction of motion.

Our measurements do not allow us to directly determine the "turning angle" of a particle, i.e., the change in direction that accompanies reorientation of the particle. Our measurements determine the particle position and orientation at each instant a video image is captured, and because directional changes may occur between the moments two successive image frames are captured, the measurements simply correlate the orientation of the particle with the direction of motion. The observation time interval also affects the value of the translational diffusion coefficient when the time scale of the observation is shorter than the characteristic rotational diffusion time.

The directional angle measurements shown in Figure 4-6 offer insights into the effect of the observation time interval on the apparent motion of the particle. The distributions of the directional angle γ for silica and Pt-silica particles in water and Pt-silica particles in 15.0% and 27.3% H_2O_2 solutions demonstrate that, with an observation time interval of $\Delta t \sim 0.02$ s, the self-propelled motion is highly directional compared to the Brownian motion. The particles in water display virtually no motion directionality, with an almost uniform distribution of the directional angle γ (Figure 4-6a, b). The motion directionality is random for this purely Brownian behavior. The distribution of the directional angle γ is distinctly different for the self-propelled particles in H_2O_2 solutions (Figure 4-6c, d), with the distribution becoming increasingly centered around small values of γ with increasing concentration. These distributions for the self-propelled particles indicate that the rotational diffusion time τ_R is larger than the observation time interval Δt. The directional angle distributions in Figure 4-6e,f become more uniform with increasing observation time interval Δt for the self-propelled particles. These distributions utilize the same data set for Pt-silica particles in 27.3% H_2O_2 solutions in Figure 4-6d, with measurements at ~55 fps. The image sequence was decimated by taking every 20th image for Figure 4-6e and every 40th image for Figure 4-6f. We see that the distribution of γ becomes less centered and, at the largest Δt, exhibits characteristics of Brownian motion with a relatively uniform distribution. Hence, with an observation time interval Δt that is about 40 times larger than that for observing Brownian motion of Pt-silica particles in water (Figure 4-6b) or propelled motion in H_2O_2

solutions (Figure 4-6d), the same particles exhibit Brownian-like motion in H_2O_2 solutions (Figure 4-6f).

An alternative approach to the mean-squared displacement for determining the translational diffusion constant D_{tran}[21] is to examine the step length distribution of a particle in the x and y directions for a given observation time interval Δt.[42] This approach allows us to take advantage of frame-to-frame measurements of the particle displacement to gain insights into the effect of Δt on the apparent motion of the particle. The probability density for a 1D displacement Δ is given by

$$P(\Delta) = A \exp(-\Delta^2/2\sigma^2) \qquad (1)$$

where $\sigma = (2D_{tran}\Delta t)^{1/2}$. The value of D_{tran} can therefore be determined by fitting eq 1 to a normal distribution of the step length Δ for a particular observation time interval Δt. We demonstrate with this approach that the self-propelled particles exhibit a Gaussian distribution of 1D step length over a wide range of the observation time interval Δt.

Figure 4-10 shows step length distributions for silica and Pt-silica particles in water and Pt-silica particles in 15.0% and 27.3% H_2O_2 solutions, with an observation time interval $\Delta t \approx 0.02$ s. The red curves show Gaussian fits for the four cases, with values of D_{tran} from Figure 4-10a-d of 0.42±0.04, 0.46±0.03, 0.60±0.06, and 0.66±0.04 $\mu m^2/s$, respectively. The dependence of the value of D_{tran} on the observation time interval Δt was investigated by developing new data sets from the data sets for Figure 4-10 according to $\Delta t_n = \Delta t(2n + 1)$ for n = 1, 2, 3, etc. The probability density for 1D displacements Δ was plotted for each data set corresponding to the incremented observation time interval. The Gaussian fits of these plots, similar to those in Figure 4-10, provide values of D_{tran} as a function of Δt.

The dependence of the translational diffusion constant D_{tran} on the observation time interval Δt is shown in Figure 11 for silica and Pt-silica particles in water and Pt-silica particles in 15.0% and 27.3% H_2O_2 solutions. We see in Figure 4-11a,b that the value of D_{tran} is independent of Δt for the purely Brownian motion of silica and Pt-silica particles in water. The least-squares fits of the values, shown by the red line, give similarly small values of D_{tran} for the particles in water (0.44 ± 0.04 and 0.68 ± 0.08 $\mu m^2/s$).[43] Figure 4-11c,d shows that the value of D_{tran} for Pt-silica particles is dependent

on the observation time interval for values of $\Delta t \leq 0.51$ s for 15.0% H_2O_2 solutions and $\Delta t \leq 0.62$ s for 27.3% H_2O_2 solutions. Above these values of Δt, the value of D_{tran} becomes independent of the observation time interval, much like the Brownian motion of the particles in water but with significantly larger D_{tran} values (3.57 ± 0.13 and 9.97 ± 0.20 $\mu m^2/s$).

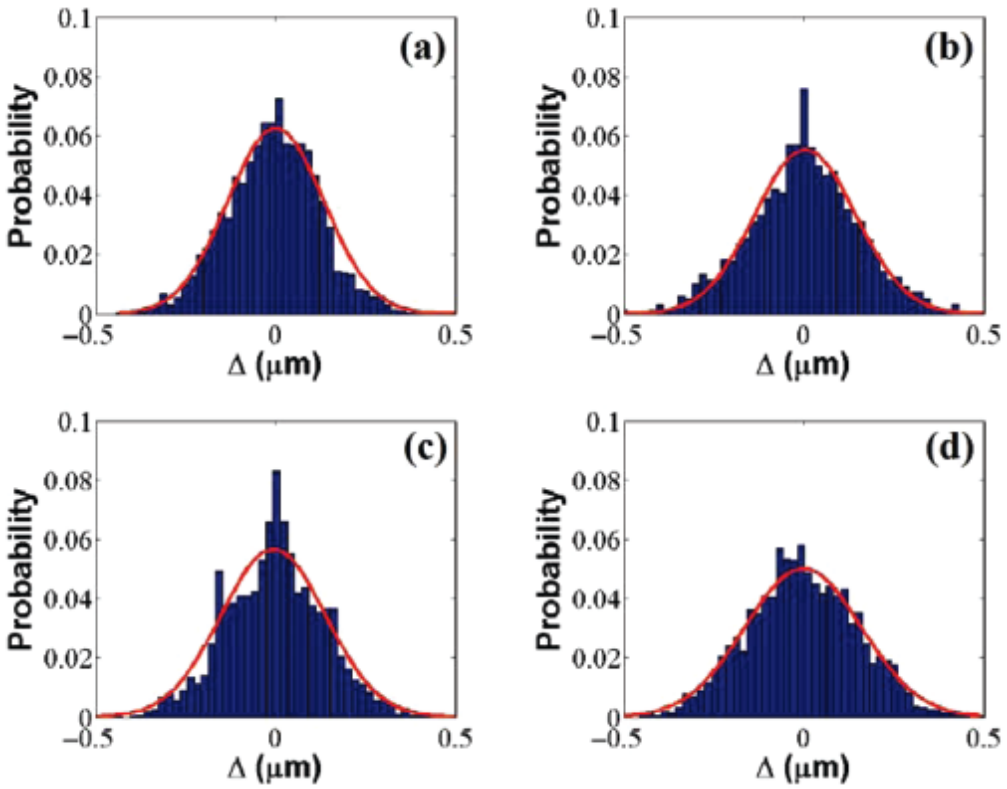

Figure 4-10. Distribution of the step length Δ for (a) silica and (b) Pt-silica particles in water and Pt-silica particles in (c) 15.0% w/w and (d) 27.3% w/w H_2O_2 solutions. The distributions are plotted for frame-to-frame step lengths in the *x* and *y* directions and normalized by dividing by the total number of steps (3000). The bar width is 0.02 μm in each distribution, and the observation time interval Δt = 0.021 (a), 0.022 (b), 0.018 (c), and 0.019 s (d). The Gaussian fit is shown by the red line, and the values of D_{tran} ($\mu m^2/s$) from each fit are (a) 0.42 ± 0.04, (b) 0.46 ± 0.03, (c) 0.60 ± 0.06, and (d) 0.66 ± 0.04.

Howse et al.[21] demonstrated that the motion of self-propelled particles can be characterized as directed propulsion for $\Delta t < \tau_R$, with an effective diffusion constant $D_{tran} = D + 1/4V^2\Delta t$, and Brownian-like for $\Delta t >> \tau_R$, with $D_{tran} = D + 1/4V^2\tau_R$, where V is the

particle speed arising from the propulsion. A transition in D_{tran} should therefore be observed as the observation time interval Δt is increased from below to above the rotational diffusion time τ_R. We see this crossover in behavior in Figure 4-11c,d, where the value of D_{tran} for the motion of Pt-silica particles in 15.0% and 27.3% H_2O_2 solutions is a linear function of Δt for $\Delta t <. \tau_R$ and is independent of Δt for $\Delta t >. \tau_R$. We can therefore estimate the value of τ_R as the point where D_{tran} plateaus to a constant value in each case. The value of τ_R increases only slightly, from ~0.51 to ~0.62 s, with increasing H_2O_2 concentration.

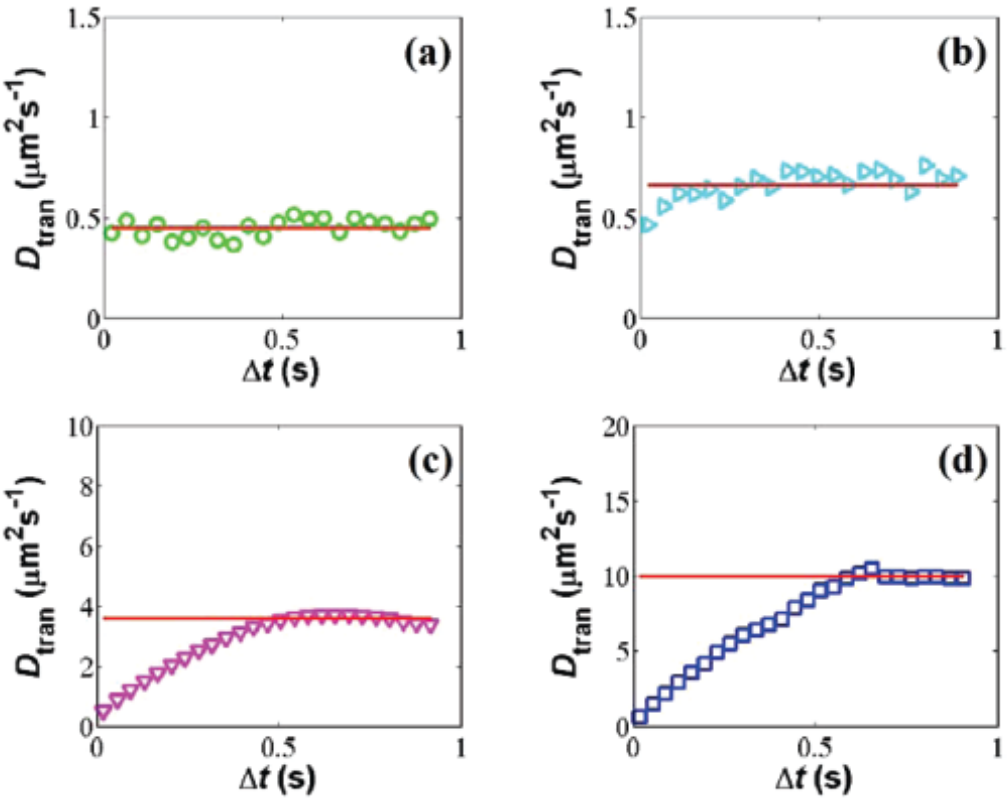

Figure 4-11. Translational diffusion coefficient D_{tran} as a function of the observation time interval Δt for (a) silica and (b) Pt-silica particles in water and Pt-silica particles in (c) 15.0% w/w and (d) 27.3% w/w H_2O_2 solutions. The red line in each plot represents the effective translational diffusion constant for Brownian motion. In (c) and (d), an approximate value of τ_R is given by the value of D_{tran} when it becomes constant, indicating the behavior is Brownian-like with $\Delta t \geq \tau_R$. The relative values of D_{tran} in each plot are given in Table 1.

TABLE 1: Values of D_{tran}, τ_R, and V from Step Length Probability Distribution

	D_{tran} ($\mu m^2/s$)	τ_R (s)	V (μm/s)
SiO_2/water	0.44 ± 0.04		
Pt-SiO_2/water	0.68 ± 0.08		
Pt-SiO_2/15.0% H_2O_2	3.57 ± 0.13	0.51	4.78
Pt-SiO_2/27.3% H_2O_2	9.97 ± 0.20	0.62	7.73

The values of D_{tran}, τ_R, and V obtained from the analysis of the 1D step length distribution in Figure 4-11 are listed in Table 1. The value of V can be calculated from the relation $D_{tran} = D + 1/4V^2\tau_R$, where D is the diffusion constant for purely Brownian motion of the Pt-silica particles in water. We see that the value of D_{tran} rises dramatically for the Pt-silica particles in H_2O_2 solutions compared to the value of D_{tran} for the particles in water, and that the value increases with increasing H_2O_2 concentration. The value of V also increases with increasing H_2O_2 concentration, while the value of τ_R changes only slightly. For comparison, the values of D_{tran}, τ_R, and V obtained from measurements of the mean-squared displacement are listed in Table 2.

TABLE 2: Values of D_{tran}, τ_R, and V from Mean-Squared Displacement

	D_{tran} ($\mu m^2/s$)	τ_R (s)	V (μm/s)
SiO_2/water	0.48 ± 0.01		
Pt-SiO_2/water	0.75 ± 0.03		
Pt-SiO_2/15.0% H_2O_2	5.48 ± 0.10	0.53	6.14
Pt-SiO_2/27.3% H_2O_2	9.80 ± 0.32	0.59	7.77

The analysis based on the step length probability distribution is consistent with the analyses of the velocity autocorrelation function and the directional angle distribution. We see in Figures 4-7 and 4-8 that the velocity correlation falls to zero at times that are roughly the same as the characteristic rotational diffusion time τ_R. Hence, at time intervals less than τ_R, velocities are correlated by the effects of directed propulsion, and at time intervals greater than τ_R, the correlations are lost due to rotational motion. The

directional angle distributions in Figure 4-6c-f also provide compelling evidence for the crossover from directed propulsion to Brownian-like behavior with increasing observation time interval. We see in Figure 4-6a,b that no directional preference is displayed in the directional angle distributions for silica and Pt-silica particles in water. Even though the observation time interval is smaller than the value of τ_R in this case, we do not expect to see any directional preference in purely Brownian motion, and we see in Figure 4-11a,b that the value of D_{tran} is independent of the observation time interval Δt. For the same observation time interval, however, we see in Figure 4-6c,d a strong directional preference of the Pt-silica particles in H_2O_2 solutions, characteristic of directed propulsion with $\Delta t \lesssim \tau_R$. As the value of Δt is increased in Figure 4-6e,f, we find the directional preference is diminished, and for $\Delta t \gtrsim \tau_R$, Brownian-like behavior is exhibited.

In summary, self-propelled Pt-silica particles in H_2O_2 solutions offer a convenient system for the characterization of chemically powered translational motion. We have found that the observation time scale may correspond to a regime of Brownian-like motion, where the observation occurs on a longer time scale than the rotational diffusion time, or to a regime of directed propulsion, where the observation occurs on a shorter time scale than the rotational diffusion time. This crossover in observed behavior with observation time interval allows important parameters to be determined, such as the rotational diffusion time τ_R, the effective translational diffusion coefficient D_{tran}, and the velocity derived from the chemical propulsion V. This system also offers the potential, in future experiments, for further exploration of factors influencing the motion of self-propelled particles, such as imposed temperature, concentration, or viscosity gradients. In addition, the system offers an opportunity to compare the features of non-biological chemical propulsion to those of self-propelled particles in living systems.

4.4 Directed Motion of Magnetic Janus Particles

The approach used to fabricate metallic Janus particles in our previous work is based upon the electron beam evaporation technique,[44] in which most metals including gold, platinum, nickel, and cobalt are commonly deposited either solely or in sequence. Magnetic materials can be decorated onto our Janus particles through e-beam evaporation

of nickel, followed by platinum (Figure 4-12). Nickel is also reported as a catalyst for the decomposition of H_2O_2, and, in the case of gold/nickel bimetallic nanorods, generated oxygen nanobubbles which caused their circular movements in solution of H_2O_2.[17] Our first experiment verifies that the nickel pellet at the millimeter scale produced bubbles at the pellet surface in 10% (v/v) H_2O_2, but at a much slower rate compared to the platinum pellet. Although there is no absolute correlation between metal surface at the macro (~mm) and micro scale (~μm), this pellet experiment provides a relative reaction rate between nickel and platinum.

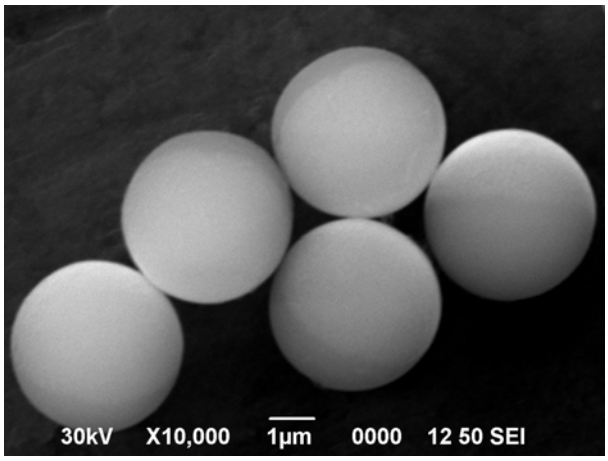

Figure 4-12. SEM image of 4 μm silica beads half-coated with 50 nm of nickel and 10 nm of platinum. The bright hemispheres represent the nickel and platinum coatings.

In concentrations of H_2O_2 solution up to ~30%, however, only random walk or very little directionality was observed for the 1 μm Ni-SiO_2 Janus particles. The 2D movement trajectory of 1 μm Ni-SiO_2 JPs in 27.3 % H_2O_2 at a frame rate of 45.6 fps (~ 250 frames) is shown in Figure 4-13A, in which the X and Y positions of the particle from each frame were extracted using Video Spot Tracker. All the directional angles were divided into ten equivalent bins from 0° to 180° and the probability for each bin was close to 0.10 (dash line), which indicated an even distribution of the directional angles, and thus, a random motion. γ was defined as instantaneous change in direction from frame to frame,[29] but without differentiating clockwise and counterclockwise changes (Figure 4-13B). This is presumably due to the slow decomposition of H_2O_2 at nickel, during which the generated force of motion was not enough to propel the beads. Another possibility is that oxidation of the nickel to nickel oxide might influence the catalytic

behavior. Native oxidation was found to occur on the nickel half shell, forming a thin layer of nickel oxide species.[44]

Our concept was to utilize platinum as the catalytic source and nickel as the magnetic handle. Platinum not only acts as the catalytic source of the autonomous motion, but protects the nickel from oxidation. Thus, the resulting Janus particles can propel themselves in solutions of H_2O_2 and their motion can be steered using an external magnetic field.

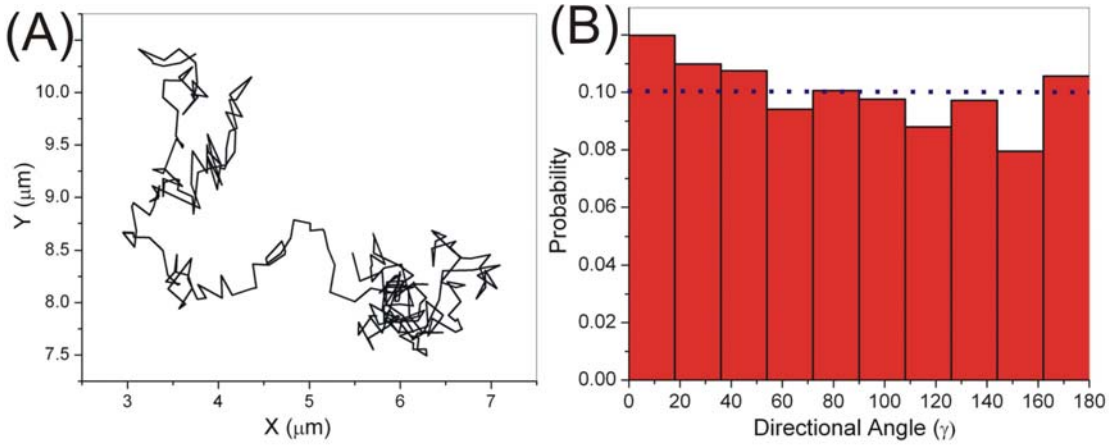

Figure 4-13. (A) 2D movement trajectory of 1 μm Ni-SiO_2 JPs in 27.3 % H_2O_2 at a frame rate of 45.6 fps (~ 250 frames). (B) Distribution of directional angle, γ, at the same frame rate (~2500 frames analyzed).

Though the curved surface of the Janus particle makes investigation of the bimetallic film difficult by XPS, AFM, or even SEM, we have investigated the oxidation of small bimetallic structures of Pt/Ni on a silica surface. The Pt/Ni features were produced during preparation of the Pt/Ni-SiO_2 JPs through the nanosphere lithography (NSL) process. Oxidation of the underlying nickel in the Pt/Ni nanostructures on the NSL substrate was observed through AFM. As shown in Figure 4-14, the Pt-"protected" nickel appeared swollen after being exposed to air for days. The oxidation was visualized as volume expansion, starting from the edge of the pseudo-trigonal prism structures (Figure 4-14B). The partial native oxidation of nickel occurred from where nickel was not fully covered by platinum, and therefore, the protection from oxidation was not effective in this particular case when the coatings were not continuous.[45] Nevertheless, the

combination of nickel and platinum resulted in new Janus particles with a dual magnetic and catalytic functionality.

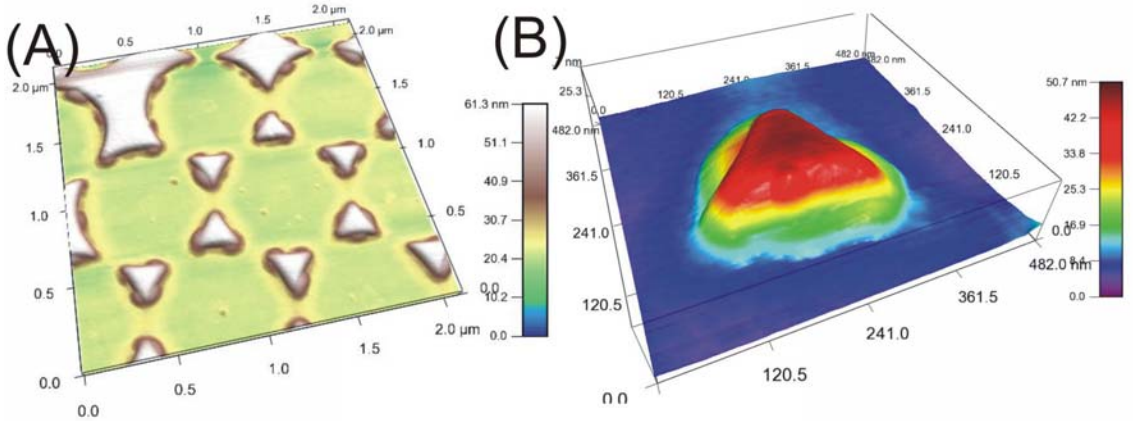

Figure 4-14. AFM of a NSL substrate after exposure in air, composed of pseudo-trigonal prism structures (A and magnified B) with 30 nm of Ni covered by 10 nm of Pt.

The magnetic behavior of the Pt/Ni-SiO_2 JPs is believed to be similar to the magnetic thin films. Due to the geometrical asymmetry (a much shorter length scale along the z direction), thin film has a magnetic anisotropy (shape anisotropy), that is, the magnetization along the in-plane direction (easy axis) is more energetically favorable than along the out-of-plane direction.[46] To illustrate this, let us take a thin film (on a flat substrate) with a dimension of 0.5 cm × 0.5 cm × 20 nm as an example. When the thin film surface normal is perpendicular to the applied field (in-plane direction), the magnetization reaches the maximum value (Figure 4-15A). In turn, when the thin film surface normal is parallel to the applied field (out-of-plane direction), the magnetization reaches the minimum value (Figure 4-15B). This produces an easy axis of magnetization along the in-plane direction in the absence of magnetic field.

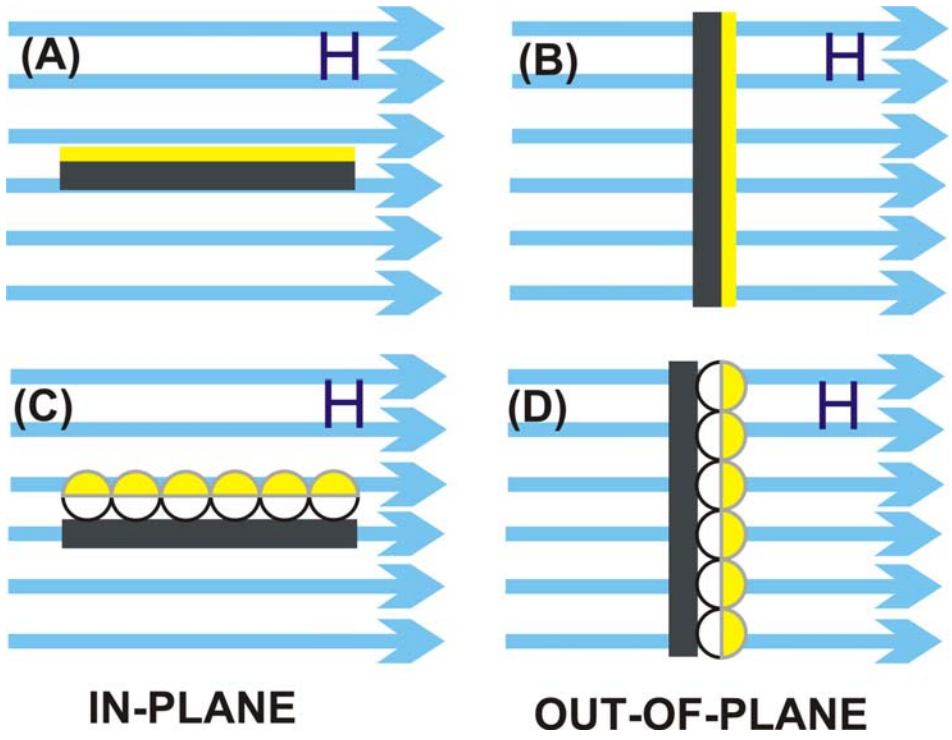

Figure 4-15. Schematic illustration of metal thin film coatings (yellow) on a flat substrate (black) and on particles (white) in the presence of external magnetic field (***H***, blue arrows).

Similarly, the magnetic JP array on flat substrate has those two corresponding positions relative to the applied field (Figure 4-15C,D). However, the metal coating on a spherical surface is not flat with increasing angles relative to the substrate plane from the pole position to the equator, leading to a non-uniform coating along the surface with maximal thickness at pole position and minimal thickness at equator.[47] For each individual Janus particle, the metal half shell has a longer dimension in the equatorial plane than in the axial plane, especially when the shell is very thin (20-50 nm in our cases), and thus, a greater contribution to the magnetization (Figure 4-16). Provided that the substrate dimension remains constant, the directional magnetization of the curved magnetic metal coating is expected to be similar to that of the flat thin film – maximum at in-plane direction and minimum at out-of-plane direction. Moreover, the magnetization maximum and minimum of magnetic JP array should fall in between those two extremes of thin film due to the curvature.

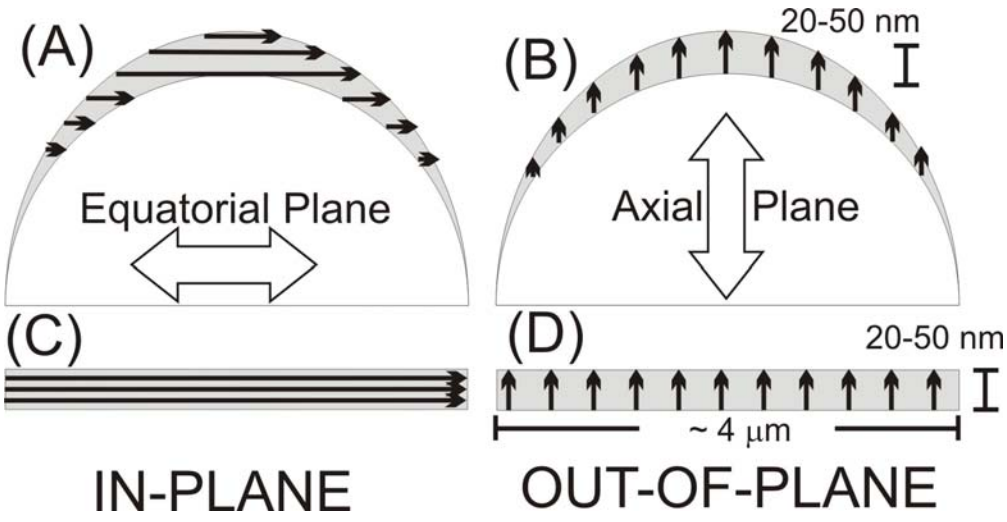

Figure 4-16. Schematic illustration of magnetic anisotropy of magnetic Janus particle (A, B) and metal thin film (C, D).

The angular dependence of the magnetization of Janus particle samples was studied for 1 μm magnetic JP coated with 20 nm of nickel. As shown in Figure 4-17A, the hysteresis cycles changed from a thin half-lying "parallelogram" to a fat standing-up "parallelogram" as the angle rotated from the out-of-plane position (90°) to the in-plane position (0°). The change in shape was accompanied with the change in the magnetization. The remnant magnetization (M_r, magnetization at zero field) exhibited a consistent increase as the substrate was rotated from out-of-plane to in-plane orientation (Figure 4-17B). The simplest explanation is that the dominant magnetic moment (easy axis) of each individual magnetic JP, and therefore, of the magnetic JP array, lay along the equatorial direction, instead of the axial direction. Other preliminary data showed that the M_r decreased as the thickness of nickel decreases. But only subtle changes were observed in the magnetic moments before and after (partial) oxidation and with/out Pt coating.

To validate this observation, a two dimensional simulation of a silica particle with a half-shell of nickel in an external magnetic field was carried out in the COMSOL multiphysics modeling and simulation software (Figure 4-18). This model does not exactly duplicate the actual system, since the nickel film is of uniform thickness on the coated hemisphere, but will provide data for comparison. The simulation was carried out, and the magnetization was summed over the total magnetic shell domain. Along the

equatorial direction, the magnetic domain (the half metal shell) required an energy of 1.06×10^{-16} A/m for magnetization, which was approximately two orders of magnitude lower than that along the axial direction (2.28×10^{-14} A/m). Therefore, the individual magnetic JP would be expected to show a preferred orientation for magnetization along the equatorial direction in the external magnetic field.

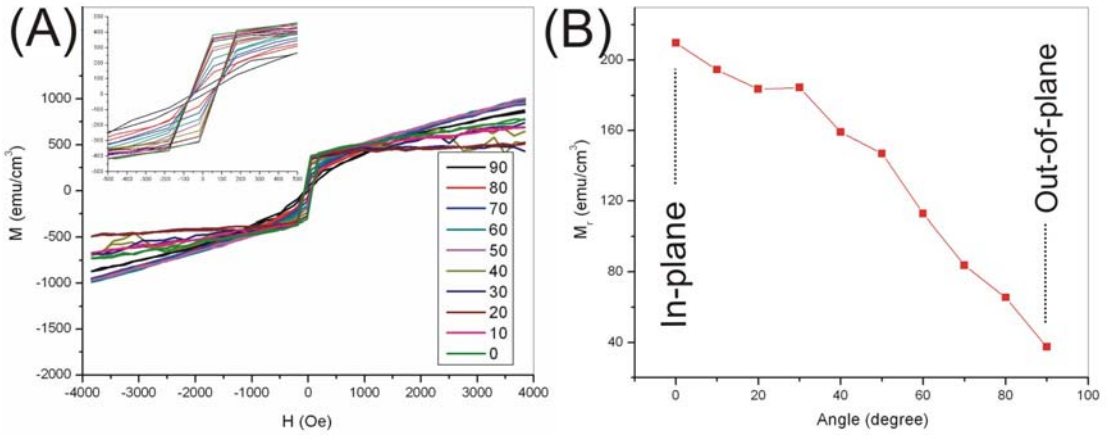

Figure 4-17. (A) Angle-dependent magnetization of 1um magnetic JPs with 20 nm of Ni (insert: magnified hysteresis cycles). (B) Angle-dependent remnant magnetization of 1 μm magnetic JPs with 20 nm of Ni.

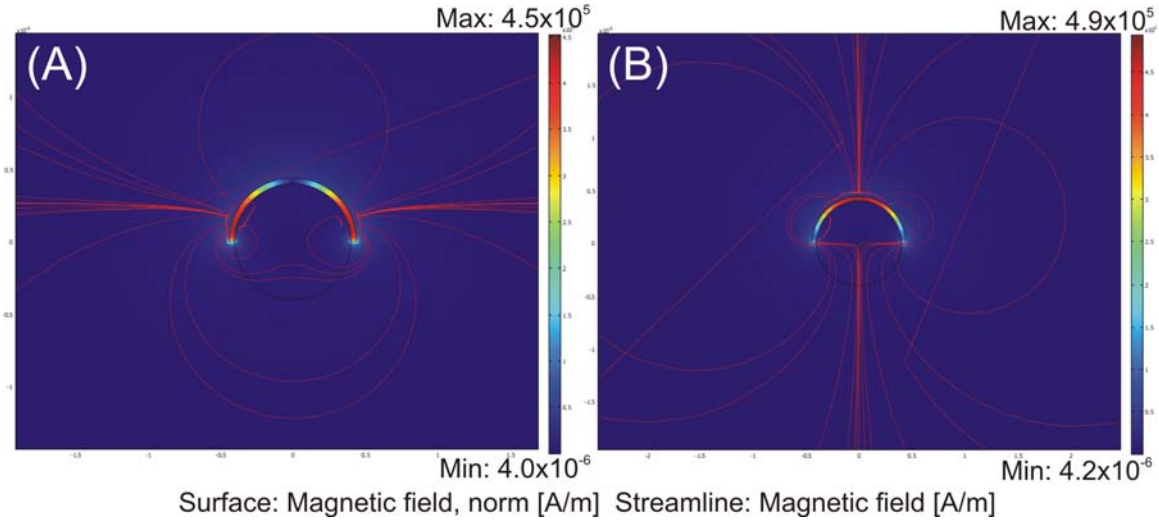

Figure 4-18. Simulated magnetization energy of nickel half shell in COMSOL in the horizontal (A) and vertical magnetic field (B).

In solution, the individual magnetic Janus particles responded freely to the external magnetic field, and oriented with the equatorial plane along the direction of the

applied field. The magnetic force brought the magnetic Janus particles in contact, forming staggered chain structures, the direction of which was also the same as that of the applied field (Figure 4-19). The chains appeared parallel to each other due to the propulsion. Close observation revealed that the magnetic Janus particles in a typical chain connected with their magnetic coatings in the central lane and the silica hemispheres facing to the sides alternatively.[46] The formation of such a chain structure is fully consistent with the magnetization measurements and the simulation.

The motion experiments were performed using magnetic JPs composed of 4 μm silica beads coated in sequence with 50 nm of nickel and 10 nm of platinum suspended in 15.0% w/w H_2O_2. A pair of permanent magnets was used to direct the motion of the magnetic JPs. As discussed previously, the magnetic JPs tended to aggregate, forming staggered chain structures at high concentrations (Figure 4-19). The bead solution was therefore highly diluted to avoid the possible interaction between any two magnetic JPs. Figure 4-20 exhibits the movement trajectory of one Pt/Ni-SiO_2 magnetic JP. The magnetic JPs underwent directed motion mostly with direction perpendicular to the external magnetic field. The orientation of magnetic JPs was clearly observed with their equatorial planes aligned along the applied field, and quickly responded to the directional change of the applied field. The magnetic JPs changed their moving direction in response to the applied field and then continued to move in a controlled direction. The magnetic JPs completed the pre-determined pathways by changing the direction of the magnetic field once (Figure 4-20). The left side of the trajectory curve (before turning the applied field) and the right side (after turning the applied field) were both fitted linearly with R = 0.99, indicating that the applied field only served to orient the particle, not influenced the speed.

The average speed of the magnetic JPs in 15% H_2O_2 is determined by the total distance traveled between any two consecutive image frames and the frame rate. At the frame rate of ~15.8 fps (observation time interval 0.064 s), the average speed was measured as 2.74±1.52 μm/s, which appeared to be small compared to the 1 μm JPs in the absence of magnetic field.[29] This is possibly due to the use of larger and heavier Janus particles with thicker metal coatings and the slower frame rate as well.

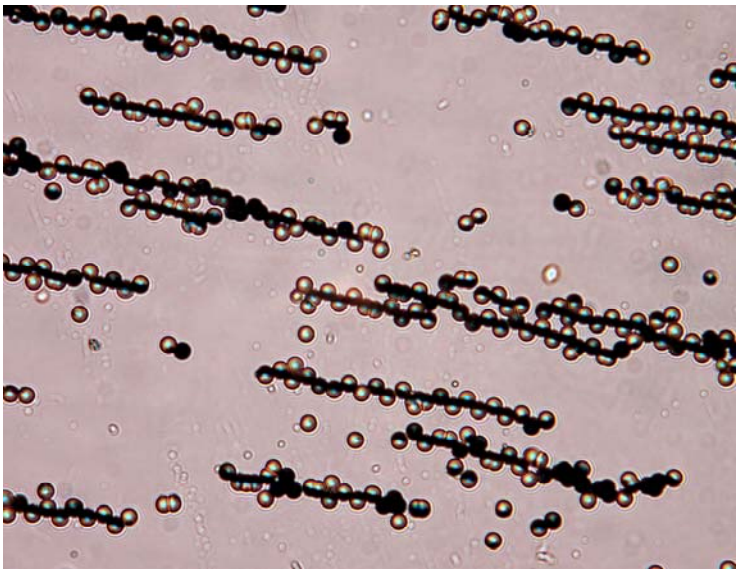

Figure 4-19. Transmission optical image of staggered chain structures of 4 μm magnetic JPs aligned along the external magnetic field parallel to the substrate surface.

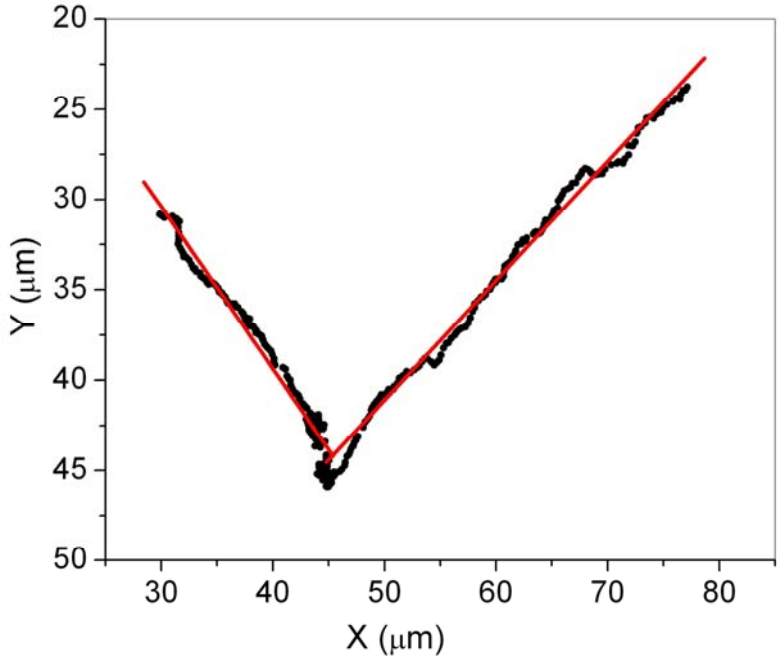

Figure 4-20. 2D movement trajectory (black) of a magnetic JP, Pt/Ni-SiO_2, in a solution of 15% H_2O_2, fitted with linear equations with R = ~0.99 (Red).

The direction of motion was analyzed by characterizing the distribution of directional angle, γ.[29] A Brownian particle should show little preference for direction relative to its previous motion (similar to Figure 4-13B with a probability of ~0.10 for

each bin). As shown in Figure 4-21 (blue bins), a rapid decay of the distribution probability can be observed from 0° (no deviation - particle moving forward) to 180° (particle completely moving backward relative to previous frames) according to the directional angle. The probability (~0.33) of continuing to travel in nearly the same direction is approximately 30% higher than what was observed for the JPs without the external magnetic field (red bins). Considering the issues of size and density of the particles, such a distinct directional preference for the magnetic JPs further confirmed that the applied field played a strong directed influence on the self-propelled motion.

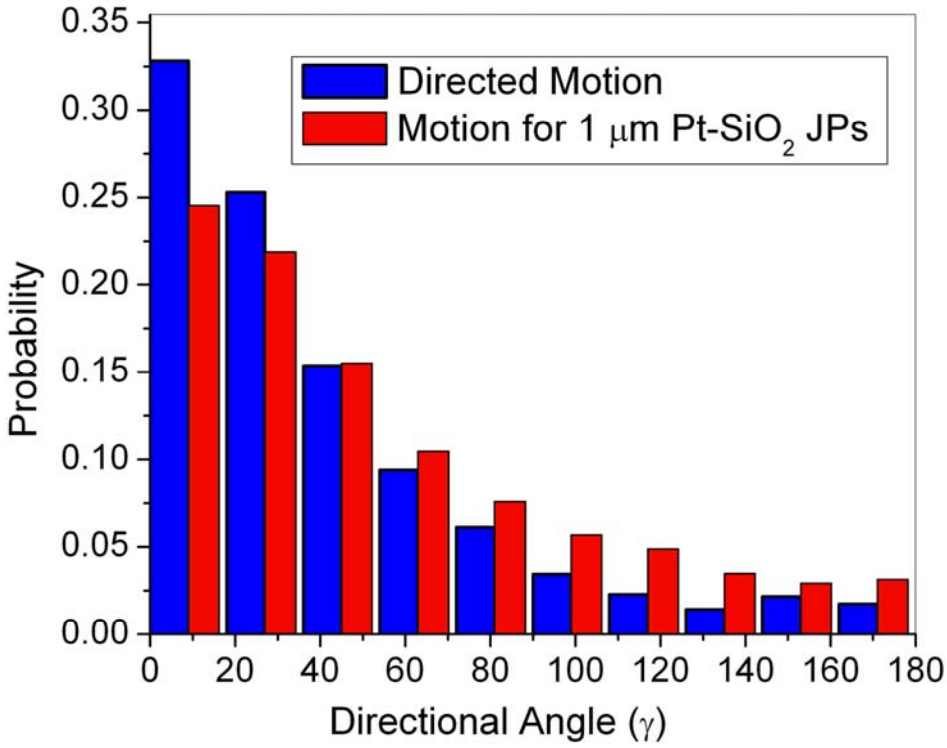

Figure 4-21. Distribution of directional angle, γ, for motion of 4 μm magnetic Pt/Ni-SiO_2 JPs in the presence of magnetic field (blue bins: 15% H_2O_2, 15.8 fps). The directional angle distribution for motion of 1 μm Pt-SiO_2 JPs (red bins: 15% H_2O_2, 18.4 fps) in the absence of magnetic field is shown for comparison.

In summary, this section demonstrated control over the direction of particle self-propulsion using the external magnetic field. The magnetic JPs can be steered with a high degree of precision to undergo motion in an arbitrary pathway. However, a complete control over the self-propelled motion has to overcome the Brownian effect, which is

ubiquitous to all the colloidal motion systems. This will become more difficult as particle vehicle size decreases. The direction of motion of the magnetic JPs may be better modulated through using automated rotational magnetic field generation, rather than mechanical rotation. The optical transmission mode clearly differentiated the metal coated hemisphere from the silica hemisphere, and we anticipate that this advantage will allow detailed analysis of the mechanism of the propelled motion.

References and Notes

(1) Cameron, L. A.; Footer, M. J.; van Oudenaarden, A.; Theriot, J. A. *Proc. Natl. Acad. Sci. U.S.A.* **1999**, *96*, 4908-4913.

(2) Pantaloni, D.; Le Clainche, C.; Carlier, M.-F. *Science* **2001**, *292*, 1502-1506.

(3) Bernheim-Groswasser, A.; Wiesner, S.; Golsteyn, R. M.; Carlier, M.-F.; Sykes, C. *Nature* **2002**, *417*, 308-311.

(4) Paxton, W. F.; Kistler, K. C.; Olmeda, C. C.; Sen, A.; St. Angelo, S. K.; Cao, Y.; Mallouk, T. E.; Lammert, P. E.; Crespi, V. H. *J. Am. Chem. Soc.* **2004**, *126*, 13424-13431.

(5) Ismagilov, R. F.; Schwartz, A.; Bowden, N.; Whitesides, G. M. *Angew. Chem., Int. Ed.* **2002**, *41*, 652-654.

(6) Paxton, W. F.; Sen, A.; Mallouk, T. E. *Chem. Eur. J.* **2005**, *11*, 6462-6470.

(7) Wang, Y.; Hernandez, R. M.; Bartlett, D. J.; Bingham, J. M.; Kline, T. R.; Sen, A.; Mallouk, T. E. *Langmuir* **2006**, *22*, 10451-10456.

(8) Kline, T. R.; Paxton, W. F.; Mallouk, T. E.; Sen, A. *Angew. Chem., Int. Ed.* **2005**, *44*, 744-746.

(9) Catchmark, J. M.; Subramanian, S.; Sen, A. *Small* **2005**, *1*, 202-206.

(10) Dhar, P.; Fischer, T. M.; Wang, Y.; Mallouk, T. E.; Paxton, W. F.; Sen, A. *Nano Lett.* **2006**, *6*, 66-72.

(11) Paxton, W. F.; Sundararajan, S.; Mallouk, T. E.; Sen, A. *Angew. Chem., Int. Ed.* **2006**, *45*, 5420-5429.

(12) Kline, T. R.; Tian, M.; Wang, J.; Sen, A.; Chan, M. W. H.; Mallouk, T. E. *Inorg. Chem.* **2006**, *45*, 7555-7565.

(13) Paxton, W. F.; Baker, P. T.; Kline, T. R.; Wang, Y.; Mallouk, T. E.; Sen, A. *J. Am. Chem. Soc.* **2006**, *128*, 14881-14888.

(14) Dhar, P.; Cao, Y. Y.; Kline, T.; Pal, P.; Swayne, C.; Fischer, T. M.; Miller, B.; Mallouk, T. E.; Sen, A.; Johansen, T. H. *J. Phys. Chem. C* **2007**, *111*, 3607-3613.

(15) Ibele, M. E.; Wang, Y.; Kline, T. R.; Mallouk, T. E.; Sen, A. *J. Am. Chem. Soc.* **2007**, *129*, 7762-7763.

(16) Ozin, G. A.; Manners, I.; Fournier-Bidoz, S.; Arsenault, A. *Ad*v. *Mater.* **2005**, *17*, 3011-3018.

(17) Fournier-Bidoz, S.; Arsenault, A. C.; Manners, I.; Ozin, G. A. *Chem. Commun.* **2005**, 441-443.

(18) Valadares, L.; Tao, Y.-G.; Zacharia, N. S.; Kitaev, V.; Galembeck, F.; Kapral, R.; Ozin, G. A. *Small* **2010**, *6*, 565-572.

(19) Hong, Y.; Blackman, N. M. K.; Kopp, N. D.; Sen, A.; Velegol, D. *Phys. Re*v. *Lett.* **2007**, *99*, 178103.

(20) Kline, T. R.; Iwata, J.; Lammert, P. E.; Mallouk, T. E.; Sen, A.; Velegol, D. *J. Phys. Chem. B* **2006**, *110*, 24513-24521.

(21) Howse, J. R.; Jones, R. A. L.; Ryan, A. J.; Gough, T.; Vafabakhsh, R.; Golestanian, R. *Phys. Re*v. *Lett.* **2007**, *99*, 048102.

(22) Golestanian, R.; Liverpool, T. B.; Ajdari, A. *Phys. Re*v. *Lett.* **2005**, *94*, 220801.

(23) Golestanian, R.; Liverpool, T. B.; Ajdari, A. *New J. Phys.* **2007**, *9*, 126-128.

(24) Ruckner, G.; Kapral, R. *Phys. Rev. Lett.* **2007**, *98*, 150603.

(25) Wang, J.; Manesh, K. M., *Small* **2010**, 6, 338-345.

(26) Demirok, U. K.; Laocharoensuk, R.; Manesh, K. M.; Wang, J., *Angew. Chem. Int. Ed.* **2008**, 47, 9349-9351.

(27) Laocharoensuk, R.; Burdick, J.; Wang, J., *ACS Nano* **2008**, 2, 1069-1075.

(28) Mirkovic, T.; Zacharia, N. S.; Scholes, G. D.; Ozin, G. A., *ACS Nano* **2010**, 4, 1782-1789.

(29) Ke, H.; Ye, S.; Carroll, R. L.; Showalter, K., *J. Phys. Chem. A* **2010**, 114, 5462-5467.

(30) Velev, O. D.; Bhatt, K. H., *Soft Matter* **2006**, 2, 738-750.

(31) Gangwal, S.; Cayre, O. J.; Velev, O. D., *Langmuir* **2008**, 24, 13312-13320.

(32) Kline, T. R.; Paxton, W. F.; Mallouk, T. E.; Sen, A., *Angew. Chem. Int. Ed.* **2005**, 44, 744-746.

(33) Burdick, J.; Laocharoensuk, R.; Wheat, P. M.; Posner, J. D.; Wang, J., *J. Am. Chem. Soc.* **2008**, 130, 8164-8165.

(34) Chaturvedi, N.; Hong, Y.; Sen, A.; Velegol, D., *Langmuir* **2010**, 26, 6308-6313.

(35) Hong, Y.; Diaz, M.; Córdova-Figueroa, U. M.; Sen, A., *Adv. Funct. Mater.* **2010**, 20, 1568-1576.

(36) Ibele, M.; Mallouk, T. E.; Sen, A., *Angew. Chem. Int. Ed.* **2009**, 48, 3308-3312.

(37) Balasubramanian, S.; Kagan, D.; Manesh, K. M.; Calvo-Marzal, P.; Flechsig, G.-U.; Wang, J., *Small* **2009**, 5, 1569-1574.

(38) Jiang, H.-R.; Yoshinaga, N.; Sano, M., *Phys. Rev. Lett.* **2010**, 105, 268302.

(39) Sundararajan, S.; Lammert, P. E.; Zudans, A. W.; Crespi, V. H.; Sen, A., *Nano Lett.* **2008**, 8, 1271-1276.

(40) Rasband, W. S. ImageJ, U.S. National Institutes of Health, Bethesda, MD, 1997-2008, http://rsb.info.nih.gov/ij/.

(41) CISMM at University of North Carolina at Chapel Hill, supported by the NIH NIBIB (NIH 5-P41-RR02170).

(42) Nakroshis, P.; Amoroso, M.; Legere, J.; Smith, C. *Am. J. Phys.* **2003**, *71*, 568-573.

(43) The values of D_{tran} may differ because the Pt-silica particles in water have the Pt-coated region oriented toward the glass surface, presumably due to the higher density of the Pt-coated region of the particle. In all experiments on self-propelled Pt-silica particles in H_2O_2 solutions, the symmetry axis of the particle is generally oriented parallel to the glass surface, with the uncoated silica region oriented toward the direction of travel.

(44) Ye, S.; Carroll, R. L., *ACS Appl. Mater. Interfaces* **2010**, 2, 616-620.

(45) Oxidation on the NSL Substrate. The oxidation details on the NSL substrate and the effect on the optical property of the resulting structure have been investigated and will be published elsewhere.

(46) Smoukov, S. K.; Gangwal, S.; Marquez, M.; Velev, O. D., *Soft Matter* **2009**, 5, 1285-1292.

(47) Ye, S.; Routzahn, A. L.; Carroll, R. L., *Langmuir* **2011**, 27, 13806-13812.

Chapter 5

Directed Assembly of Functionalized Janus Particles at Interfaces and Through Magnetic Fields

5.1 Background

Anisotropic particles have recently attracted significant attention due to their unique surface properties and diverse potential applications.[1,2] Assembly of anisotropic colloidal structures produces two or three dimensional superstructures with applications in photonics, electronics, or sensing.[3-5] Previous works have shown that assembly of Janus Particles (JPs) through the use of external magnetic or electric field creates chain structures.[6-8] Current research focuses on more complex structures through novel anisotropic building blocks. The metal half-coated Janus particles are functionalized to become hydrophobic on one side and hydrophilic on the other. The assembly of these functionalized Janus particles is confined at the interfaces of water/air and water/oil. The orientation of the Janus particle monolayer may be controlled through the use of variety of oil phases. The direct transfer of "face-down configuration" onto a solid substrate is demonstrated, which enables a better way to prepare bimetallic Janus particles. The patterns of chain structures formed by the magnetic JPs through directed self-assembly are expected to lead to complex soft materials allowing for potential applications in photonic devices. The magnetic Janus particles respond to the applied field and form chain structures, along the direction of magnetic field parallel to the substrate surface, from various concentrations of particle solution. These staggered structures can be retained both in solution and under dry condition. In the presence of magnetic field perpendicular to the substrate surface, the magnetic JPs form short chains, typically doublets, due to the confinement of the cell dimension which holds the sample solution.

5.2 Experimental

5.2.1 Preparation of Alkanethiol Functionalized Janus Particles (Au/Ni-SiO_2).

A typical method to prepare (thiolated) metallic Janus particles is described below (Figure 5-1). A predominately close-packed monolayer of colloidal silica particles (Bangs Laboratories, Inc) with a diameter of 4 μm was assembled on a clean, flat substrate. Nickel (100 nm) and gold (80 nm) were then deposited sequentially through e-beam evaporation (Temescal BJD-2000) onto the silica bead substrate. The resulting metal half-coated Janus particles, denoted as Au/Ni-SiO_2 JPs, were dispersed into water using ultrasonication. The chemisorption of alkanethiol on the metallic Janus particles

(denoted as thiolated Au/Ni-SiO_2 JPs) was carried out through immersion of the substrate of Au/Ni-SiO_2 JPs into dodecanethiol for 15 min,[9] forming a self-assembled monolayer (SAM) on the gold caps, followed by rinsing with ethanol. Digital camera, optical microscope (Olympus BX51), and FE-SEM (JEOL 7600F) were used to characterize the formed Janus particles and their assembled structures.

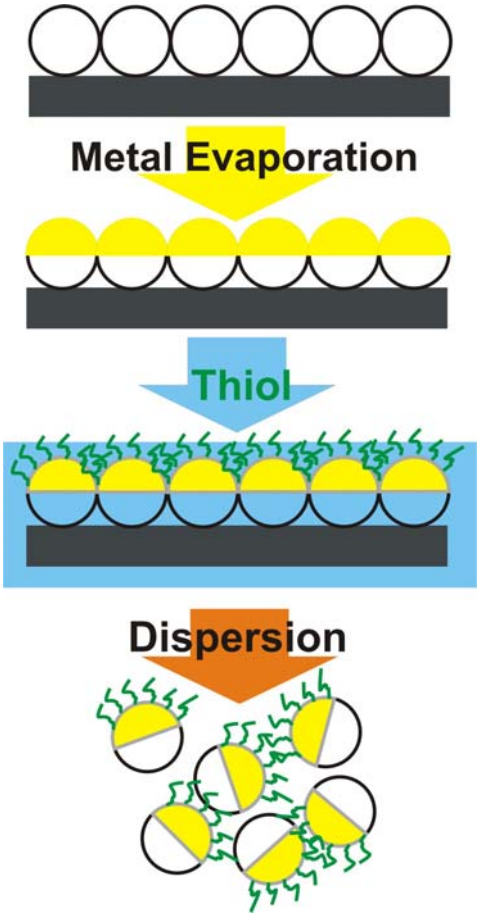

Figure 5-1. An approach to fabricate (thiolated) metallic Janus particles.

5.2.2 Directed Assembly of Magnetic JPs in the Presence of Magnetic Field.

A pair of permanent magnets was applied across the sample substrate on an optical microscope (Olympus BX51). The direction of external magnetic filed is, in one case, parallel to the substrate surface. In the case when the external magnetic field is perpendicular to the substrate surface, only one permanent magnet is used, which is placed underneath the microscope stage. A digital camera (Canon EOS REBEL T1i) fitted to the microscope is used to capture the optical images of the assembled structures.

5.3 Janus Particles at Interfaces

5.3.1 Au/Ni-SiO_2 JPs in water

The Au/Ni-SiO_2 JPs were easily removed from the substrate and dispersed into water using ultrasonication. Due to large bead size and high density, the metal half-coated JPs sedimentated quickly within a few tens of seconds. The JPs were re-dispersible into water using ultrasonication after sedimentation. Drying the JPs on a flat glass substrate showed no preferred orientation with regard to the glass. As shown in Figure 5-2, the Au/Ni-SiO_2 JPs self-assembled to form a loosely packed monolayer with mixed orientations on a glass coverslip. Several representative orientations - "new moon", "crescent", "half moon", "gibbous" - are depicted in Figure 5-2B.

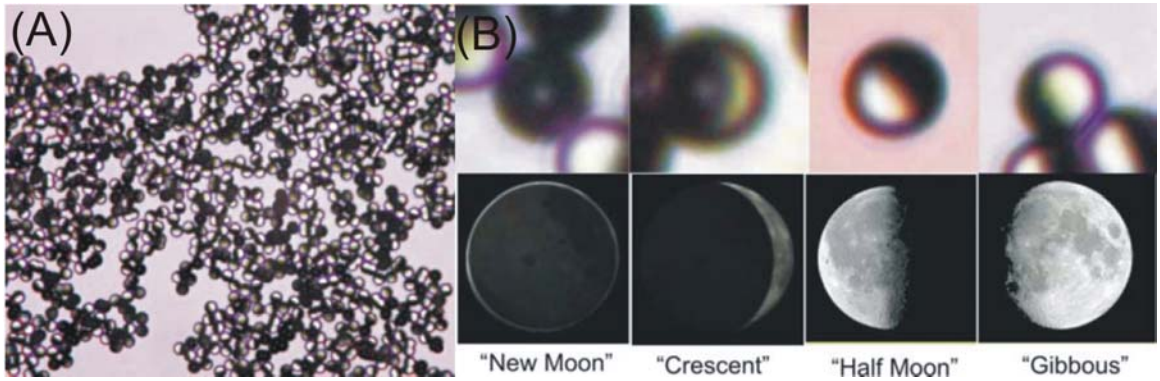

Figure 5-2. (A) Transmitted optical image of Au/Ni-SiO_2 JPs dried from an aqueous solution on a coverslip; (B) orientations of individual Au/Ni-SiO_2 JPs - "new moon", "crescent", "half moon", and "gibbous", analogous to the lunar phase[10]

5.3.2 Thiolated Au/Ni-SiO_2 JPs at interface

(1) Thiolated Au/Ni-SiO_2 JPs at water/air interface

The thiolated Au/Ni-SiO_2 JPs assembled as a loosely packed monolayer, floating at the water/air interface with the thiolated metal caps pointing up to atmosphere (Figure 5-3).[11] The hydrocarbon ligand-covered gold hemispheres are considered hydrophobic (or nonpolar) whereas the silica hemispheres are typically polar due to Si-O-Si and Si-OH functionalities. In contrast to bare silica particles exhibiting complete dispersion into water implying uniform wetting, the resulting thiolated JPs have two distinct surface regions exhibiting differing wettability. In consequence, their interfacial activity was

significantly increased due to the Janus character (anisotropy), and the thiolated JPs assembled and oriented preferentially at the water/air interface. Optical and SEM imaging reveals that the JPs retained orientation ("face-up" configuration) after drying of the suspension on a coverslip (Figure 5-4).

(2) Thiolated Au/Ni-SiO_2 JPs at water/oil interface

Similar to the water/air interface, the self-assembly of the thiolated Au/Ni-SiO_2 JPs was confined at the water/hexane interface with the gold caps facing up to the nonpolar phase ("face-up" configuration; hexane has lower density than water) (Figure 5-5). In contrast, by replacing hexane with a denser organic solvent, such as chloroform or perfluorodecalin (F_{18}-decalin), the thiolated JPs self-organized at the water/oil interface with the gold caps facing down to the oil phase ("face-down" configuration, Figure 5-6). Similarly, the self-assembled thiolated JP monolayer was loosely packed at the interface of water/F_{18}-decalin. Note that the dull golden color in Figure 5-6B indicated an opposite orientation (metal caps pointed to the lower oil phase) with respect to the case of water/air interface (Figure 5-3C). The orientation of the JPs can be manipulated at the interface dependent on the density of the selected oil phase.

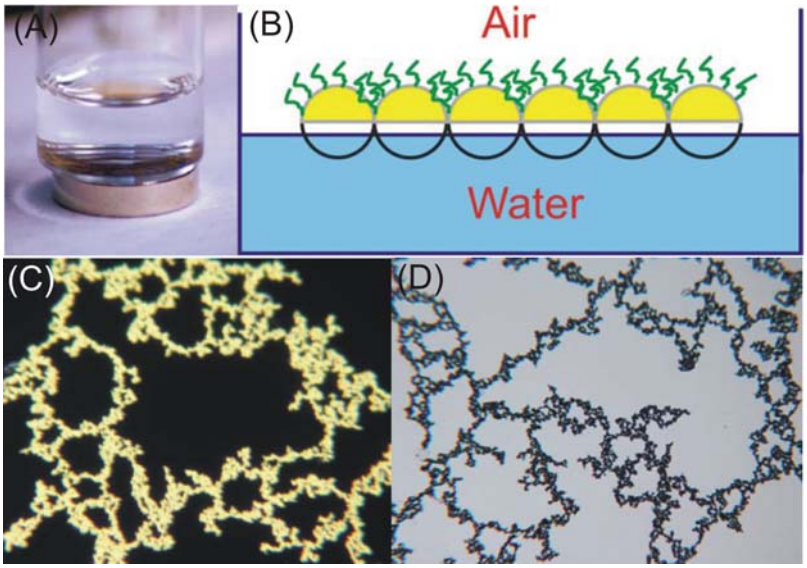

Figure 5-3. Optical imaging (A) and schematic illustration (B) of thiolated Au/Ni-SiO_2 JPs at water/air interface; microstructures of thiolated Au/Ni-SiO_2 JPs assembled at water/air interface, captured by dark-field (C) and transmission (D) optical microscopy.

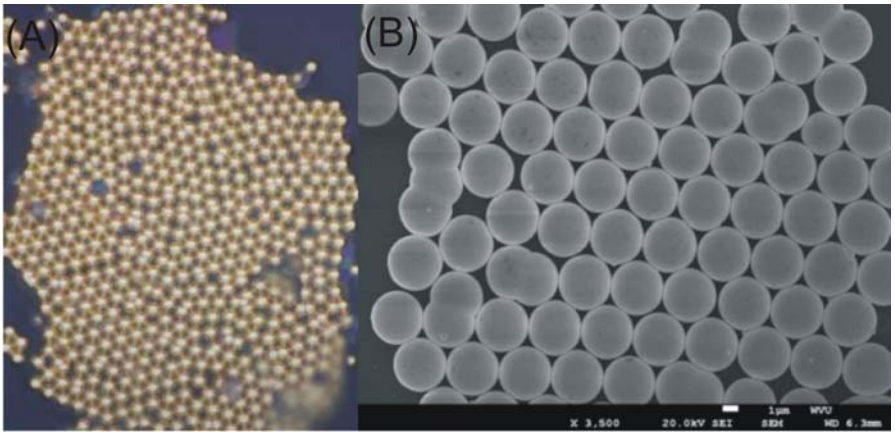

Figure 5-4. Optical micrograph (A) and scanning electron microscopic imaging (B) of the thiolated Au/Ni-SiO_2 JPs after drying on the substrate (scale bar: 1 μm).

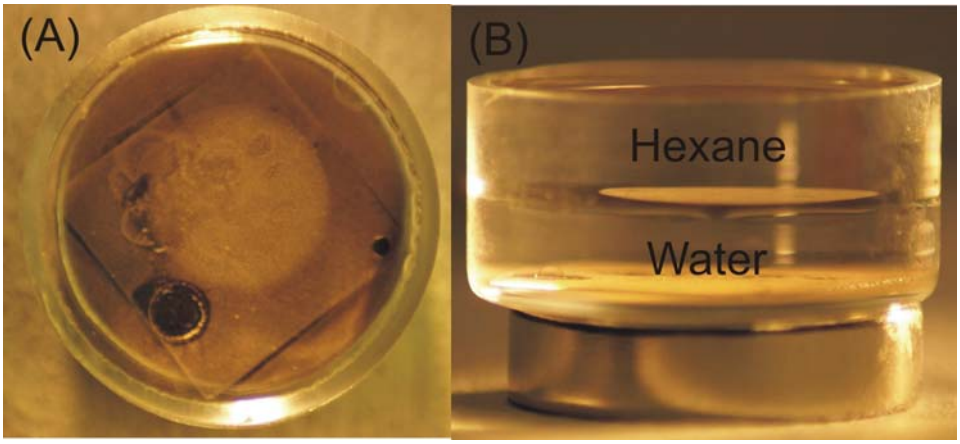

Figure 5-5. Top-view (A) and Side-view (B) of the thiolated Au/Ni-SiO_2 JPs at water/hexane interface. Note that the magnet on the bottom of the vial helped attract the JPs to the central area.

(3) Thiolated Au/Ni-SiO_2 JPs in F_{18}-decalin/glass interface

In a pure perfluorodecalin, the thiolated JPs were easily dispersed using sonication and settled within a short period of time. The JPs started to sedimentate, adsorbing to a pre-immersed glass coverslip and the inner wall of the glass container. The coverslip was lifted away from the oil phase after ~10 minutes and dried in air. As shown in Figure 5-7A, a mixture of orientations of the thiolated JPs was observed. Alternatively, when placed on a flat substrate, the droplet of F18-decalin containing the thiolated JPs started to dry and the JPs formed clusters mostly with the silica hemispheres touching

closely (Figure 5-7B), which indicated attractive interactions between the silica hemispheres of the JPs.

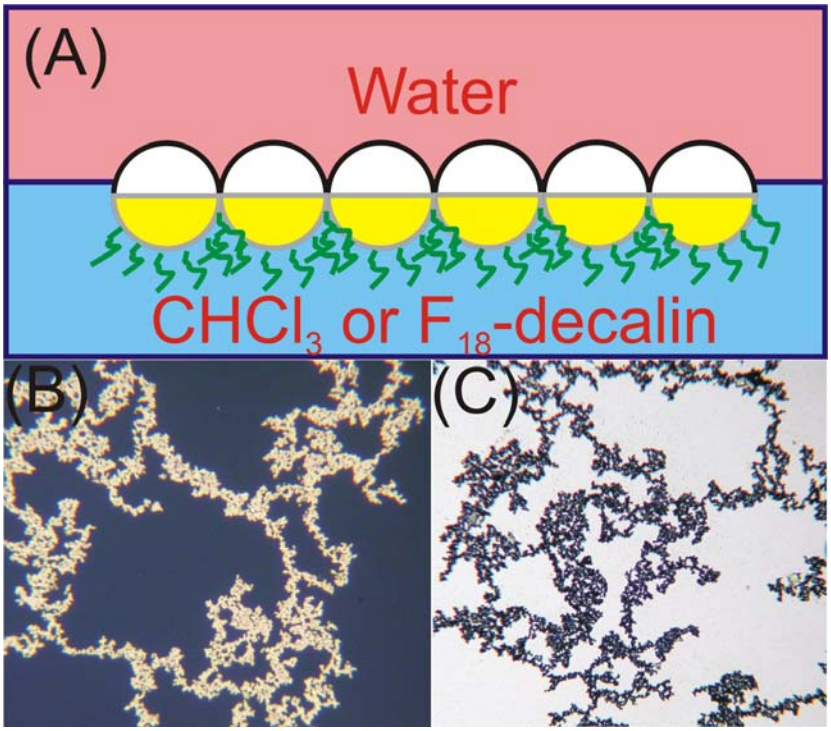

Figure 5-6. (A) Illustration of the thiolated Au/Ni-SiO_2 JPs at water/chloroform (or F_{18}-decalin) interface; dark-field (B) and transmission (C) optical imaging of the thiolated Au/Ni-SiO_2 JPs at water/ F_{18}-decalin interface.

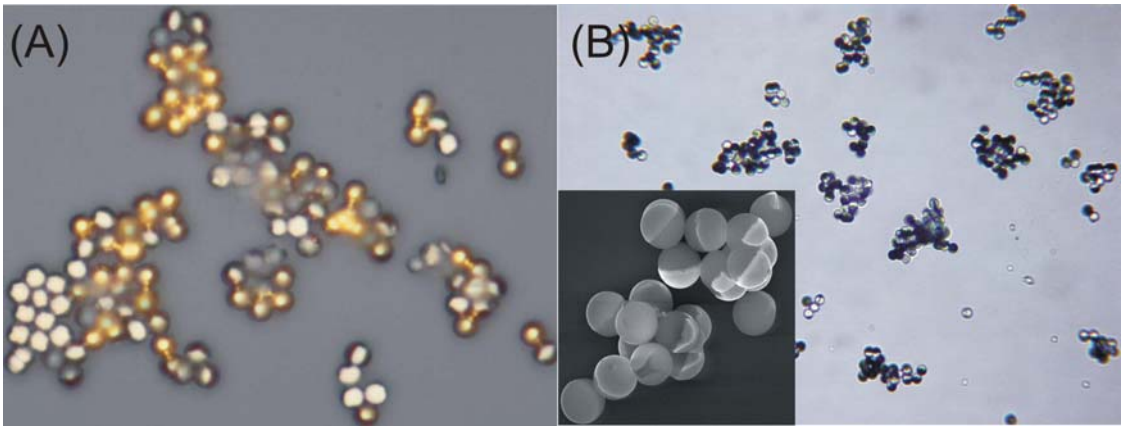

Figure 5-7. (A) Optical images of the thiolated Au/Ni-SiO_2 JPs adsorbed on the pre-immersed coverslip, dried from an F_{18}-decalin solution; (B) clusters formed by the thiolated JPs after dried from F_{18}-decalin (Inset: FE-SEM image of the cluster).

5.3.3 An alternative way to fabricate bimetallic Janus particles

Previously, the use of adhesive substrate was utilized to invert the half metal coated silica particles. The advantage in using the double-sided copper tape was its high adhesion to beads, heat tolerance, and release characteristics.[12] However, several practical problems were discovered. During the inversion procedure, the orientation of the particles was likely to be changed, especially when the normal force was not even through the entire piece of copper tape. The inherent roughness of the substrate complicated efforts to fix the problem – in most cases, the particles did not form perfect single layers on the substrate; loosely packed areas or multilayers were frequently observed due to the particle size distribution. Secondly, the pressing force had to be carefully applied to prevent adhesion of particles from the secondary layers. The inversion procedure limited the yield and quality of bimetallic Janus particles produced.

The self-assembly of the thiolated JP monolayer at liquid/liquid interface provides an opportunity to selectively modify the surface in either phase. The JPs preferential orientation in the same direction at interface allows for direct transfer of beads while the desired face remains in a "face-up" or "face-down" configuration. Flat substrates (i.e. glass coverslips) were utilized to pick up the thiolated JPs, simply by raising the coverslip through the interface of water/air or water/hexane. The silica hemisphere of the JPs adhered to the glass surface with the thiolated metal coating facing to the atmospheric and oil phase. This lift-up process required the initial complete immersion of the glass coverslip into the water phase. This was of no consequence when the water phase was the lower phase, in which the JPs at interface were partially immersed in the water phase. The silica hemispheres appeared to have greater affinity to the coverslip (due to the same composition) than water. When they came into contact, the silica-silica attraction, as well as the gravitation, provided positive contribution to make them stuck together in air and through the oil phase (hexane). Transfer of the "face-down" configuration, however, is not the same case. At interface of water /F_{18}-decalin, the glass coverslip floated on the top of the JP monolayer. The attractive force between the thiol groups and the oil phase (F_{18}-decalin) was strong enough to pull the particles off the coverslip during lift-up. Even when replaced with a hydrophobic (nonpolar) substrate, e.g. alkylsilylated glass surface, the thiolated JPs would rather stay at the liquid/liquid interface.

In the case of water/air interface, the interaction between the thiol groups and the oil phase was minimized. When placed at the interface, thin PDMS film floated on top of the JP monolayer, and the alkane groups appeared to stick well to it. The thiolated JPs were inverted with the "face-down" configuration captured (Figure 5-8). To our best knowledge, this work is the first to demonstrate the inverted duplication of "face-down" configuration using the purely hydrophobic interaction. As a critical intermediate step, this new inversion method would improve the quantity and quality in fabrication of bimetallic Janus particles.[12]

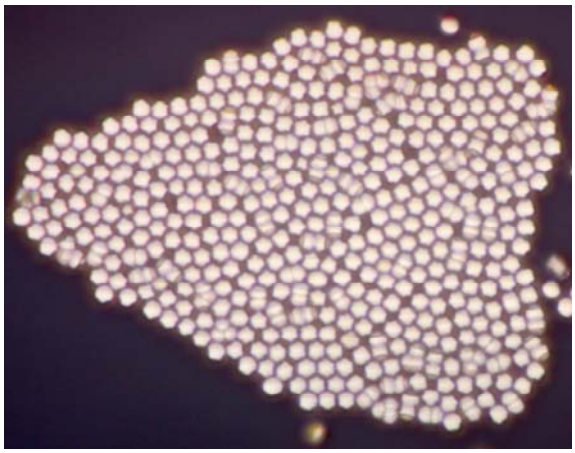

Figure 5-8. A "face-down" configuration of the thiolated Au/Ni-SiO_2 JPs captured on the thin PDMS film.

5.4 Directed Assembly of Magnetic Janus Particles

The design and assembly of building blocks with novel structures and interactions lead to advanced complex superstructures for applications in photonics, electronics and sensing.[1,2] Anisotropic colloidal particles (Janus particles) are considered as unique building blocks due to their multi-functionality and surface anisotropy. Therefore, the assembly of anisotropic colloidal particles requires long-range ordered organization of the particles and the anisotropic elements as well. In the former section, we have successfully demonstrated the confinement of the JPs at the biphasic interface with manipulated orientation. This was realized through incorporation of the internal force (hydrophobic interaction) with selective surface modification. Alternatively, external intervention methods have been sought to direct self-assembly of the JPs, which includes

light,[13] electric and magnetic field,[6-8] producing 2D or 3D desired super structures. In this section, the specific assembly of the magnetic Janus particles is demonstrated in the presence of external uniform magnetic field.

The Au/Ni-SiO_2 JPs are composed of silica microspheres half-coated with nickel and gold. In a pure aqueous solution, the anisotropic feature of the JPs can be easily differentiated from the physical perspective. For instance, the silica hemisphere allows the visible light to penetrate, appearing transparent while the metal coated hemisphere blocks the transmission of the light, appearing dark in optical microscopy. Chemically, however, no specific interaction between the JPs was observed. A direct evidence for that was self-assembly of the Au/Ni-SiO_2 JPs on a flat substrate rendered random distribution with no preferential orientation or obvious interaction between the metal caps (Figure 5-9).

Upon application of a magnetic field parallel to the substrate surface, however, the Au/Ni-SiO_2 JPs assembled quickly, forming staggered chain structures oriented along the direction of the magnetic field (Figure 5-10).[6] These chain structures were featured as single chains with the metal coated hemispheres touching each other and the silica hemispheres alternatively facing outward. Each individual magnetic JP in the chain oriented with its equatorial axis along the direction of magnetic field. Recall that the previous simulation and magnetization measurements in Chapter 4 verified that the magnetic Janus particles had an easy-axis along the equatorial direction. Upon rotation of the applied field in the horizontal dimension, the chains re-oriented to match the direction of the applied field. The chain structures in solution were separated from each other due to the repulsion; occasionally, when the head of one chain came into close to the tail of another chain, a longer chain would be formed. The spacing between the chains was found to be dependent on the concentration of JP solution and the strength of the applied field. A certain degree of relaxation in the direction occurred to the chains after removal of the applied field.

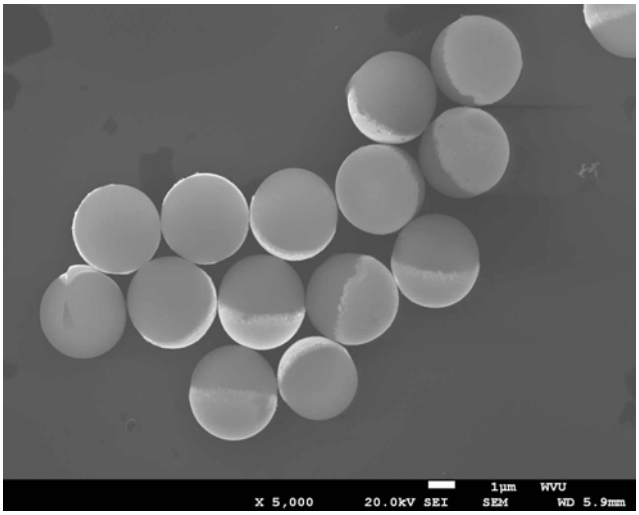

Figure 5-9. FE-SEM image of the Au/Ni-SiO_2 JPs in the absence of magnetic field.

The 2D or 3D well-organized structures on the substrate are desired for optical measurements. However, the staggered chain structures formed in the solution were mostly destroyed during the evaporation of the solvent (water). The capillary force appeared to be greater than the magnetic interaction between the magnetic Janus particles. Application of a stronger magnetic force could not maintain the chain structures. This is most likely due to the magnetization saturation of each individual particle. Other organic solvents such as ethanol, isopropanol and hexane with lower surface tension did not show any improvement in maintaining the structure.

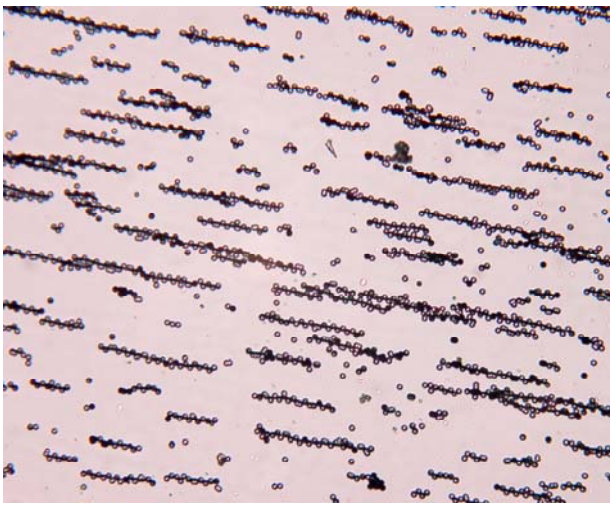

Figure 5-10. Staggered chain structures in solution formed by the Au/Ni-SiO_2 JPs in the presence of external magnetic field.

It is necessary to find a way to lock those patterned structures in place after evaporation. Ammonium carbonate, $(NH_4)_2CO_3$, decomposes into NH_3, CO_2, and H_2O a 58 °C. Suspended into a saturated solution of $(NH_4)_2CO_3$, the magnetic Janus particles behaved similarly as in the pure water, forming staggered chain structures in the presence of magnetic field. High temperature (60 °C, slightly above the decomposition temperature of $(NH_4)_2CO_3$) facilitated fast evaporation of water, and meanwhile, the formation of white crystals was observed to form on the substrate. The white crystals stayed at room temperature but disappeared rapidly at the temperature of 60°C. We believe the added $(NH_4)_2CO_3$ recrystallized during the evaporation of water and then directly decomposed into gaseous molecules.

A pair of permanent magnets was applied in one fixed direction during the process of evaporation and decomposition. After complete removal of the additive, the staggered chain structures remained on the substrate no matter whether the applied field was present or removed, aligning with the chain direction parallel to the previous direction of the applied field (Figure 5-11). The formation of the white crystals adjacent to the JPs appeared to be able to lock the JPs in place during the evaporation of the solvent. The additive could be removed without causing contamination by mild heating.

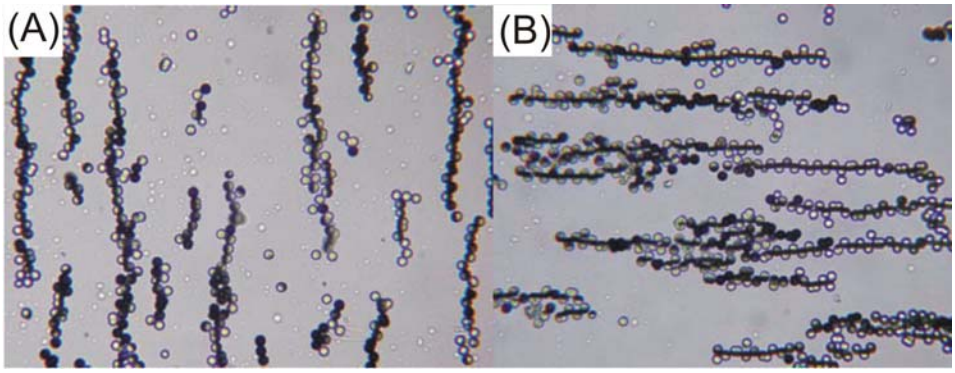

Figure 5-11. Optical images of staggered chain structures dried from a saturated $(NH_4)_2CO_3$ solution after removal of the external magnetic field.

By changing the direction of the applied field from parallel to perpendicular to the substrate surface, the magnetic JPs disassembled from the chains and formed dimeric clusters in most cases, spaced apart from each other (Figure 5-12).[14] The bright smooth surface of the magnet under the substrate acted as a mirror and thus, these images

captured using the refection mode seemed to be transmitted images with clear dark and bright sides. These dimers stood up (one in focus and the other not) with one metal half overlaying on top of the other metal half (Figure 5-13). In fact, these dimers were just one formation of the previous chain structures; instead of containing many JPs, they were composed of two single magnetic JPs. This is due to the field gradient with the strength maximum near the substrate/liquid interface and the magnetic JPs tended to attract to the field maximum. All the dimers are independent magnetic dipoles, oriented in the same direction along the applied field, resulting in repulsion from each other. It is noteworthy that the confinement from the cell dimension (8 μm in height) also played a significant role in determining the cluster structures. This can be investigated through changing the dimension of the spacers.

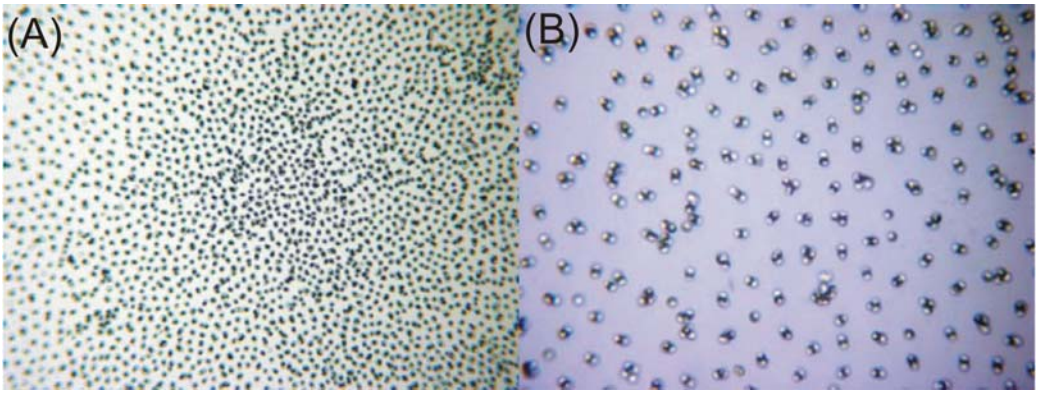

Figure 5-12. Optical images of microstructures (A and magnified B) formed by the Au/Ni-SiO_2 magnetic JPs in the presence of magnetic field perpendicular to the substrate surface. Note that the density gradient (variation in the spacing between the dimers) was due to the field gradient by just using single magnet.

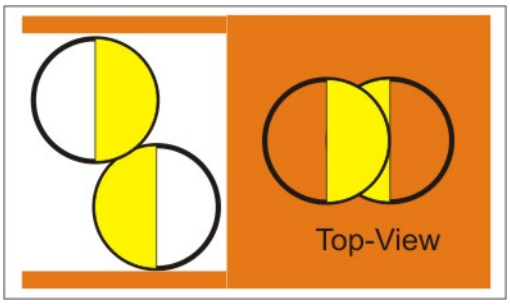

Figure 5-13. Side view and top view of the dimer when the applied field is perpendicular to the substrate surface.

In summary, this chapter demonstrated the behavior of the thiol-surface modified JPs at the interfaces and the transfer of the "face-down" configuration dependent on the hydrophobic interaction. The magnetic JPs formed staggered chain structures when the applied field was parallel to the substrate surface and the configuration of the chain structures were maintained in dry by adding $(NH_4)_2CO_3$ into the water solution. The magnetic JPs also formed dimeric clusters when the applied field was perpendicular to the substrate surface. Future work will focus on the combinatorial effect of the internal and external forces on the assembly of the JPs.

References

(1) Du, J.; O'Reilly, R. K. *Chem. Soc. Rev.* **2011**, *40*, 2402-2416.

(2) Lee, K. J.; Yoon, J.; Lahann, J. *Curr. Opin. Colloid Interface Sci.* **2011**, *16*, 195-202.

(3) Glotzer, S. C. *Science* **2004**, *306*, 419-420.

(4) Glotzer, S. C.; Solomon, M. J.; Kotov, N. A. *AIChE Journal* **2004**, *50*, 2978-2985.

(5) Glotzer, S. C.; Solomon, M. J. *Nat. Mater.* **2007**, *6*, 557-562.

(6) Smoukov, S. K.; Gangwal, S.; Marquez, M.; Velev, O. D. *Soft Matter* **2009**, *5*, 1285-1292.

(7) Gangwal, S.; Pawar, A.; Kretzschmar, I.; Velev, O. D. *Soft Matter* **2010**, *6*, 1413-1418.

(8) Gangwal, S.; Cayre, O. J.; Velev, O. D. *Langmuir* **2008**, *24*, 13312-13320.

(9) Whitesides, G. M.; Laibinis, P. E. *Langmuir* **1990**, *6*, 87-96.

(10) Park, B. J.; Brugarolas, T.; Lee, D. *Soft Matter* **2011**, *7*, 6413-6417.

(11) Ye, S.; Carroll, R. L. *ACS Appl. Mater. Interfaces* **2010**, *2*, 616-620.

(12) Vossmeyer, T.; DeIonno, E.; Heath, J. R. *Angew. Chem. Int. Ed.* **1997**, *36*, 1080-1083.

(13) Skjeltorp, A. T. *Phys. Rev. Lett.* **1983**, *51*, 2306-2309.

Chapter 6

Conclusions and Future Work

This dissertation work studied the fabrication of anisotropic Janus particles and their interesting catalytic and interfacial behaviors, providing fundamental basis for future work in motion and assembly.

Deposition of metals through electron beam evaporation onto both hemispheres of colloidal particles led to the successful fabrication of bimetallic Janus particles (BJPs). The resulting BJPs are capped with various metals on opposite hemispheres, leaving uncoated silica belts around the equatorial region. One of the challenges was to make small sizes of BJPs. The current approach involves the use of adhesive copper tape, by which the BJPs can be made with particle size greater than ~800 nm in diameter. In contrast to the large size particles, the thickness of the adhesive on the copper tape might have a greater influence on the particles with smaller sizes. The small particles might be completely embedded into the adhesive during the inversion procedure, and therefore, the inverted metal half-coated particles were not accessible to the second metal evaporation. A new approach without using adhesive is being sought to fabricate BJPs with small sizes. Chapter 5 presented an alternative method, including the functionalization of metal half-coated Janus particles with long chain alkanethiols, self-assembly of the Janus particles at water/air interface, direct transfer of “face-down” configuration onto a hydrophobic substrate (metal coated hemispheres of the particles facing toward the substrate), and a second metal evaporation. By taking advantage of the amphiphilic Janus character at interface, this approach avoided the use of adhesive, suggesting a promising way to make small size BJPs.

Another challenge was to prepare large quantity of BJPs in order to study self-assembly of these anisotropic building blocks into complex structures. The inversion step in the aforementioned approach appears to be most time-consuming. Future work can be done to develop a highly efficient method based on combination of electroless deposition and roll-to-roll evaporation. The electroless deposition is to make silica-metal core-shell structures and the roll-to-roll process is designed to continuously deposit metal onto the core-shell structures on a flexible substrate.

Chemical transformation of BJPs into JPs with various combinations of metals, metal oxides and metal sulfides through solid-gas heterogeneous reactions was also

demonstrated. Both BJPs and transformed BJPs are a group of anisotropic building blocks. The surface materials range from metals to metal oxides, metal sulfides, and other possible species, and therefore, the properties of the resulting Janus particles differ in optical, magnetic, electronic and catalytic behavior. More importantly, the vast library of anisotropic particles provides a variety of potential means to manipulate the JPs. For instance, electric, optical or magnetic fields would play a significant role in control of the orientation of the JPs through polarization or magnetic interaction with the anisotropic structures leading to formation of extended arrays. The use of more than one component to manipulate BJPs or transformed BJPs in a design-specific manner could lead to use in applications such as targeted cargo transportation and the fabrication of photonic crystals.

Self-propelled Janus particles in H_2O_2 solutions are envisioned as one of the smallest artificial engine systems which convert the chemical energy into mechanical movement. This system also offers an opportunity to compare the features of non-biological chemical propulsion to those of self-propelled particles in living systems. The self-propulsion arises from catalytic decomposition of hydrogen peroxide on the asymmetric surface of Janus particles. However, the detailed mechanism remains unclear although several major mechanisms have been proposed for this system. Future experiments can be done to explore the factors that influence the motion of self-propelled Janus particles, such as imposed temperature, pH, ionic strength, or concentration gradient. These experiments will provide direct or indirect evidence for mechanistic study.

The direction control of the particle in solution may be realized through the use of light source, electric field, concentration gradient and so on. Magnetic control over the direction of particle motion using the external magnetic field is an example to take advantage of self-propulsion in this system. The magnetic JPs can be steered with a high degree of precision to undergo motion in an arbitrary pathway. This remotely controllable engine system is promising as a cargo transporter in the micro-channel networks. However, a complete control over the self-propelled motion has to overcome the Brownian effect, which is ubiquitous to all the colloidal motion systems. This becomes more difficult as particle vehicle size decreases. In addition, this research employed a pair of permanent magnets to control the orientation of the Janus particles. An automated

rotational magnetic field is preferred to better modulate the particle motion. Future work will be focused on design of a rotational electromagnetic field setup, which can be fitted onto the microscope, in order to control of the particle orientation in high precision.

The interfacial behavior of the alkanethiol functionalized JPs offers an obvious practical application as particulate surfactants. The preliminary study in Chapter 5 described the self-assembly of the Janus particles at interfaces in a qualitative way. Quantitative experiments will be conducted with Janus particles at interfaces (flat surface) and in emulsion (curved surface). The formation of staggered chain structures comprised of magnetic Janus particles has been demonstrated in the presence of external magnetic field. And the configuration of the chain structures can be maintained using $(NH_4)_2CO_3$. Future work will be focused on the control of the spacing between the chain structures by adjusting the field strength, particle concentration, particle size and metal thickness. The aim of this research is to prepare ordered chain structures for optical study.

3D nanostructures with controllable structure can be formed into high fidelity patterns by geometrically structured dynamic shadowing lithography. Based on the predictive empirical model, the height and shape of the 3D metal dot arrays can be carefully controlled through deposition rate from the e-beam evaporation system. We believe that huge benefits can be garnered by knowledge of the detailed geometry of the deposited material with respect to the studied parameters. For instance, as the size and shape of the metal nanostructures changes, the localized surface plasmon resonance would change accordingly. This would allow further information on the physical and chemical properties of the SL substrates to be elucidated. These structures also present an interesting substrate to perform magnetic studies of certain material whose magnetic domain is comparable to the size of the nanostructures.

Appendix:
γ, θ_{axis}, θ_{motion} Analysis

Particle motion was recorded on an inverted optical microscope with a 100X oil objective. According to the captured images, the particles at the submicron scale can be clearly observed. In addition, dark spots and intensity variation in the field of view are also observed and captured. The noisy background sometimes causes interference, which makes hard to track the particles using Video Spot Tracker. This software tracks the particles based on the intensity difference between the particle and background. When the particles move close to an area which has a similar intensity to the particle itself, the software will not be able to differentiate in an accurate way, which most likely provides false information. This requires a removal of the background noise from each frame.

The background frames were captured in the same field of view as the original sample frames when there were no motile particles. The intensity of the background frames were averaged using the image processing software ImageJ. The resulting averaged background frame was subtracted from all the sample frames. After removal of the background noise, these frames typically possess a flat a background, which facilitates the tracking.

The segmentation is also carried out in ImageJ. Because the intensity of the silica side (bright area in the particle) is higher than that of the background, and the intensity of the platinum side (dark area) is lower than that of the background, both the silica hemispheres and the platinum hemispheres can be segmented using "Threshold" in ImageJ. The x-y positions of the silica and platinum hemispheres can be extracted in Video Spot Tracker, and then used to determine the average speed, mean squared displacement, γ, θ_{axis}, and θ_{motion}.

Sample file: 080528.16.31.07

Sample frames: #355-374

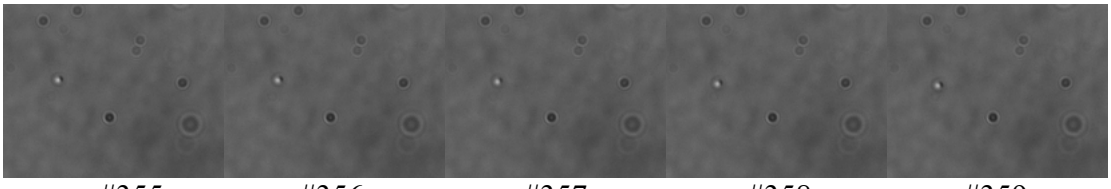

#355 #356 #357 #358 #359

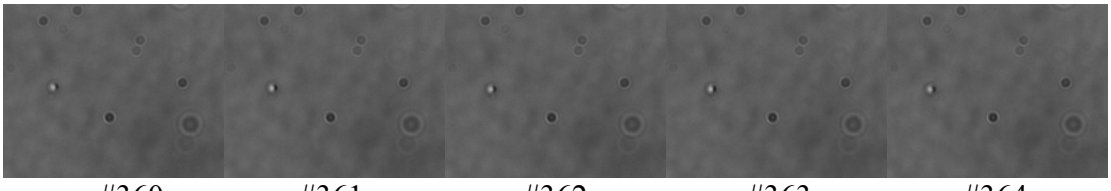

#360 #361 #362 #363 #364

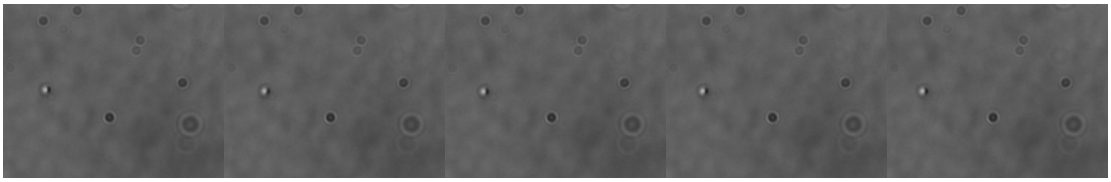

#365 #366 #367 #368 #369

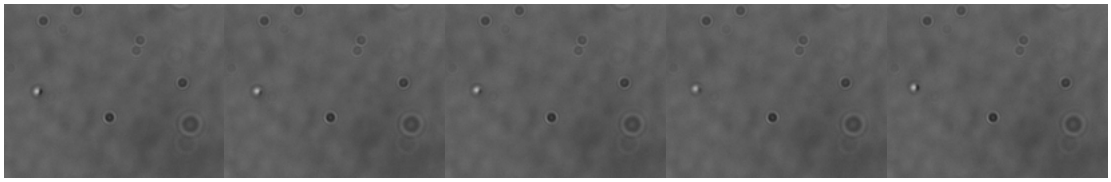

#370 #371 #372 #373 #374

Background frames: #3000-3136

The frames between #300-3136 are almost the same. A typical frame (#3000) with no particle in the field of view (the particle moved out of the field of view) is shown below:

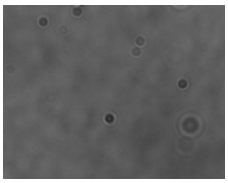

1. Image processing in ImageJ:

1) Select the regions having particles in all 20 sample frames, crop selection (x=7, y=34, z=0, w=63, h=54) for both sample frames and background frames.

Sample frames:

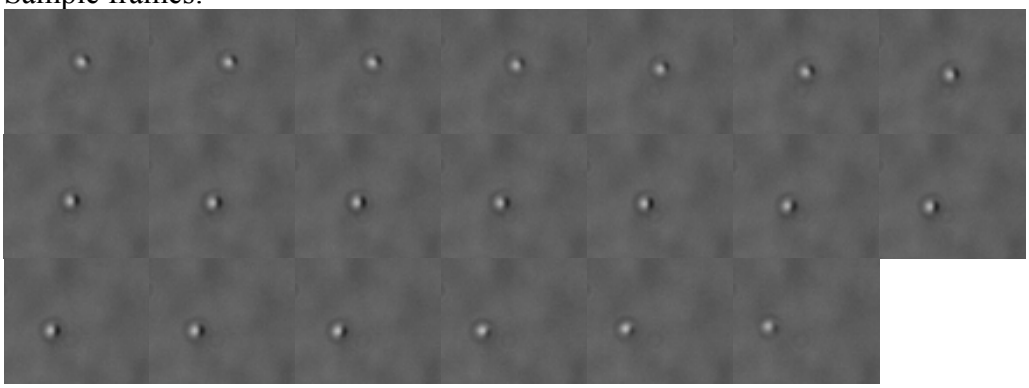

Background frames:

2) Average intensity of a stack of backgrounds (#3000-3136).

Image>Stacks>Z Project…>Projection Type: Average Intensity

Averaged background frame:

3) Background removal from the sample frames.
Process>Image Calculator>Image 1 (sample frames) – Image 2 (Averages background frame)
Background subtracted sample frames:

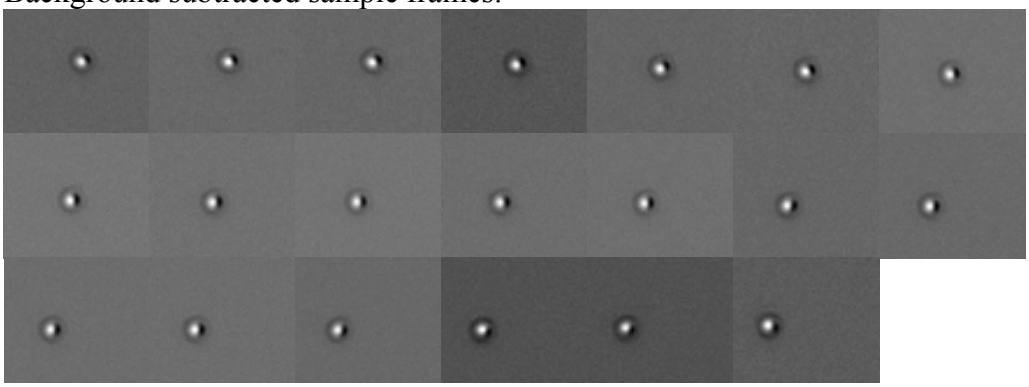

4) Segmentation of Pt and SiO_2 hemispheres.
Image>Adjust>Threshold…

Pt hemispheres:

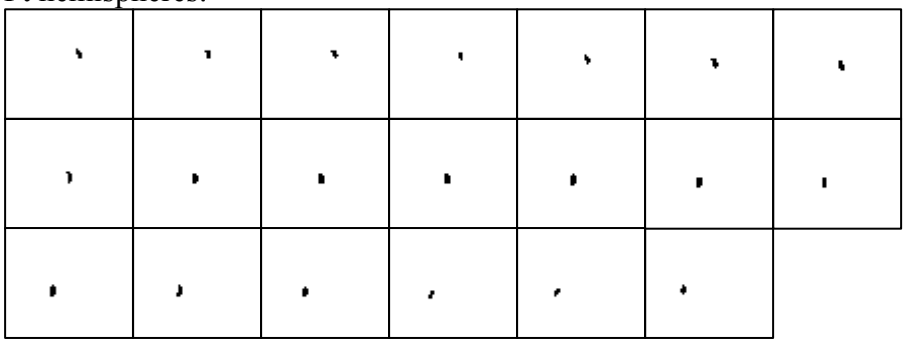

SiO_2 hemispheres:

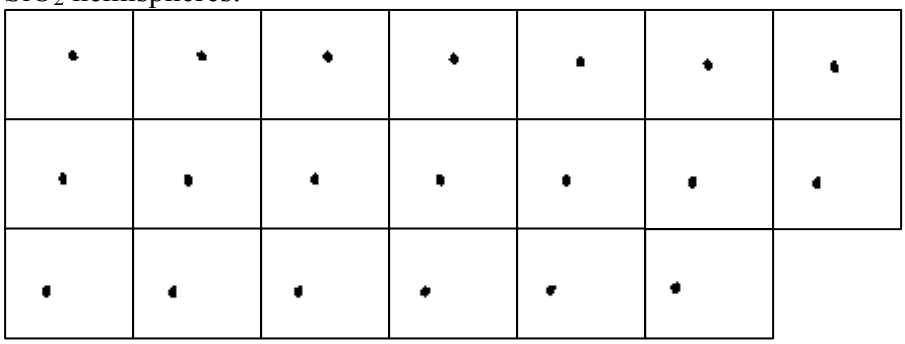

2. Position (x,y) tracking in Video Spot Tracker
Pt hemispheres:

Entry	Frame Number	X (pixel)	Y (pixel)
1	355	36.15625	21.3125
2	356	36.46875	21.53125
3	357	35.53125	21.53125
4	358	34.53125	22.375
5	359	34.03125	24.09375
6	360	33.65625	25.75
7	361	33.125	27.28125
8	362	31.34375	28.34375
9	363	29.75	29.15625
10	364	28.75	29.25
11	365	27.75	29.25
12	366	27.125	29.59375
13	367	25.9375	30.625
14	368	24.53125	30.65625
15	369	23.125	30.59375
16	370	22.375	30.8125
17	371	20.75	31.25
18	372	20	32.375
19	373	18.8125	31.1875
20	374	18.15625	30.25

SiO_2 hemispheres:

Entry	Frame Number	X (pixel)	Y (pixel)
1	355	32.625	22.15625
2	356	33.1875	22.40625
3	357	32.1875	22.6875
4	358	31.25	23.71875
5	359	30.46875	25.25
6	360	30.25	26.6875
7	361	29.4375	27.71875
8	362	27.625	28.625
9	363	26.40625	29.34375
10	364	25.53125	28.84375
11	365	24.4375	29.25
12	366	23.46875	29.53125
13	367	22.5	30.375
14	368	20.53125	30.84375
15	369	19.5	30.375
16	370	18.53125	30.84375
17	371	17.5	30.5625
18	372	17.0625	30.53125
19	373	15.75	29.75
20	374	14.21875	28.71875

3. The γ, θ_{axis}, θ_{motion} angles can be calculated by using the x-y values.